1-1-2015

Mesoscale Full Field Modeling of Stress Localization in Polycrystalline Materials Deforming by Both Slip and Twin

Vahid Tari

Mesoscale full field modeling of stress localization in polycrystalline materials deforming by both slip and twin.

By

Vahid Tari

A Dissertation
Submitted to the Faculty of
Mississippi State University
in Partial Fulfillment of the Requirements
for the Degree of Doctor of Philosophy
in Computational Engineering
in the Department of Computational Engineering

Mississippi State, Mississippi

August 2015

Mesoscale full field modeling of stress localization in polycrystalline materials deforming by both slip and twin.

By

Vahid Tari

Approved:

_____

Haitham El Kadiri
(Major Professor)

_____

Anthony D. Rollett
(Committee Member)

_____

Andrew L. Oppedal
(Committee Member)

_____

Edward A. Luke
(Committee Member)

_____

Shantia Yarahmadian
(Committee Member)

_____

Pasquale Cinnella
(Graduate Coordinator)

_____

Jason M. Keith
Interim Dean
Bagley College of Engineering

Name: Vahid Tari

Date of Degree: August 14, 2015

Institution: Mississippi State University

Major Field: Computational Engineering

Major Professor: Haitham El Kadiri

Title of Study: Mesoscale full field modeling of stress localization in polycrystalline materials deforming by both slip and twin.

Pages in Study: 134

Candidate for Degree of Doctor of Philosophy

The aim of this PhD thesis is to incorporate deformation twinning in a full-field viscoplastic crystal plasticity model based on fast Fourier transform in an effort to gain insights into its role on strain localization. This work is motivated by current experimental evidences on the important role that dislocation reactions at the twin interface play on damage initiation in materials during plastic deformation.

We began first by investigating the role of slip on stress localization. To this end, we simulated the effect of macroscopic deformation path, which dictates a macroscopic stress state, as well as pre-existing microstructure in typical ferritic steel, where plastic deformation is accommodated by slip mechanism. The results show that the width of localized strain rate regions near grain boundaries is a function of the deformation path, and there is a positive correlation between local Taylor factor and local stress field, which slightly depends on deformation path.

For the incorporation of mechanical twinning in twinning-induced plasticity (TWIP) steel, we implemented predominant reorientation scheme (PTR) in vpFFT, which was implemented previously in the mean field VPSC. The comparison between

experimental and simulation results indicates that twin volume fraction, final texture, and stress-strain curve were satisfactorily predicted. Despite that predominant twin reorientation scheme was not suitable to capture lamellar shape of twins in the microstructure, twin domains were predicted to form and grow at or close to grain boundary regions.

Finally, we surveyed current literature, which aimed at capturing the characteristic lamellar morphology of twins. Literature review shows several unsuccessful crystal plasticity simulations in capturing twin nucleation and twin lamellar shape at measocale. These inabilities can be attributed to i) twin nucleation that is controlled by local atomistic configurations and stress fluctuations at the grain boundaries, and ii) the random or stochastic nature of twin nucleation, which has been proved by EBSD observation. Based on the EBSD observations, twin nucleation depends on both microstructural (e.g, grain size, dislocation density) and loading conditions (e.g, stress, strain). Furthermore, the propensity, frequency, and morphology of deformation twins are different among grain with the same orientation and applied boundary conditions.

DEDICATION

To my mom and dad who are the symbol of unconditional love.

ACKNOWLEDGEMENTS

I would like to acknowledge my supervisor Dr. Haitham El Kadiri who gave me the opportunity to study in this field, and encouraged me in this journey.

My special thanks goes foremost to Prof. Anthony D. Rollett for introducing me with the field of texture and anisotropy, his patience and kindness with me has made this field for me so enjoyable. His eagerness in education of students and his willingness to give his time, even when he has a little time, to students who want to learn have been inspiring. I am indebted to Prof. Rollett for his guidance when I was in his group in building my professionalism in the intellectual way.

I would like to thank Dr. Hossein Beladi for providing three-dimensional microstructure and experimental data. I have benefited from scientific discussion with him during this research, and I really appreciate his kindness and patience.

I would also like to acknowledge Dr. Andrew L. Oppedal for his great patience and his guidance during my research.

I am also thankful to Dr. Edward A. Luke and Dr. Shantiya Yarahmadian for serving as my committee members.

TABLE OF CONTENTS

LIST OF TABLES

LIST OF FIGURES

CHAPTER I

INTRODUCTION

1.1 Introduction

The reduction of greenhouse gases (GHG) and reduced dependence on hydrocarbon-based fuels is a key priority worldwide. The United States, Canada, China and the Euro-zone have engaged, in a first stage plan to reduce the mass of CO_2 emitted by passenger vehicles a full 30-50% below current standards by the year 2020 (targets: 95g/km for EU and China; 110g/km for the USA and Canada). Such tremendous improvements will require extensive vehicle mass reduction through the use of lightweight materials allowing for (1) a net fuel economy improvement in combustion engine and (2) an increase in the range of electric vehicles. In addition, all material developments must maintain or improve crash worthiness of current vehicles.

Metals that have potential to satisfy these conflicting demands contain a hexagonal close-packed (HCP) crystal structure, twinning-induced or martensitic transformation-induced plasticity steel, and/or aluminum alloys. Candidate materials systems are based upon magnesium (Mg), titanium (Ti), as well as advanced-high strength steels (AHSS), including twinning-induced plasticity (TWIP), third-generation advanced high strength (3GAHSS), and transformation-induced plasticity (TRIP) steels. However, current structural applications of HCP Mg alloys, in particular, are limited to castings due to difficulties associated with forming wrought alloys. In order to increase

applications of these lightweight materials in response to the critical needs within the transportation sector, improvement in both their formability and ability to absorb energy during a crash is required.

The plastic anisotropy of the hexagonal lattice is widely understood as the source the present limitations associated with HCP metals [1]. The dislocations which easily accommodate plasticity in HCP crystals generally have Burgers vectors within the basal plane. Thus, these materials suffer from an inability to easily deform along the HCP crystal c-axes, in the absence of a deformation twinning-based mechanism of strain accommodation. Deformation twinning has long been known to alleviate the requirement to satisfy the von Mises criterion for polycrystalline plasticity that demands five independent easy dislocation slip modes [2]. However, deformation twinning-based plasticity can be a "double-edged sword." Several examples [3–5] in the literature demonstrate where twinning is associated with fracture initiation, and there are a number of micro-mechanism hypotheses to explain these phenomena.

1.2 Effect of twinning on Mechanical (anisotropic) behavior

In HCP crystals, the most common twinning mechanism involves shear on the $\{10\bar{1}2\}$ planes and is known as tension twinning [6] in Mg alloys; shear produces tension parallel to the c-axes of the crystals. It is responsible for the asymmetry characteristic of strongly textured alloys since the activity of this mechanism is minimized or maximized by just inverting the sign of the stress or by changing the strain path (Figure 1.1). However the interactions involving slip, twinning, and microstructural feature which are responsible for the rapid strain hardening shown in region II of Figure 1.1 are much less understood. Similarly, the interactions which lead to rapid strain incompatibilities and

localization between grains and damage initiation are only qualitatively understood [7–10].

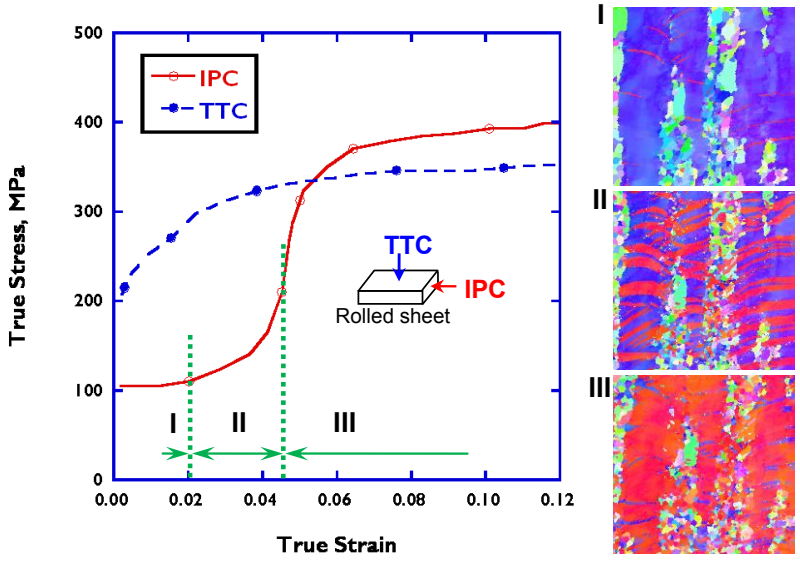

Figure 1.1 Plastic anisotropy of magnesium

(Left) Stress-plastic strain curves typical of rolled sheets when deformed by in-plane compression (IPC) and through thickness compression (TTC) [11]. This anisotropy is caused by minimal twinning during TTC and profuse $\{10\bar{1}2\}$ twinning upon IPC. The IPC curve presents a Regime II characterized by pronounced increase in strain hardening rate. (Right) Orientation image maps produced by sequential EBSD show deformation twins (red) growing in the parent (blue) when an extruded Mg alloy, AM30, was compressed [12].

Interactions involving slip and twinning within a given grain clearly underlie the rapid strain hardening shown in region II of Figure 1.1. However, nearly a century of focus on the strain hardening of materials accommodating plasticity by dislocation slip alone has diverted scientists from determining the relationships which govern the strain hardening during twin accommodated plasticity. For example, recall the well-accepted Taylor hardening expression, $\tau = \tau_0 + \alpha\mu b\sqrt{\rho}$, where τ is the critical resolved shear stress and ρ is the dislocation density, α is a geometrical parameter, μ and b are shear

modulus and burger vector, respectively. Similarly, the plastic strain incompatibilities between neighboring grains clearly underlie the rapid fracture initiation. However, the ductile fracture of metals and alloys with face centered cubic (FCC) and body centered cubic (BCC) crystal structures are largely dictated by second-phase particle fracture and/or interface debonding. Depending on the initial microstructure, as mentioned above other interactions appear to additionally drive damage initiation in HCP alloys, e.g. Mg.

1.2.1 Twin nucleation at grain boundaries

Single crystal tests aimed at addressing whether or not twinning is a type of pseudo-slip deformation mechanism generally show substantial scatter in the critical resolved shear stress (CRSS) [6,13,14]. In general, the twinning stress exhibits an as of yet poorly understood dependence on microstructure, strain rate, temperature, stress state, prior slip, and crystallographic texture. Fundamental studies on the generation of highly glissile twinning dislocations and their crystallography have since then been undertaken in an effort to develop physics-based models suitable for higher length scale simulations such as crystal plasticity [15,16]. A significant number of researches [14,15,16] have shown the scatter in CRSS to the state of pre-existing defects in test sample. This suggests that the casting, or other preparation methods, affect the twinning stress. Hence, the Schmid law should still be in principal applicable to twinning [20–22], but with a marked sensitivity to initial material impurity. This has led to the suggestion that twin embryos always pre-exist in the investigated samples [23]. Alternatively, other authors have suggested that a twin originates either from spontaneous nucleation in the elastic field due to a stress concentration agent, such as an internal defect, [18,19,24,25], or from dissociations of prior slip dislocations [26–30] also be favored by stress concentrators.

The above three mechanisms (pre-existing defect, "growth accidents", and spontaneous nucleation due to stress concentration) for twinning nucleation are still the subject of intense debate in the research community.

Following the premises of micro-plasticity suggested by Meyers et al. [11] and Armstrong et al. [32] developed a dislocation pile-up based constitutive model to account for the negative grain-size effect [4,33,34]. The main idea relies on the primary role of dislocation pile-up on twin nucleation. The grain size has to be large enough to permit sufficiently long pile-ups capable of increasing the internal stress to the level required for a twin nucleation event, otherwise the twin will simply not form. These approaches were later refined and used to explain the strong dependence of twinning on grain size [35] and even an apparent disappearance of twinning when the grain size drops below a critical value usually in the one micron range [33,36]. The work by Barnett et al. [37] emphasized the size effects inherent to twinning, which are mainly reflected by the square dependence of the number fraction of twins to the grain size. The apparent vanishing of twins in very small grains created controversy since twinning was observed in nanocrystalline aluminum and copper at even slow strain rates and low temperatures [38,39]. These controversies have stimulated theories supporting a double-inverse grain size dependence [38,40]

Recent endeavors have highlighted that $\{10\bar{1}2\}$ twins in HCP metals may preferentially nucleate from low-angle grain boundaries (GBs) [41–43] (Figure 1.2), or from artificially introduced $\{10\bar{1}2\}$ stacking faults in molecular dynamics (MD) simulation schemes. Nucleation from a defect-free environment inside a single crystal, though possible, requires excessively high stresses [44].

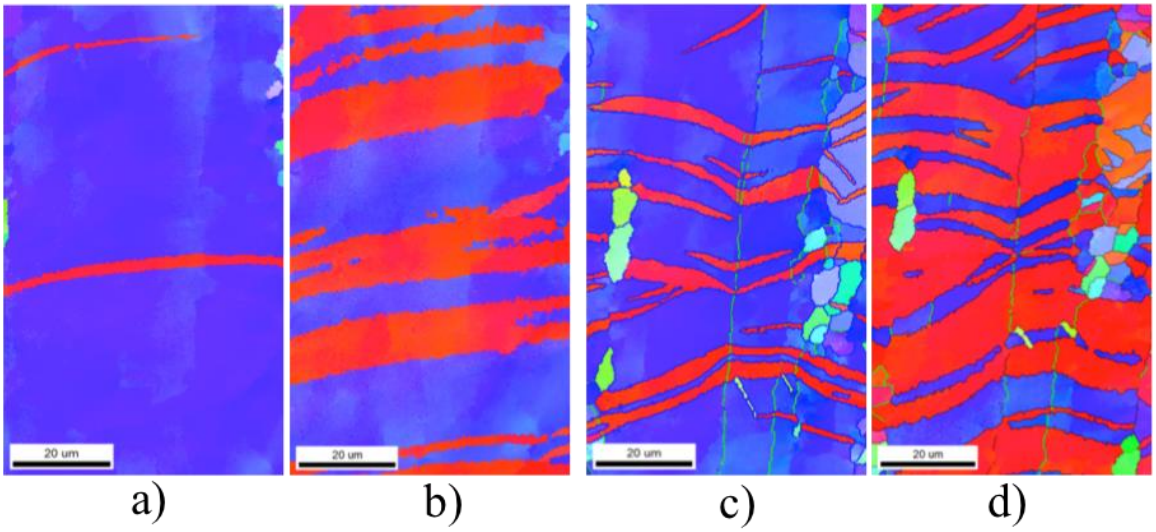

Figure 1.2 EBSD investigation of twin nucleation at grain boundaries

Inverse pole figure maps obtained by in sequential EBSD showing {10-12} twins (red regions) in AM30 magnesium deformed at two same compressive plastic strain levels (2.3% and 4.7%) but within two regions [12]. In (a-b), a region of a grain having only highly misoriented grain boundaries (>15), and in (c-d) a region of a grain containing a central boundary with a misorientation angle less than 15°. The grain boundaries outlined in green correspond to misorientation angles less than 15° while those outlined in black correspond to misorientation angles greater than 15°. Growth in the first region is dominated by edgewise propagation of a few nuclei, while in the second region, growth is dominated by greater nucleation rate due to the low misoriented tilt boundary.

Using density-functional theory, Wang et al. [45] showed that a $\{10\bar{1}2\}$ stable nucleus triggered by a $\{10\bar{1}2\}$ stacking fault requires at least six twinning disconnections (TDs) to strike simultaneously. Conversely, these authors suggested a pragmatic process whereby a twin embryo can nucleate at a symmetric tilt wall provided a pile-up of lattice dislocations is applied to the boundary [46].

This process was not described as dissociation of lattice dislocations into twinning dislocations. Rather, the lattice dislocations acted as stress concentrators, motivating nucleation through a “pure shuffle” mechanism. In contrast, Barrett et al. [47] have demonstrated that a twin facet can readily nucleate at a high-angle $\{10\bar{1}0\}$ ||(0001) basal-

prismatic (BP) boundary through a mechanism which only implicated intrinsic interfacial dislocations and actually transformed one of the pre-existing grains into a twin. The twin boundary (TB) was shown to nucleate from a pile-up of $b_{2/2}$ type disconnections as a relaxation process of the attendant distortion field.

This literature review suggests that twin nucleation is driven by complex interactions between lattice dislocations and interfacial intrinsic defect of GBs.

1.2.2 Twin propagation

There are two stages of twin propagation that stem from different mechanisms, i) the drastic lengthwise thickening parallel to the composition plane, and ii) the progressive edgewise thickening normal to the habit plane, known as normal growth or twin propagation [23], which depends on various mechanisms such as twin-twin interactions (Figures 1.5 & 1.6).

The lengthwise thickening has strong ties with nucleation and was believed for a long time to involve complex mechanisms related to formation of emissary dislocations and to elasto-plastic compatibility at the tip of the tapering twin [48,49]. Recently, these concepts have been proven invalid following the researches [45,48,49,50, 51], which demonstrated the primary role of the basal-prismatic asymmetric tilt boundary (Figures 1.3 and 1.4). These complexities transcend the scope of this literature review. However, the development of the characteristic lamellar morphology of twins resides in the mechanisms taking place at this early stage of propagation. Therefore, for a full field model (the full field term means both long-range and short-range grain interactions are considered) to capture the microstructure induced by deformation twinning, a micromechanical framework for the lengthwise thickening needs to be implemented.

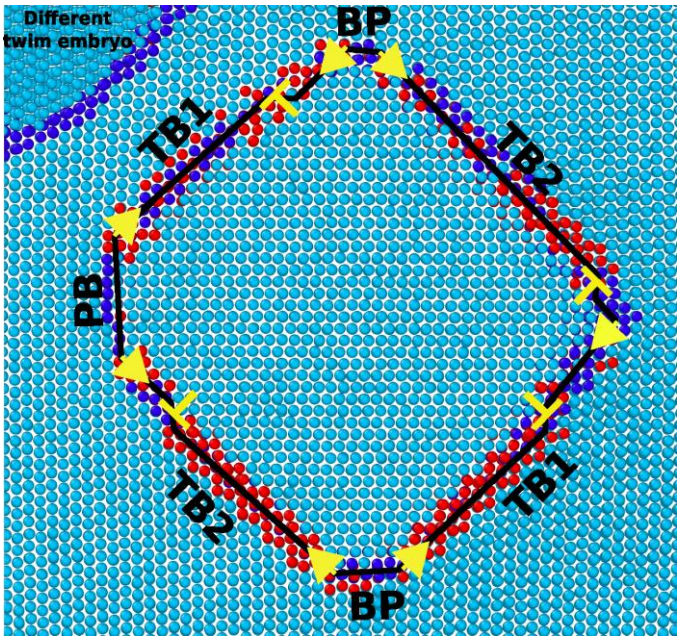

Figure 1.3 Atomic scale simulation of lengthwise thickening

Molecular dynamics simulations by Barrett et al. [50] illustrating the role of basal prismatic (BP) boundary, various variants of $\{10\bar{1}2\}$ twinning, twinning disconnections in the drastic lengthwise thickening of a $\{10\bar{1}2\}$ twins in Mg.

Twin propagation is a widely discussed topic in the literature, but the fundamentals were primarily provided between the nineteen fifties and the nineteen seventies. Starting from the nineteen eighties, most efforts concentrated on numerical investigations of the previous theories through atomistic simulations [54,55,15].

A crucial topic concerned the origin and dynamics of twinning disconnections that accommodate normal growth. Theoretical efforts led to two distinct schools of thought. The first school assumed spontaneous nucleation of twinning disconnections, whereupon stress and thermal agitation act in tandem to create little islands of twin on each successive lattice composition plane. Confounding the elastic properties of the matrix and the interface, the theory implied that a nucleation would be improbable if the Burgers vector magnitude of the twin disconnection exceeds approximately one half of

the interatomic spacing in the composition plane. This ramification was consistent with twin propagation in double-lattice structures such as face-centered tetragonal, orthorhombic and $\{10\bar{1}2\}$ twinning in HCP, but inconsistent with twin propagation in cubic metals.

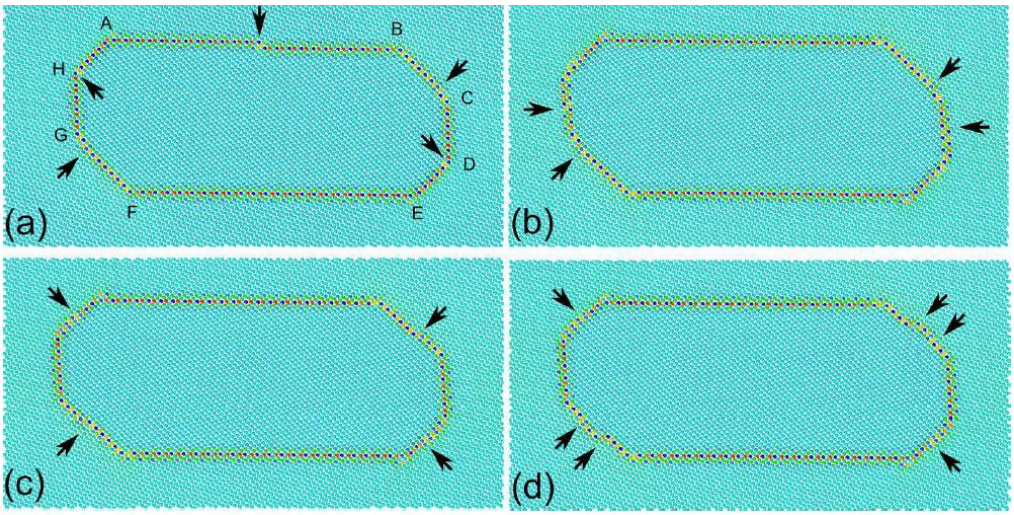

Figure 1.4 Atomic scale simulation illustrating the role of basal prismatic boundaries

(a) Molecular dynamics simulations by Ostapovets et al. [52] illustrating the role of basal prismatic (BP) boundary and disconnections in the drastic lengthwise thickening of a $\{10\bar{1}2\}$ twins in Mg. (a) Initial relaxed configuration with one disconnection in the $\{10\bar{1}2\}$ upper boundary and one disconnection in two BP boundaries. (b, c and d) Different stages of twin growth under applied shear strain. Arrows point to disconnections.

Based on the wider core of twinning disconnections compared to bulk dislocations [56,57], Yamaguchi and Vitek [57] provided calculations that corroborated the normal growth by spontaneous nucleation, and actually supported the fact that the twinning stress for growth is a fraction of that for nucleation. In sum, there is so far no theory put forward that would negate the theory of spontaneous nucleation for twin propagation.

However, the most widely accepted theory for twin propagation is the pole mechanism for normal growth put forward independently by Cottrell et al. [58] and Thompson et al. [59], which constitute the second school of thoughts. This theory rests on the creation of generating nodes and twinning disconnections by matrix slip dislocations when they intersect the twin boundary. This theory has been recently confirmed by MD simulations by Barrett et al. [47]. The dislocation segment within the matrix, resp. within the twin, and connected to the node, forces the gliding twinning disconnections to proceed forward toward the matrix, resp. or backward toward the twin, accommodating normal twinning propagation, resp. normal detwinning shrinkage depending on the stress sign. The theory showed a remarkable consistency with the fact that twinning stress for growth is a fraction of that for nucleation [58].

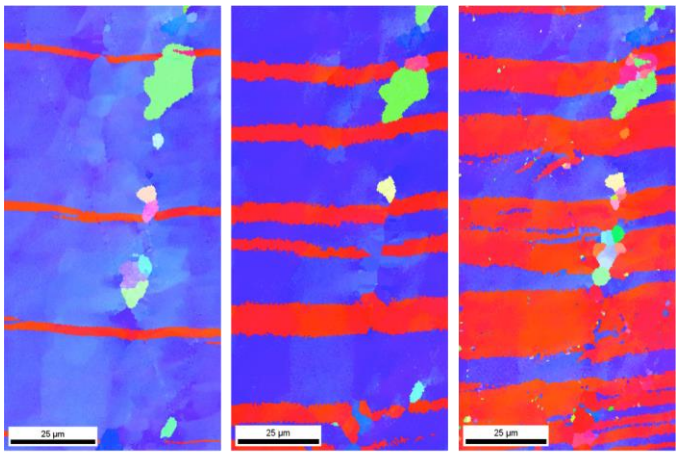

(a) 2.3% (b) 3.8% (c) 6.0 %

Figure 1.5 In situ EBSD investigation of mechanical twinning

Inverse pole figure maps obtained by sequential EBSD on a grain deformed at three compressive plastic strain levels: (a) 2.3%, (b) 3.8%, (c) 6.0%, which experienced a single variant of $\{10\bar{1}2\}$ twinning growing under 0.315 initial value of the Schmid factor [43]. The twins, in red, grew in the parent matrix, in blue, having mainly the ED$\|\langle 10\bar{1}0\rangle$ orientation.

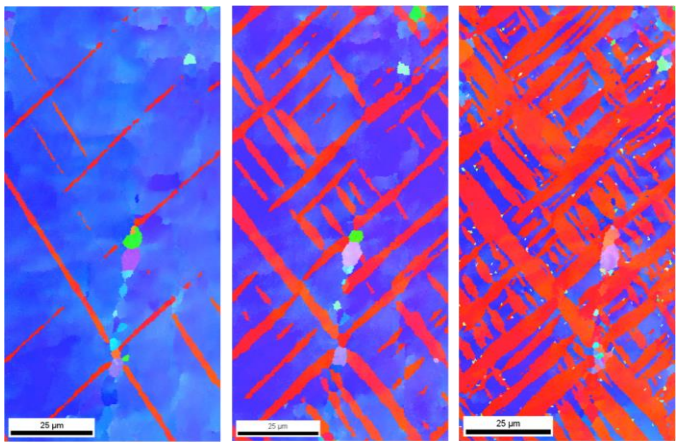

(a) 2.3% (b) 3.8% (c) 6.0 %

Figure 1.6 In situ EBSD investigation of lengthwise and edgewise thickening

Inverse pole figure maps obtained by sequential EBSD on a grain deformed at three compressive plastic strain levels: (a) 2.3%, (b) 3.8%, (c) 6.4%, which experienced two variants of $\{10\bar{1}2\}$ twinning growing both under 0.49 initial value of the Schmid factor [43]. The twins, in red, grew in the parent matrix, in blue, having mainly the ED$\|\langle 10\bar{1}0\rangle$ orientation.

Here again, our literature review on twin propagation suggests that this phenomenon results from complex interactions between lattice dislocations and twin boundaries leading to the creations of MB disconnections that thread the twin boundary and accommodate its advance in the parent grain.

1.2.3 Twin- GB interactions

When a deformation twin is nucleated at a GB, propagates across a grain, and reaches the opposite GB, the strain brought about by twinning can be accommodated either by kinking, slip or twinning at the GBs. This process is known as accommodation effects.

Accommodation effects by slip and kinking are of considerable importance for the reversibility of the twin whether by stress removal or stress reversal. The twinning

shear is either accommodated by elasticity in the matrix or by slip or kinking, usually in the matrix [55]. The idea that a twin accommodates plastic deformation without kinking or slip in the matrix is erroneous, although it had dangerously spread in recent literatures. The ability of matrix slip under twinning has a fundamental effect on detwinning, and, as it will be shown in this paper, on pseudo-elasticity.

While kinking may be predominant in single crystals, accommodation effects in polycrystals are mainly provided by slip or another twin (interaction twins). If the GB has a low misorientation, twinning can be readily activated in the adjacent grain. However, if the GB has a sufficiently high misorientation, which happen typically in sharply rod-textures and more randomized textures, slip is necessary or otherwise a crack may nucleate (Figures 1.7 and 1.8) and drive damage [62–64].

However, for largely unconstrained single crystals (SC), the shape change of twinning may be partly accommodated by kinking and/or slip [65–67]. Holden [65] observed that non-basal slip could readily relax any strain incompatibility in HCP single crystals. Unfortunately, such non-basal slip systems tend to be much harder to activate than the basal slip counterparts. These local stress effects correlated to twin deformation are considerably more pronounced in HCP structures than in more commonly used structural materials with FCC or BCC structures. Although the role of twin-accommodation slip in plasticity was cited and emphasized during the nineteen fifties and sixties, current crystal plasticity (CP), and thus, continuum mechanics (CM) models still largely ignore it.

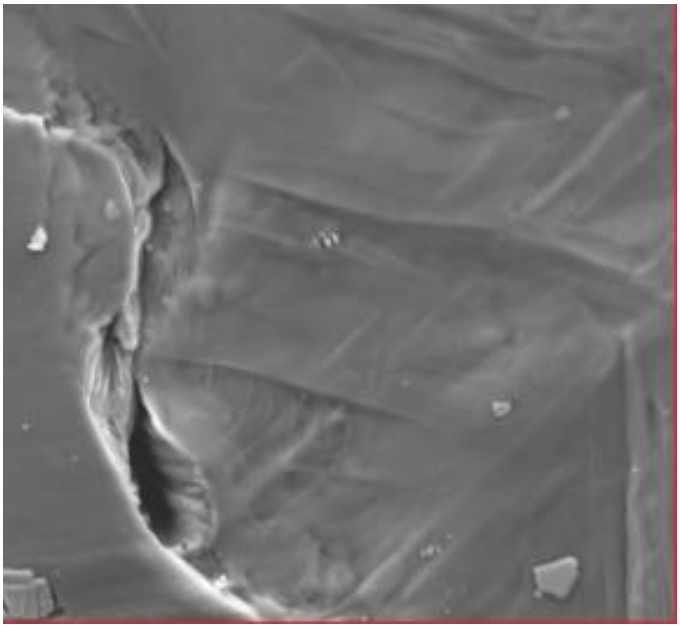

Figure 1.7 SEM obervation of crack nucleation at a grain boundary

SEM micrograph surface relief due to twinning on the right and crack nucleation at the GB, on the left, of an AM30 Mg alloy deformed to 12% plastic strain.

Accounting for GB effects within crystal plasticity-based crystal plasticity models is an active research field [65], and it will be considered in this thesis. Twin-accommodation effects at GBs bear critical implications for damage initiation in HCP structures [5,7]. Zhang et al. [5] recently showed via MD simulations the opening of cracks in BCC molybdenum at a GB into which a deformation twin impinges (Figure 1.8). Here, the effect of low GB misorientation (LGBM) is of considerable importance since it does not only affect the critical resolved shear stress (CRSS) for twinning, it also seems to affect the ease with which slip can accommodate twinning [42,69,70].

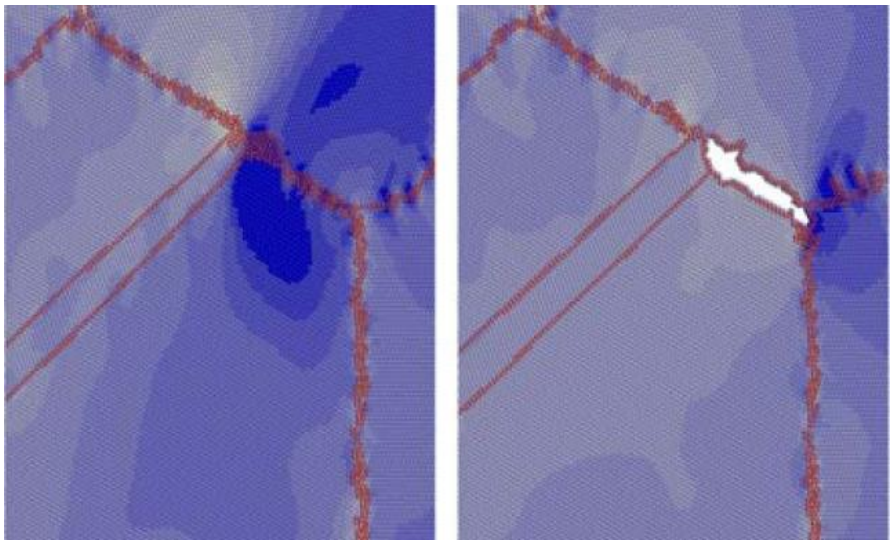

Figure 1.8 Atomic scale simulation of Twin-GB interaction

Twin-GB interaction-induced regions of high stress (dark blue regions) leading to GB crack initiation in Mo according to MD simulations [5]

The difficulty of activating slip might be exacerbated by intergranular particles and solutes, so cracks may readily open as suggested by Remy et al. [71,72]. As described more fully below, twinning has typically been treated within crystal plasticity models as a pseudo-slip type mechanism, where the strain produced is homogenized over the parent crystal [73–75]. The results shown in Figures 1.7 & 1.8 underline the benefits of full-field crystal plasticity modeling. The twinning event is itself a strain localization event, and this must be captured in some way. Further, local interactions with GBs drive the development of "hot stress spot" (highlighted by the dark blue regions in Figure 1.8), accommodation slip, and even fracture initiation.

Finally, all these events are compounded with classical effects of slip on strain incompatibility and thus localization. GBs are lattice orientation discontinuities over which strain incompatibility arises. Local phenomena are more pronounced in triple

junctions and quadruple points where deformation is more than two grains influence the effective lattice rotation. The Taylor model is the most widely used to capture strain compatibility in the grain boundaries [76]. According to the Taylor model, strain-rate is similar over all grains in the polycrystal aggregate, and strain incompatibility at the grain boundaries causes violation of stress equilibrium. The difference in stress state across neighboring grains causes stress gradient in the grain boundaries. Crystallographic slip during plastic deformation of polycrystals or single crystals causes gradual lattice rotation, and thus local changes in grain orientation. However, the lattice rotation is usually not uniform, it causes orientation gradients inside the grain. Literature shows several studies on orientation gradients or local misorientation within grains as result of plastic deformation, these studies include approaches using lattice curvature [77], deformation banding [78] or grain subdivision [79] based on various experimental techniques, most notably misorientation changes across line segments collected by EBSD measurements [80].

1.3 Three-dimensional microstructure measurement

In order to have a correct understanding the role of microstructure on a particular property, measuring a true 3-dimensional polycrystalline microstructure is an essential factor. For instance, 3-dimensional microstructure gives useful information about grain boundaries such as full crystallographic characterization, which is not obtained with 2D measurements. In the following, three main measurement techniques are described.

1.3.1 High-energy X-ray diffraction

High energy X-ray diffraction is a non-destructive method that is able to probe bulk samples and make material space, and time resolved microstructural measurements [81–83]. 3DXRD measurements provide grain orientation and strain information, and track individual grains information during plastic deformation [84]. Moreover, because of fast measurements, X-ray diffraction is a very useful technique to capture dynamic microstructure evolution [85]. Diffraction contrast tomography (DCT) is another type of non-destructive grain mapping, which gives both orientation and shape of each grain [82].

Near-field high energy x-ray diffraction microscopy (nf-HEDM) is another non-destructive technique shown in Figure 1.9b. It has been developed to measure orientation of deformed materials [83,86]. In the same way, far field (ff) HEDM only provide the center mass position of individual grains, and because of its high resolution, it can be utilized to study the evolution of dislocation structures during deformation [87,88]. Combination of Nf-HEDM and ff-HEDM enables us to obtain information from both sub-grain structures as well as stress and strain state of individual grains [89].

1.3.2 Neutron diffraction

Neutron diffraction is another technique, which is used to measure bulk texture and lattice strain during plastic deformation. Moreover, its applications are not limited with the sample size. In the recent publications, this technique has been used to provide bulk texture development and grain scale internal strain in plastic deformation [90]. These grain scale information can be used as input for simulation models [91].

1.3.3 Electron diffraction

Transmission electron microscopy (TEM) and electron backscatter diffraction (EBSD) are electron diffraction methods that can measure spatially resolved orientation and strain information [92,93]. Conventional EBSD or 2D EBSD is a very convenient and effective technique, which provide characterization information such as grain boundaries and grain orientation from the surface of materials. To obtain more detailed information, combination of EBSD and focused ion beam (FIB) provide three-dimensional information from material microstructures (Figure 1.9a) [94]. Three-dimensional EBSD is a surface based technique and destructive to sample, which is its major shortcoming. Therefore, it is not a proper technique to measure three-dimensional microstructure information during plastic deformation.

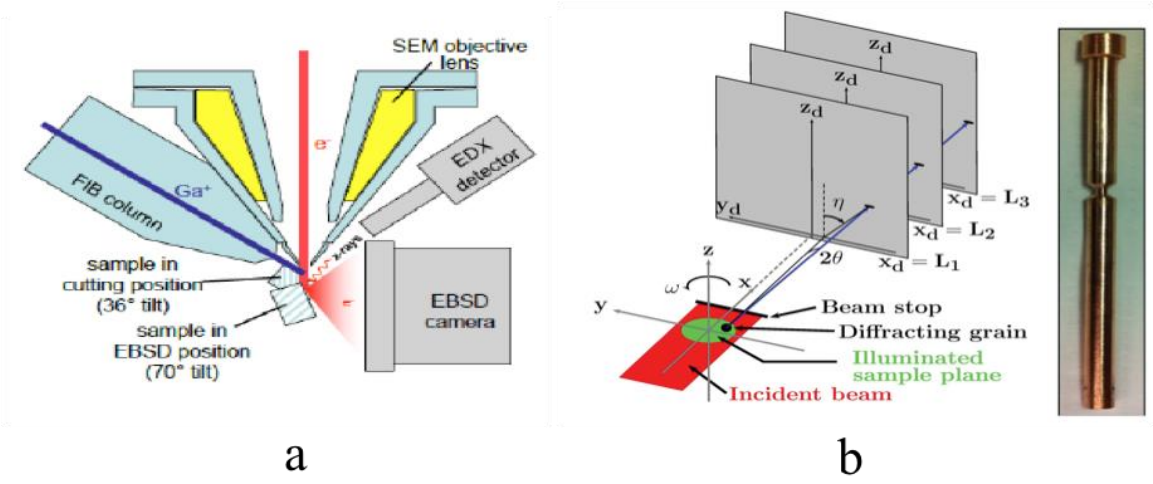

Figure 1.9 Schematics of three dimensional microstructure measurements

Schematics illustrating (a) geometrical set-ups of the EBSD-FIB [94], and (b) mapping measurement techniques with 3D-XRD [95].

1.4 Crystal plasticity modeling

Various crystal plasticity formulations have been developed to numerically predict the macroscopic response such as strain field, stress field and texture evolution after or during plastic deformation.

1.4.1 Statistical Models

Sachs model [96] considers activation of a single slip system, where all individual grains in polycrystalline experiences same stress tensor. According to this model, stress equilibrium is satisfied in grain boundaries, while strain compatibilities are violated in grain boundaries, then, this model gives a lower bound in crystal plasticity prediction of macroscopic behaviors.

An upper bound in crystal plasticity modeling of polycrystalline has been proposed with Taylor and Bishop-Hill [97,98]. Based on their model, all individual grains are subjected to same strain tensor, and activations of multiple slip systems occur to satisfy strain compatibility at grain boundaries. To minimize the work expanded on each slip system, at least five-slip systems must be active to satisfy strain compatibility. This model is a Full constraint (FC) model, and stress equilibrium is violated at grain boundaries. FC model is very successful in prediction of deformation texture [99].

Viscoplastic self consistant (VPSC) is the most popular statistical method, which has been used to predict texture evolution and macroscopic field during plastic deformations [100]. This model is most commonly used in cubic and non-cubic materials. It considers each grain as a single crystal inclusion embedded in an effective viscoplastic medium with anisotropic properties. Ultimately, to compute macroscopic behavior of

polycrystalline, an incompressible viscoplastic constitutive equation is used to define local material response.

1.4.2 Microstructure based Models

Crystal plasticity finite element method (CPFEM) is the first and most commonly used method based on material microstructure as input, which considers grain interaction and provide full field solution to compute texture and stress/strain field during deformation [101,102]. CPFEM computes full field solution in elasto-plastic deformation, and slip systems are considered as main mechanism involved in the plastic deformation process [103]. In CPFEM, input microstructure is meshed with significant number of element to give a more accurate solution. Generating meshes that conform to grain boundaries is time consuming. Moreover, FE method generally runs in order of N^2, so a problem with many degrees of freedom such crystal plasticity problem takes a long time to be solved.

In contrast to FEM, fast Fourier transform (FFT) is a very good alternative that does not suffer from mesh complexity and slow running time. This method provides a full-field solution by considering the interaction of one point with other point in the image of initial microstructure [104,105]. Furthermore, absence of meshing requirement enables us to use large input images for the deformation simulation. The method will be described in more detail in the following.

Gibbs' phenomenon corresponds to the large oscillation that Fourier series of a piecewise continuously differentiable periodic function exhibits at a discontinuity. It leads to an over prediction of the values at the discontinuity compared with those given with the analytical solution by approximately 9% [106]. In particular, for full-field FFT

crystal plasticity simulations, this artifact tends to shield and perturb the effects of grain boundaries on stress localization [107]. Therefore, Gibbs' phenomenon is a characteristic disadvantage of FFT crystal plasticity compared to CPFEM. [108]. In the literature, several solutions were suggested from utilizing a filter [106], to increasing Fourier point numbers in excess to 128 points [109], and performing calculation on odd grid numbers [109].

1.5 Crystal plasticity based on Fast Fourier transforms (FFT).

The first application of FFT has been proposed by Moulanic and Suquet [105]. First, they used FFT to calculate micro-mechanical problem of linear elastic composite, and later extended to non-linear two-phase isotropic materials. Finally, Lebensohn combined crystal plasticity (CP) with FFT to calculate full field solution in viscoplastic polycrystalline materials [104].

The CPFEM, which uses the microstructure as an input, is undoubtedly the most popular based crystal plasticity formulation, commercially implemented to solve plasticity problems. However, it suffers from degrees of freedom in the problems with large complex microstructure. Furthermore, CPFEM shows difficulties in generating mesh, which conform to the interface in the microstructure with complex morphology, while meshless methods such as CPFFT can easily overcome these complexities. The accuracy of the solution in both CPFFT and CPFEM is a function of input microstructural image, but this dependency is stronger in CPFEM. In addition, crystal plasticity based on FFT formulation is solved in each voxel independently, thus, the CPFTT can be easily parallelized, and adapted on supercomputers with multiple processors, which is an effective way to decrease computational running time.

To apply FFT, the input must be discretized to $N1 \times N2 \times N3$ Fourier points and a periodic boundary condition is applied, which is a requirement of FFT calculation. A regular space grid is laid on the microstructure in three or two dimension; a center-wieght voxel, in three dimensions, or a center weight pixel, in two dimensions, is created at each grid point. Figure 1.10 shows an illustration of a pixelized microstructure.

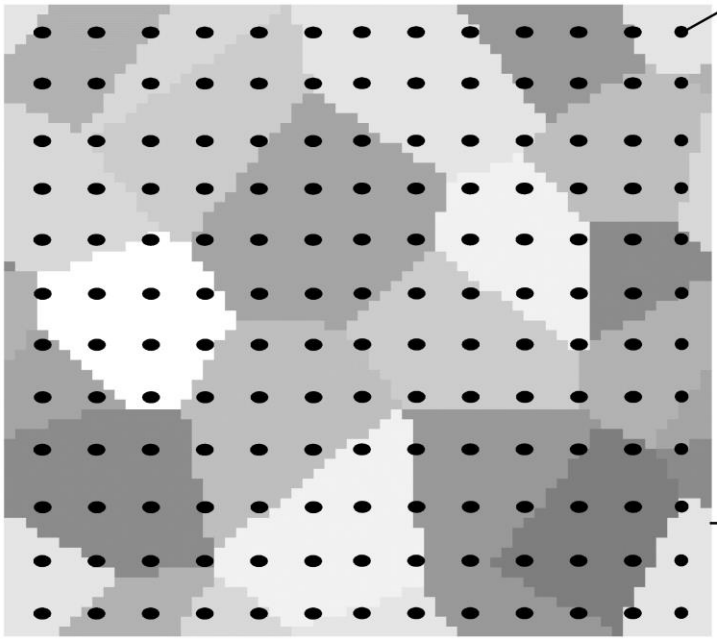

Figure 1.10 An artificially-constructed microstructure overlaid with regular Fourier grid.

In CPFFT method, the relation between local stress and strain/strain-rate is given with a constitutive equation. This method uses Green's function to compute local response of the heterogeneous medium, and strain compatibility is satisfied at each point with solving stress equilibrium at each point.

CPFFT formulation is based on augmented Lagrangian (AL) [110] iterative scheme, which compute local stress and strain/strain-rate when the unit cell is subjected to external loading boundary conditions. After reaching convergence, an equilibrated stress is obtained from a non-linear constitutive equation, and consequently, stress equilibrium and strain compatibility are satisfied at the same time. FFT based formulations have been developed for elastic, viscoplastic, and elasto-viscoplastic [111] constitutive behaviors to compute full field solution in polycrystalline deformation. In the following, we describe elastic formulation based on FFT, which is extended to viscoplastic and elasto-viscoplastic constitutive formulations.

1.5.1 Elastic case

An elastic constitutive relation between stress and strain field at a single crystal material point X is given by

$$\sigma_{ij}(x) = C_{ijkl}(x)\epsilon_{kl}(x) \qquad (1.1)$$

where $C_{ijkl}(x)$ is the anisotropic stiffness tensor at each point X of the representative volume element (RVE). To compute local-micromechanical field, a full-field solution method is used to solve the above equation for inhomogeneous elastic medium. With considering a homogenization approach, elastic constant of medium C^0 is calculated as the average of $C_{ijkl}(x)$. The local strain can be split as following:

$$\epsilon_{ij}(x) = E_{ij} + \tilde{\epsilon}_{ij}(x) \qquad (1.2)$$

where $\dot{E}_{ij}$ and $\tilde{\epsilon}_{ij}(x)$ are applied macroscopic strain and a periodic fluctuation strain at point X, respectively. The fluctuation strain can be expressed in terms of fluctuation displacement:

$$\tilde{\epsilon}_{ij}(x) = (\tilde{u}_{ij}(x) + \tilde{u}_{ij}\,(x)) \qquad (1.3)$$

Then, with adding and subtracting the average stress, local stress at each Fourier point is given by the following equations:

$$\sigma_{ij}(x) = \sigma_{ij}(x) + C^0{}_{ijkl}\,\epsilon_{kl}(x) - C^0{}_{ijkl}\epsilon_{kl}(x) \qquad (1.4)$$

$$\sigma_{ij}(x) = (\sigma_{ij}(x) - C^0{}_{ijkl}\,\epsilon_{kl}(x)) + C^0{}_{ijkl}\epsilon_{kl}(x) = C^0{}_{ijkl}u_{kl}(x) + \phi_{ij}(x) \qquad (1.5)$$

where $\phi_{ij}(x)$ is the polarization field, which means the deviation of local stress field from the average one. After applying stress equilibrium condition $\sigma_{ij,j}(x) = 0$ on equation (1.5), we will have:

$$C^0{}_{ijkl}\tilde{u}_{k,lj}(x) + \phi_{ij,j}(x) = 0 \qquad (1.6)$$

Equation (1.6) is a homogeneous differential equation, which can be solved with Green's function for a periodic unit cell under an average strain $E_{ij} =< \epsilon_{ij}(x) >$, and it can be written in terms of Green's function as:

$$C^0{}_{ijkl}G_{km,lj}(x - x') + \delta_{im}\delta(x - x') = 0 \qquad (1.7)$$

where G_{km} is Green's function associated with fluctuation displacement field $\tilde{u}_k(x)$, and δ is dirac delta function associated with polarization field ϕ_{ij}. Then, the local displacement at each Fourier point is given by,

$$\tilde{u}_k(x) = -\int G_{ki}\,(x - x')\phi_{ij,j}(x')dx' \qquad (1.8)$$

Solving equation (1.8) in real space is difficult and time consuming, the equation is transformed into Fourier space, where the convolution integral can be solved with multiplication of polarization field and Green function in Fourier space, equation (1.8) in Fourier space becomes

$$\hat{u}(K) = \hat{\Gamma}_{ijkl}{}^{0}(K)\widehat{\phi_{kl}}(K) \quad (1.9)$$

where K is the point in the Fourier space, and $\hat{\Gamma}_{ijkl}{}^{0}$ is Green's function in Fourier space as well, Green's Function in Fourier space is given by:

$$\hat{\Gamma}_{ijkl}{}^{0}(K) = -K_j K_l \hat{G}_{ik}(K) \quad (1.10)$$

$$\hat{G}_{ik}(K) = [C^0{}_{kjil} k_l k_j]^{-1} \quad (1.11)$$

Furthermore, due to requirement of FFT algorithm to a periodic boundary condition, a periodic boundary is assumed across RVE. Local fluctuation strain is given in Fourier space by

$$\hat{\epsilon}_{ij}(K) = \hat{\Gamma}^{0sym}{}_{ijkl}(k)\hat{\phi}_{kl}(k) \quad (1.12)$$

After back transform to real space, the compatible strain field is written as,

$$\epsilon_{ij} = E_{ij} + FT^{-1}(\hat{\epsilon}_{ij}(K)) \quad (1.13)$$

If a known perturbation field is available, the local strain field can be easily calculated from the above equations. However, due to the initial unknown fluctuation term at each point X, an iterative scheme is implemented to calculate local strain at each point X. In the iterative scheme, with (i)th guess for $\epsilon^{i}{}_{ij}(x)$ used in equation (1.1)-(1.3) and (1.5)-(1.6), $\epsilon^{i+1}{}_{ij}(x)$ is obtained at (i+1)th iteration. Finally, with a proper

convergence criterion, the algorithm terminates when both stress equilibrium and strain compatibility are satisfied at the same time.

1.5.2 Viscoplastic case

In the Viscoplastic based on FFT (vpFFT), the elastic strain is considered very small compared to plastic one, and the relation between local deviatoric stress $\acute{\sigma}(x)$ and strain-rate $\dot{\mathcal{E}}_{ij}(x)$ at each point X is given by the following well known crystal plasticity equation.

$$\dot{\mathcal{E}}_{ij}(x) = \dot{\gamma}_0 \sum_{s=1}^{N} m_{ij}^{s}(x) \left(\frac{m_{ij}^{s}(x):\acute{\sigma}(x)}{\tau^{s}(x)}\right)^{n} \operatorname{sgn}\left(m_{ij}^{s}(x):\acute{\sigma}(x)\right) \qquad (1.14)$$

According to this equation, activation of slip and twinning mechanisms produces strain-rate during plastic deformation. $m_{ij}^{s}(x)$ is schmid tensor on slip or twin system, $\dot{\gamma}_0$ and $\tau^{s}(x)$ are the reference shear rate and critical resolved shear stress on each slip or twin system, respectively. N is summation of active twin and slip system in plastic deformation.

The macroscopic velocity V_{ij} is applied on the periodic unit cell, and can be decomposed into symmetric $\dot{E}_{ij}$ and antisymmetric $\dot{\Omega}_{ij}$ tensor.

$$V_{ij} = \dot{E}_{ij} + \dot{\Omega}_{ij} \qquad (1.15)$$

where $\dot{E}_{ij}$ and $\dot{\Omega}_{ij}$ are strain rate and rotation rate tensor, respectively. The local strain rate and rotation rate is given by,

$$\epsilon_{ij} = \frac{1}{2}(v_{i,j} + v_{j,i}) \qquad (1.16)$$

$$\dot{\omega}_{ij}(x) = \sum_{s}^{N} \alpha^{k}{}_{ij}(x)\dot{\gamma}^{s} \qquad (1.17)$$

where ${\alpha^k}_{ij}$ is anti-symmetric Schmid tensor. The local strain–rate is decomposed to average strain-rate and local strain fluctuation at each point X as,

$$\dot{\epsilon}_{ij}\big(v_k(x)\big) = \dot{E} + \tilde{\epsilon}_{ij}(\tilde{v}_k(x)) \quad (1.18)$$

$$v_k(x) = \dot{E}x_k + \tilde{v}_k(x) \quad (1.19)$$

The velocity field is assumed periodic across boundary, and to assure stress equilibrium condition in the boundaries of unit cells, traction vector is anti-periodic across the boundaries. The Cauchy stress for incompressible material is given by,

$$\sigma_{ij}(x) = {L^0}_{ijkl}(x)\dot{\epsilon}_{kl}(x) + \phi_{ij}(x) - p(x)\delta_{ij} \quad (1.20)$$

where $p(x)$ and ${L^0}_{ijkl}$ are the hydrostatic pressure and stiffness of reference medium, respectively. With applying stress equilibrium, and considering strain compatibility, equation (1.20) becomes

$${L^0}_{ijkl}(x)v_{k,lj}(x) + \phi_{ij,j}(x) - p(x) = 0 \quad (1.21)$$

$$v_{k,k} = 0 \quad (1.22)$$

Likewise for the elastic case, equation (1.21) is solved by using Green's function method, and the convolution integral associated with Green's function and polarization function is written as:

$$\tilde{v}_k(x) = \int G_{ik,jl}\,(x - x')\phi_{kl}(x')dx' \quad (1.23)$$

Forward transforming of the above integral to Fourier space and solving the convolution integral gives local strain field in Fourier space as,

$$\hat{\dot{\epsilon}}_{ij}(k) = {\hat{\Gamma}^{0\,sym}}_{ijkl}(k)\hat{\phi}_{kl}(k) \quad (1.24)$$

Similar to the elastic case, $\hat{\Gamma}^{0\,sym}{}_{ijkl} = \mathrm{sym}\left(G_{ik,jl}\right)$, the polarization field can be calculated using the FFT based formulation. More robust and involved iteration based on the augmanted lagrangian method (AL), adapted from Michel et al. [110], which converge faster, is implemented in VPFFT formulation [112]. The diviatoric local stress field, $\acute{\sigma}(x)$, associated with compatibility constraint, is considered as initial guess for Lagrange multiplier field in the iteration. If the polarization field is known from the (i)th iteration, The new guess for the fluctuation at (i+1)th iteration is given by:

$$\hat{e}^{(i+1)}(k) = -\hat{\Gamma}^{0\,sym}(k) : \hat{\phi}^{(i)}(k) \qquad (1.25)$$

$$\forall K \neq 0, and\ \hat{e}^{(i+1)}(0) = 0 \qquad (1.26)$$

Local strain rate in real space is written as,

$$\tilde{e}^{(i+1)} = FT^{-1}\left(\hat{e}^{(i+1)}(k)\right) \qquad (1.27)$$

The new guess for local stress at (i+1)th iteration is computed from

$$\sigma'^{(i+1)}(x) + L^0 : \dot{\epsilon}^{(i+1)}(x) = \lambda^i(x) + L^0 : \dot{e}(x) \qquad (1.28)$$

where $\lambda^i(x)$ is Lagrange multiplier field at iteration (i)th, and the new guess for Lagrange multiplier at next iteration is given by:

$$\lambda^{(i+1)}(x) = \lambda^{(i)}(x) + L^0(\dot{\epsilon}^{(i+1)}(x) - \dot{e}^{(i+1)}(x)) \qquad (1.29)$$

Strain-rate field $\dot{\epsilon}$ is related to stress field constitutively, and convergence happens when both strain-rate field $\dot{\epsilon}$ and kinematically admissible auxiliarly strain-rate field $\dot{e}$ meet the same value to fulfill strain compatibility. Then, the Lagrange multipler λ field converges to the stress field σ to satisfy equilibrium condition [110,113]. Both equation

(1.28) and (1.29) guarantee that stress equilibrium and strain compatibility occurs at the same time.

1.5.3 Elastic viscoplastic case

Elastic viscoplastic (EVP) formulation considers both elastic and plastic strain evolution during deformation. The relation between local stress and elastic strain at each point X is given by,

$$\sigma_{ij}(x) = C_{ijkl}(x)\epsilon^{e}{}_{kl}(x) \quad (1.30)$$

where $C_{ijkl}(x)$ and $\epsilon^{e}{}_{kl}(x)$ is local elastic stiffness and elastic strain at each point X, with the following formulation, we can express local stress in terms of total strain and plastic strain,

$$\epsilon^{e}{}_{ij} = \epsilon_{ij} - \epsilon^{p}{}_{ij} \quad (1.31)$$

$$\sigma_{ij}(x) = C_{ijkl}(x)\epsilon^{e}{}_{kl}(x) = C_{ijkl}(x)(\epsilon_{ij} - \epsilon^{p}{}_{ij}) \quad (1.32)$$

$$\sigma^{t+\Delta t}(x) = C(x)\epsilon^{e,t+\Delta t} = C(x)(\epsilon^{t+\Delta t}(x) - \epsilon^{p,t} - \dot{\epsilon}^{p,t+\Delta t}(x, \sigma^{t+\Delta t})\Delta t \quad (1.33)$$

where $\sigma(x)$ is the Cauchy stress at point x, $C(x)$ is elastic stiffness tensor, ϵ_{ij} , $\epsilon^{e}{}_{ij}$, $\epsilon^{p}{}_{ij}$, $\dot{\epsilon}^{p}$ are total, elastic, plastic strain, and plastic strain-rate at each point X, respectively. As shown in equation (I-33), Local plastic strain is computed from plastic strain rate in equation (I-14) with Euler time discretization, and total strain is given by,

$$\epsilon(x) = C^{-1}(x)\sigma(x) + \epsilon^{p} + \dot{\epsilon}^{p}\Delta t \quad (1.34)$$

Similar to elastic and viscoplastic case, average stiffness C^{0} is computed by averaging over local striffness at each point X. Constitutive law between local stress and displacement is given by,

$$\sigma_{ij}(x) = C^0{}_{ijkl}u_{k,l}(x) + \sigma_{ij}(x) - C^0{}_{ijkl}u_{k,l}(x) \quad (1.35)$$

$$\sigma_{ij}(x) = C^0{}_{ijkl}u_{k,l}(x) + \phi_{ij}(x) \quad (1.36)$$

where ϕ_{ij} is polarization factor, which means deviation of local field from average medium field. Likewise elastic and viscoplastic case, the compatible strain field is given by solving convolution integral of Green's function and polarization field in Fourier space.

$$\epsilon_{ij}(x) = E_{ij} + FT^{-1}(Sym(\hat{\Gamma}^0{}_{ijkl}(K)\hat{\phi}_{kl}(K) \quad (1.37)$$

where $\hat{\Gamma}^0{}_{ijkl}$ and $\hat{\phi}_{kl}$ are Green operator and polarization function in Fourier space, K is a frequency in Fourier space. An iteration scheme based on augmented lagrangian (AL) like VPFFT case is used on EVP formulation. Local stress $\sigma\ (x)$ and elastic strain is considered as initial guess for auxiliary stress and strain. Provided the polarization field is known at iteration $(i)^{th}$, local strain at iteration $(i+1)^{th}$ is given by;

$$e^{(i+1)}{}_{ij}(x) = E_{ij} + FT^{-1}(\hat{e}^{(i)}{}_{ij} + sym(\hat{\Gamma}^0{}_{ijkl}(K)\hat{\lambda}^{(i)}{}_{kl}(K)) \quad (1.38)$$

In contrast to VPFFT case, an alternative fix point approach has been used, which compute compatible strain as result of multiplication between stress field and Green operator in Fourier space (equation 1.38). To compute new guess for stress field, Lebensohn et al. [111] used following modification on augmented Lagrangian (AL) to be more robust and to converge faster.

$$R_k(\sigma^{(i+1)}) = \sigma^{(i+1)}{}_k + C^0{}_{kl}\epsilon^{(i+1)}{}_l\left(\sigma^{(i+1)}\right) - \lambda^{(i)}{}_k - C^0{}_{kl}e^{(i+1)}{}_l = 0 \quad (1.39)$$

This scheme needs nullification of a residual R at each point X, and this residual is a function of stress field $\sigma^{(i+1)}$, constitutively related with strain tensor $\epsilon^{(i+1)}$ at each iteration, and finally, new guess for lagrangian multiplier is given by

$$\lambda^{(i+1)}(x) = \lambda^{(i)}(x) + C^0 : (e^{(i+1)}(x) - \epsilon^{(i+1)}(x)) \qquad (1.40)$$

When $(e^{(i+1)}(x) - \epsilon^{(i+1)}(x))$ is smaller than a predefined threshold, convergence happens and EVPFFT algorithm goes to next deformation step. Similar to VPFTT, up on the convergence, both stress equilibrium and strain compatibility is satisfied at the same time.

CHAPTER II

EFFECT OF DIFFERENT DEFORMATION MODES ON LOCAL HETEROGENEITIES IN A THREE DIMENSIONAL FERRITIC STEEL MICROSTRUCTURE

2.1 Abstract

We investigated the effect of macroscopic deformation modes (i.e. tension, compression, plane strain and torsion) on a real three-dimensional ferritic steel microstructure obtained by three-dimensional (3D) serial sectioning EBSD. To compute local lattice reorientation, strain rate and stress, a 3D full-field viscoplastic formulation based on fast Fourier transformation (VPFFT) was used. Kernel average misorientation (KAM) and local Taylor factor were calculated based on the orientation at each Fourier point. The calculated local stress, strain rate, Taylor factor, and KAM values were categorized according to (Euclidean) distance maps for three different microstructural features: grain boundaries, triple junctions and quadruple points. The results show that low and high values of local stress, strain rate, Taylor factor, and mainly high values of KAM all lie close to the microstructural features in all deformation modes. The width of high strain rate regions adjacent to grain boundaries depends on stress state in tension, compression, and plane strain, whereas the torsion mode results in hot spots distributed throughout the grains. Taylor factor and KAM exhibit a strong correlation with local

stress and local stress gradient, respectively, which varies to some degree with deformation mode.

2.2 Introduction

Plastic deformation of polycrystalline metals is heterogeneous in grain scale, and several researches have been performed to realize deformation gradient inside of grains. New characterization tools such as electron backscatter diffraction (EBSD) and 3D synchrotron X-ray diffraction have been used to investigate grain scale heterogeneities [114,115]. Strain heterogeneity is known to occur near grain boundaries, triple lines and quadruple points, which are all discontinuities in orientation. The jumps in orientation from one grain to the next across these boundaries can cause jumps in stress and strain incompatibility near the boundaries. For general inclusions (could be a grain) with a "perfect" interface, displacements and interface tractions across the interface must be continuous. However, there may be a jump in the displacement gradient normal to the interface, while that along the interface remains continuous. The Taylor model is widely used to approximate the anisotropic response of polycrystals and assumes uniform strain (rate), thus compatibility is automatically satisfied and at grain boundaries in particular [116]. By assuming uniform strain rate for all grains in the polycrystalline aggregate, which is a strong assumption about local boundary conditions, much success has been obtained in texture prediction [117]. However, grains have different neighborhoods, and thus different stress vertices, to be reached by the local stress in order to satisfy compatibility that is aggravated by grain-grain interactions. A grain is forced to deform in a polyslip condition, as it is unable to deform independently from its neighbors. The change in stress direction from the single crystal deformation condition (early strain) to

the interacting grain condition, upon increasing plastic strain, is usually tracked by the change in elastic strain direction. The inevitable changes in stress state from a grain to another one means that stress gradients will be the largest across grain boundaries and stress equilibrium is clearly violated there.

The local Taylor factor is essentially used to measure the amount of plastic work required to deform the polycrystal at a given location. A few studies have shown that the variation of local Taylor factor from one grain to another one correlates with damage susceptibility and thus failure. For instance, Wright and Field [118] showed that grains with low Taylor factors adjacent to those with high Taylor factor are more susceptible to develop stress concentrations. Furthermore, Taylor factor value is an effective criterion to explain the sources of void nucleation, for example, voids nucleate more frequently in the regions with both hard and soft orientations than in the regions with a high Taylor factor [119]. On the other hand, void development mostly happens at grain boundaries between soft orientation where incompatible shape changes are in results of differential strains from predominant slip systems [120,121].

To measure experimentally the relation between local strain and orientation, some techniques such as digital image correlation (DIC) and electron backscatter diffraction (EBSD) can be used. DIC that provides full-field strain measurements in the microstructure [122,123] was coupled with EBSD to determine strain in grain interiors and close to grain boundaries. The results showed strain concentration near grain boundaries. The magnitude of plastic strain variation across boundaries was related to the residual Burger vectors. Two types of regions near grain boundaries were identified, *viz*.

regions with low and high strain associated with GB shielding, versus regions with slip transmission across the boundary and therefore minimal strain concentrations [124,125].

Crystallographic slip during plastic deformation of polycrystals or single crystals causes gradual lattice rotation, and thus local changes of grain orientation. However, the lattice rotation is usually not uniform, it causes orientation gradients inside the grain. Studies of orientation gradients or local misorientation within grains as result of plastic deformation have shown orientation gradients as lattice curvature [77], deformation banding [126] or grain subdivision [78] where the material has not been deformed severely (e.g. bulk torsion). EBSD measurements have also confirmed the existence of orientation gradients between the grain center and boundaries from uniaxial tension [80].

Three-dimensional (3D) crystal plasticity finite element method (CPFEM) was used to model heterogeneity of stress, strain and orientation gradient at the grain scale [127,128]. For instance, Lewis *et al*. [129–131] performed 3D CPFEM simulations based on a measured 3D microstructure, grain morphology, grain boundary and connectivity under different loading conditions. Their results confirmed that the local von Mises stress is the highest near grain boundaries (GBs) and triple junctions (TJs).

To decrease computational time and avoid meshing complexities associated with CPFEM such as generating a good quality mesh that conforms to the grain boundary network, the viscoplastic full-field solution based on the fast Fourier transform (VPFFT) was proposed by Lebensohn [132–134], which in turn was based on work by Moulinec and Suquet [135] for composite materials. Using VPFFT, Rollett *et al*. [136] identified stress localization near GBs, TJs and quadruple points (QPs) for different 3D microstructures.

In this work, we are concerned with deciphering the effect of imposed macroscopic deformation modes on local stress, strain and average misorientation, with the motivation to infer how the microstructure responds to the loading condition in terms of damage susceptibility. We instantiate the VPFFT simulations with a measured 3D microstructure of BCC steel obtained by 3D electron backscatter diffraction (EBSD) serial sectioning. Four different deformation paths (i.e. tension, compression, plane strain compression, and torsion) were applied to the real 3D ferrite microstructure. Appropriate algorithms were developed to statistically analyze the localization behavior with respect to microstructural features including GBs, TJs, and QPs for each loading condition. Next, the effect of loading boundary conditions was investigated on correlation between Taylor factor and local stress and strain rate. Finally, we investigated the correlation between kernel average misorientation (KAM) and stress gradient in different deformation modes.

2.3 Experimental procedure

2.3.1 Sample preparation and mechanical testing

A fully ferritic steel with composition 0.04 C-1.52 Mn-0.2 Si -0.22 Mo-0.08 Ti-0.33 Al (wt%) was used in the current study. The material was received in a rolled slab condition having 40 mm in thickness. Hot rolling was performed to reduce the thickness to 12 mm. A plane-strain compression specimen with a dimension of 300×300×10 mm was machined out of the hot rolled plate with its long length perpendicular to the rolling direction. The specimen was reheated at 5 °C/s to 1200-°C and held for 300-s. It was then cooled down to 890°C, held for 20 s, and then deformed to a strain of 1 at a strain rate of 1 s^{-1}. Afterwards, the deformed specimen was cooled to 650 °C at 10 °C/s and held for 600 s followed by water quenching. This thermomechanical procedure was employed to

refine the ferrite grain size and consequently achieve a high population of grains within the volume that can be analyzed by three-dimensional EBSD mapping. The final microstructure consisted of fully polygonal ferrite grains having an average grain size of ~6 μm.

The compression device was a servo hydraulic thermomechanical treatment simulator apparatus (Servotest, 500 kN) equipped with an automated testing machine including an induction furnace, a muffle furnace and a computer data-acquisition system. Temperature was monitored throughout the testing using a thermocouple embedded into the specimen. A boron nitride lubricant was used to coat the specimen and minimize the friction between the contact surfaces of the specimen and anvils during deformation.

To quantify the mechanical property of the material, sub-size tensile specimens with a gauge of 20 mm×2 mm×2 mm were machined by wire-cutting out of thermomechanically processed sample. The tensile axis was perpendicular to the deformation direction. Tensile testing was performed using an Instron tensile testing machine with a crosshead displacement rate of 7.2 mm/min (i.e. corresponding to a nominal strain rate of 10^{-3} s^{-1}.

2.3.2 Three dimensional EBSD Measurement

To construct a 3D orientation map of the microstructure, 3-D EBSD measurement with automatic serial sectioning was performed on a rectangular specimen. The specimen was extracted from the center of the deformed sample compressed normal to the loading axis. The thickness of the sample was reduced to approximately 150 μm through mechanical grinding and polishing. EBSD mapping was carried out using under a voltage

of 20 kV and a current of 8 nA. EBSD scans were performed with a step size of 150 nm. In each sectioning step, 200 nm was removed using a 30 kV, 5 nA Ga^+ ion beam. The average confidence index generally changed between 0.60 and 0.70. More details on 3D-EBSD characterization routine can be found in [137].

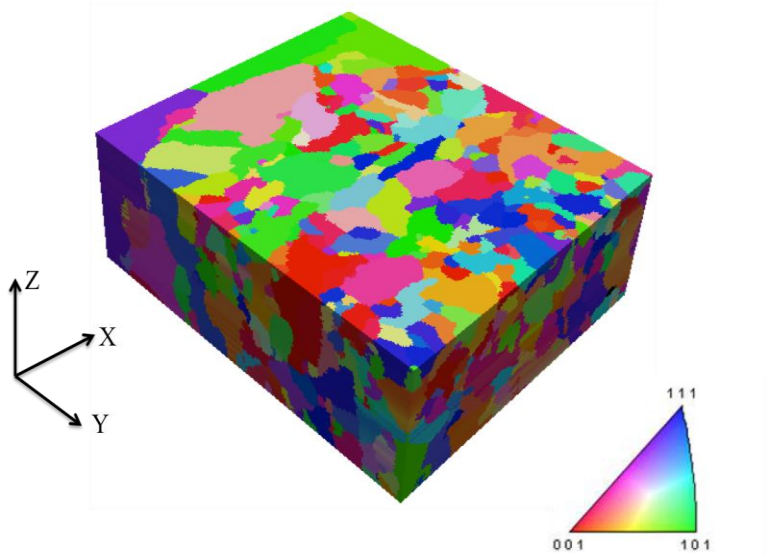

Figure 2.1 Three dimensional reconstructed microstructure of a Ferritic steel

Three dimensional reconstructed microstructure of a Ferritic steel obtained by 64 serial sections with electron backscatter diffraction. The orientations are colored according to an inverse pole figure for the X direction, see inset bottom right.

To create 3D reconstructed microstructure, the serial sectioned data was placed in a 3D framework using the software package Dream.3D [138]. During reconstruction process the following cleaning step was applied. First, to remove ambiguous data, a grain dilation was applied in each layer, then a single average orientation was assigned to each grain in three dimensional, finally grains smaller than 30 voxels were merged with the neighboring grains having the highest number of voxels. The 3D Ferritic microstructure

containing 1276 grains was constructed with dimensions $234 \times 267 \times 68$ voxels (Figure 2.1).

2.4 FFT Method and hardening rules

The FFT viscoplastic formulation computes a local compatible strain-rate field in each point when the unit cell undergoes a macroscopic strain rate $\dot{E}_{ij}$ [20,21]. Due to a priori unknown value for strain-rate field, an iteration scheme based on augmented Lagrangian [140] was adopted to compute local strain rate field at each strain increment. Up on convergence, local strain rate field, related constitutively to stress, becomes equal to the kinematically admissible strain rate field to satisfy compatibility condition. As a consequence, the Lagrange multiplier field converges toward stress field to fulfill stress equilibrium. The readers are referred to references [134,139] for further detailed information.

The local constitutive relation between strain-rate $\dot{\mathcal{E}}_{ij}(x)$ and the deviatoric stress $\acute{\sigma}(x)$ is given with a commonly used crystal plasticity equation:

$$\dot{\mathcal{E}}_{ij}(x) = \dot{\gamma}_0 \sum_{s=1}^{N} m_{ij}^{s}(x) \left(\frac{m_{ij}^{s}(x) : \acute{\sigma}(x)}{\tau^{s}(x)} \right)^{n} sgn\left(m_{ij}^{s}(x) : \acute{\sigma}(x) \right) \qquad (2.1)$$

Summation N runs over all slip N_s systems, τ^s and m^s are the threshold shear stress and Schmid tensor associated with each slip system, respectively. $\dot{\gamma}_0$ is a normalization factor and n is the rate sensitivity exponent.

The critical resolved shear stress (CRSS) increases with accumulated shear strain Γ in each point (each grain). For VPFFT, the evolution of CRSS with shear strain is described with the extended Voce law-hardening model:

$$\tau_s(\Gamma) = \tau_0 + (\tau_1 + \Theta_1\Gamma)\left[1 - exp\left(\frac{-\Theta_0\Gamma}{\tau_1}\right)\right] \quad (2.2)$$

$$\Gamma = \int_0^t \sum_s |\dot{\gamma}| dt \quad (2.3)$$

τ_0 and θ_0 are the initial shear stress and hardening rate, while τ_1 and θ_1 are the saturation stress and hardening rate, respectively. The solution to Eq. (II-1) provides the slip rates used in Eq. (II-2).

Activation and interaction of slip systems causes hardening, so an expression is needed to capture how hardening increases the CRSS of each slip system:

$$\dot{\tau}^s = \frac{d\tau^s}{d\Gamma} \sum_{\acute{s}} h^{s\acute{s}} \dot{\gamma}^{\acute{s}} \quad (2.4)$$

Here $\frac{d\tau^s}{d\Gamma}$ and $h^{s\acute{s}}$ are self and latent hardening parameters between different slip systems, respectively.

To use the MPI-parallel FFT algorithm, the dimensions of the simulation volume should be power-of-two. 22 buffer layers were added in the *x* direction to make a simulation volume with dimension of $256\times 256 \times 64$. Figure 2.2 shows inverse pole figures (IF) of simulation volume. There is a strong <111> fiber parallel to X direction.

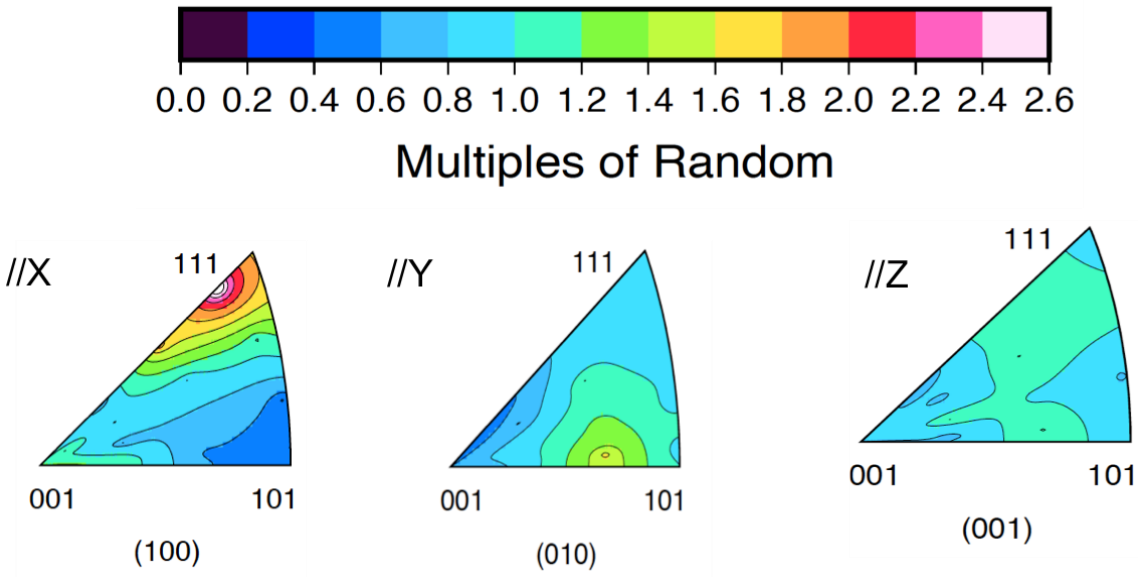

Figure 2.2 Inverse pole figures (IPF) of the input microstructure

Showing a mild <111> fiber texture parallel to the X direction of the 3D ferritic steel microstructure**.**

VPFFT simulations were performed to simulate four different strain paths by imposing macroscopic strain-rate of four deformation modes in step of 0.01 von Mises strain to a maximum strain of 0.3, as described in Table 2.1.

Because of existence of experimental data for tensile sample, first, the Voce law hardening parameters were determined based on the best fit between experimental and simulation result (see Table 2.2). Then, with the fitted parameters stress- strain curves of the three other deformation modes (compression, plane strain and torsion) were simulated.

Table 2.1 Four different deformation path imposed on the unit cell

Tension			Compression			Plane Strain			Torsion		
-0.5	0	0	0.5	0	0	0	0	0	0	0	0
0	1.0	0	0	-1.0	0	0	0.866	0	0	0	0.866
0	0	-0.5	0	0	0.5	0	0	-0.866	0	0.866	0

VPFFT simulations were performed to simulate four stress states by imposing macroscopic strain-rate of four deformation modes in step of 0.01 von mises strain to a maximum strain of 0.3 described in Table 2.1.

Because of existence of experimental data for tensile sample, first, the voce law hardening parameters were found based on the best fit between experimental and simulation result (Table 2.2). Then, with the fitted parameters stress- strain curves of the three other deformation modes (compression, plane strain and Torsion) were simulated.

Table 2.2 Voce law hardening parameters of the three slip modes resulting from the best fit between predicted and experimental tensile test along X (RD)

	τ_0	τ_1	θ_0	θ_1
{110}<111>	266	54	878	103
{112}<111>	256	54	878	103
{123}<111>	266	54	878	103

2.5 Results and Discussion

2.5.1 Simulated Macroscopic stress-strain curves

For simplicity, slip in a body center cubic (BCC) structure is assumed to occur along different planes all with a <111> slip direction. The three slip modes, namely {110} <111>, {112} <111>, and {123} <111>, contain 48 slip systems in total. To predict the macroscopic stress-strain curve, all three-slip modes are considered. In previous endeavors [141], the value of initial critical shear stress on {112} plane was

considered less than those associated with the two other slip modes. Table 2.2 summarizes our Voce hardening law parameters, which we identified for each slip system by fitting the tension stress-strain curve in Figure 2.3.

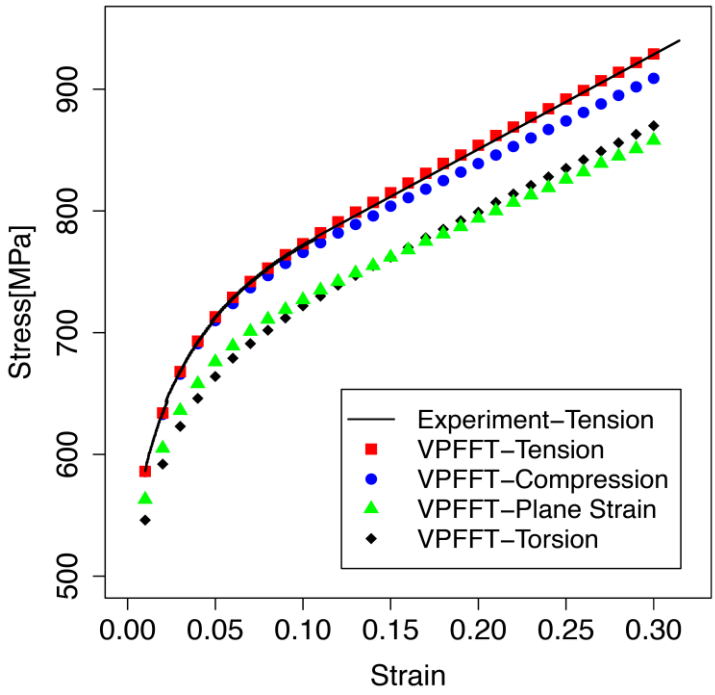

Figure 2.3 Experiment and simulated stress-strain curves of the Ferrite steel. Experimental tensile test curve (solid line), and VPFFT simulated stress-strain curves of four different macroscopic strain paths listed in Table 2.1.

According to Figure 2.3, the tension and compression stress-strain curves are close, denoting dismal asymmetry. However, the torsion and plane strain compression curves lie distinctly below the tension result. Tomé et al. [142] also showed similar behavior for a copper material with random texture. These authors argued that the material leaves off isotropy at large deformation, while the Voce law hardening equation is not truly equivalent for all strain paths.

2.5.2 Local strain and stress distribution

Figure 2.4 shows the strain rate on the exterior surface of the simulation domain for all four-deformation paths. It is obvious that the local response varies within grains. Each deformation path gives rise to different patterns of local maxima and minima in the microstructure. Figure 2.4 also reveals that under torsion the regions with the highest values of strain rate correspond to the grain center, while in the other deformation paths most of the hot spots lie near grain boundaries. We return to this point later.

Local strain rate peaks are known to occur near grain boundaries because of deformation incompatibilities between neighboring grains with different orientations, which experience different resolved shear stresses. Furthermore, rotation of crystal lattice depends on deformation paths, For example, when a single crystal is subjected to uniaxial tension or compression, loading axis rotates toward plane normal or slip direction, respectively [143]. Under torsion, however, the corresponding simple shear does not substantially affect the contacted area along the slip plan so less incompatibility phenomena are expected.

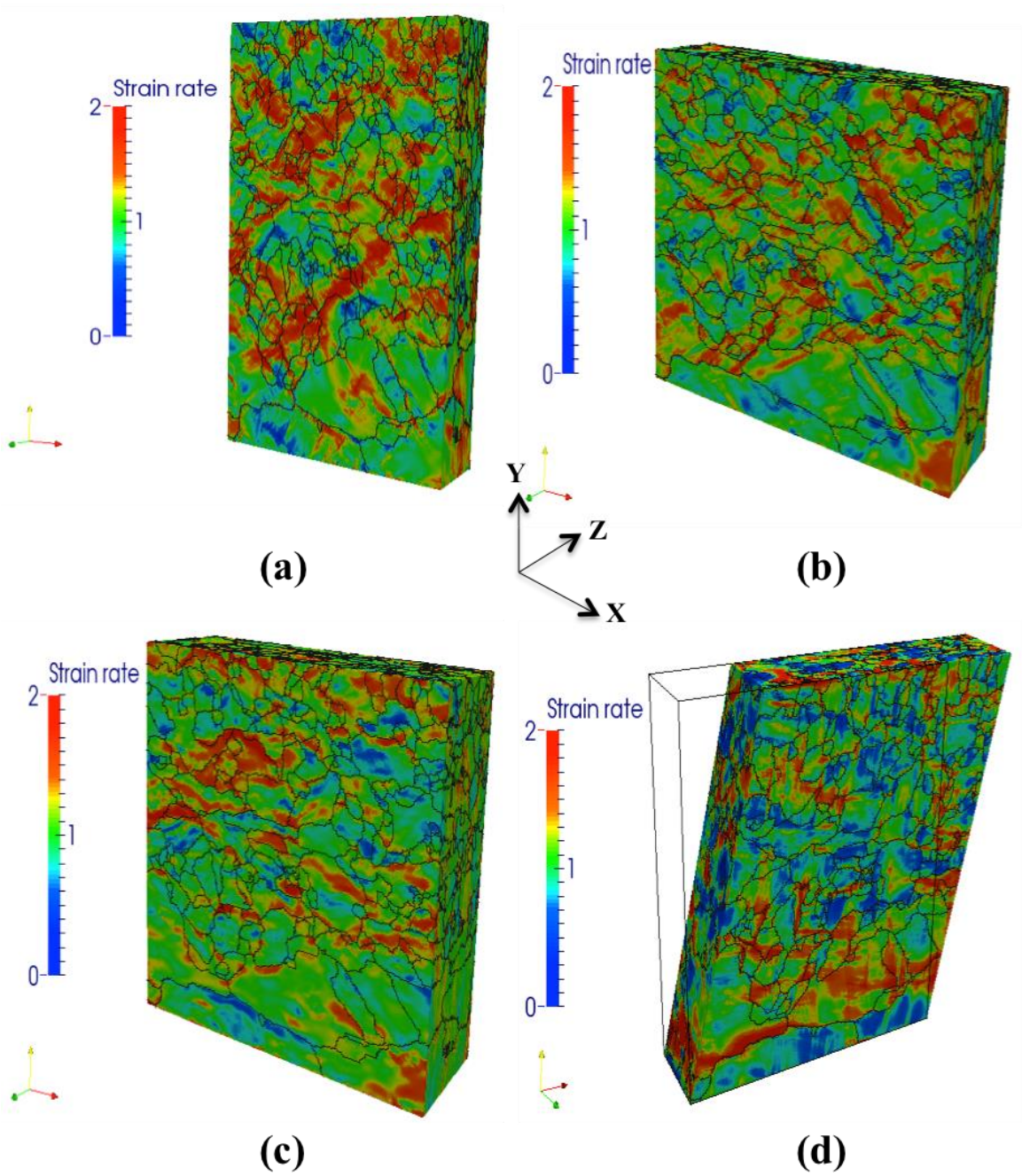

Figure 2.4 Distribution of local strain rate on surface of simulation box

Strain (von Mises equivalent) field on the surface of the simulation volume for ferritic steel after applying a) Tension, b) Compression, c) Plane strain, and d) Torsion boundary conditions.

Figure 2.5a shows a histogram of strain rate distribution for all four-deformation paths in the entire microstructure. The deformation modes do not appear to have a significant effect on the mean and peak fraction of histograms. However, all four histograms have long tails, indicating occurrence of shear localization [144].

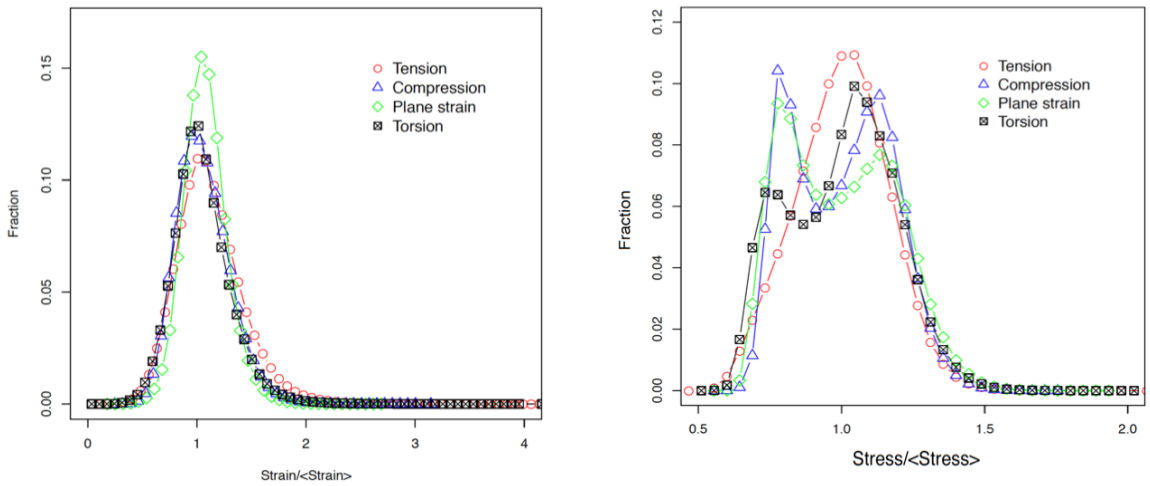

Figure 2.5 Stress and strain rate histogram

a) histogram of von Mises strain and b) histogram of von Mises stress, normalized by their respective mean values, in the simulation volume for 4 deformation modes (Tension, Compression, Plane strain, and Torsion).

Figure 2.6 shows the simulated stress distribution on the exterior surface of the simulated volume. Torsion and tension cause the highest local stress values among the four deformation modes. However, again in tension, stresses concentrate most adjacent to grain boundaries (red color) and spread toward grain interiors, while torsion shows the opposite effect. The dependence of stress distribution (both high and low stress values) to grain orientation changes with the nature of loading, and it is clear that hot spot regions are sensitive to the strain path.

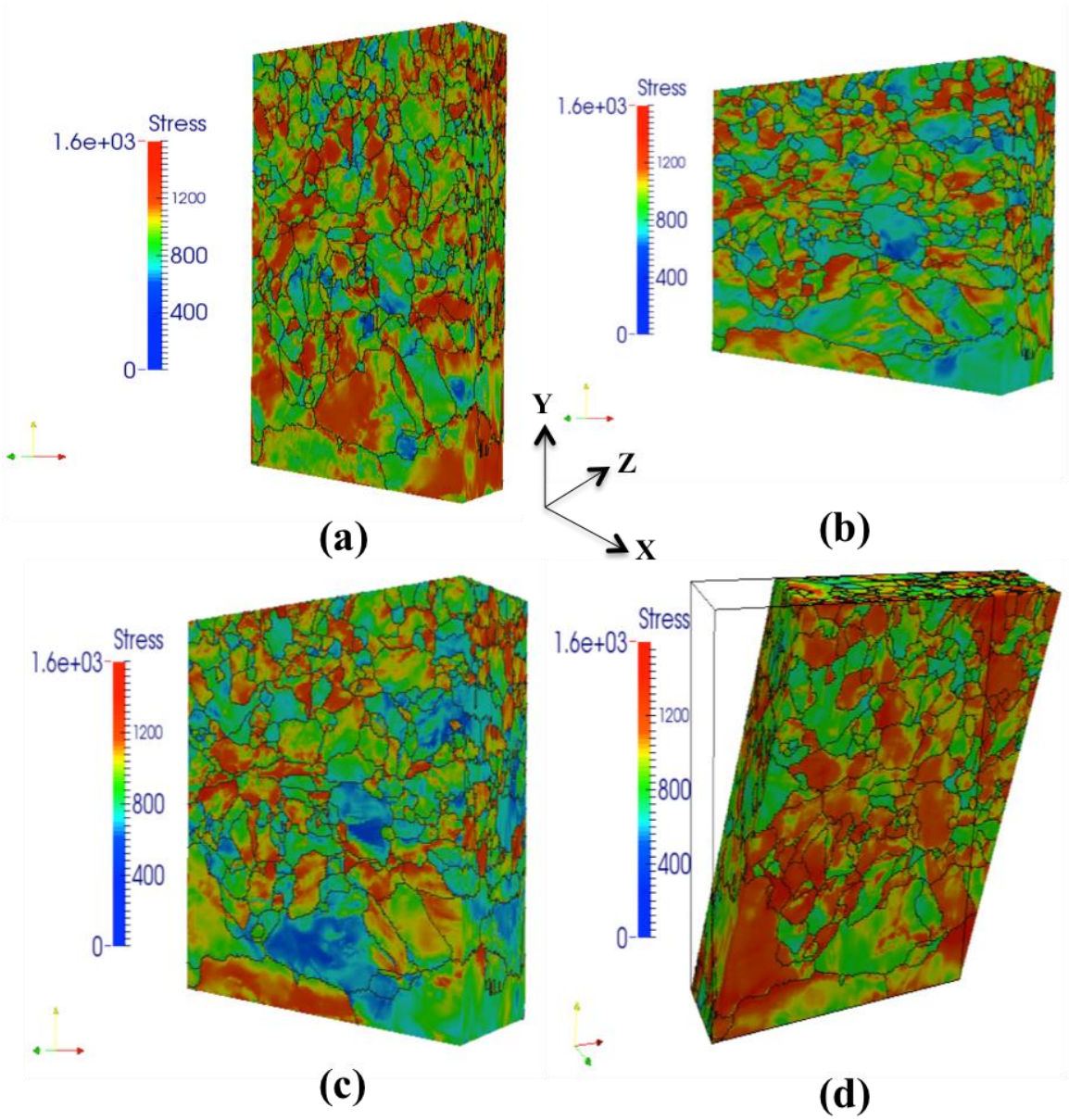

Figure 2.6 Distribution of local stress on the surface of simulation box

Stress (von Mises equivalent) field on the surface of the simulation volume for ferritic steel after applying a) Tension, b) Compression, c) Plane strain, and d) Torsion boundary conditions

The effect of microstructural inhomogeneities on stress localization was reported earlier by Barbe et al. [145]. The regions with high stress correlate with regions with high

dislocation densities. In general, localization amplitude scales with the degree of incompatibility, so peaks are expected near triple junctions and quadruple points.

Figure 2.5b compares stress distribution in all Fourier points between all strain path conditions. The strain path clearly affects the shape of local stress distribution. Except for tension, the stress histograms exhibit two peaks at the same stress value for all strain paths. The peak amplitudes reflect the quantity of grid-points with low or high local stresses, which are near GBs or grain centers, respectively.

2.5.3 Grain Scale behavior

As stated earlier, microstructural features such as grain boundaries (GB), triple junctions (TJ) and quadruple points (QP), are known to be an important source of strain localization. To investigate the relation between local strain rate, stress, and misorientation versus distance to these singularities, a Euclidean distance map [146]-was computed where each point was binned according to its characteristic distance (See Figure 2.7). For more detail on the procedure, the reader is referred to-Rollett et al. [136].

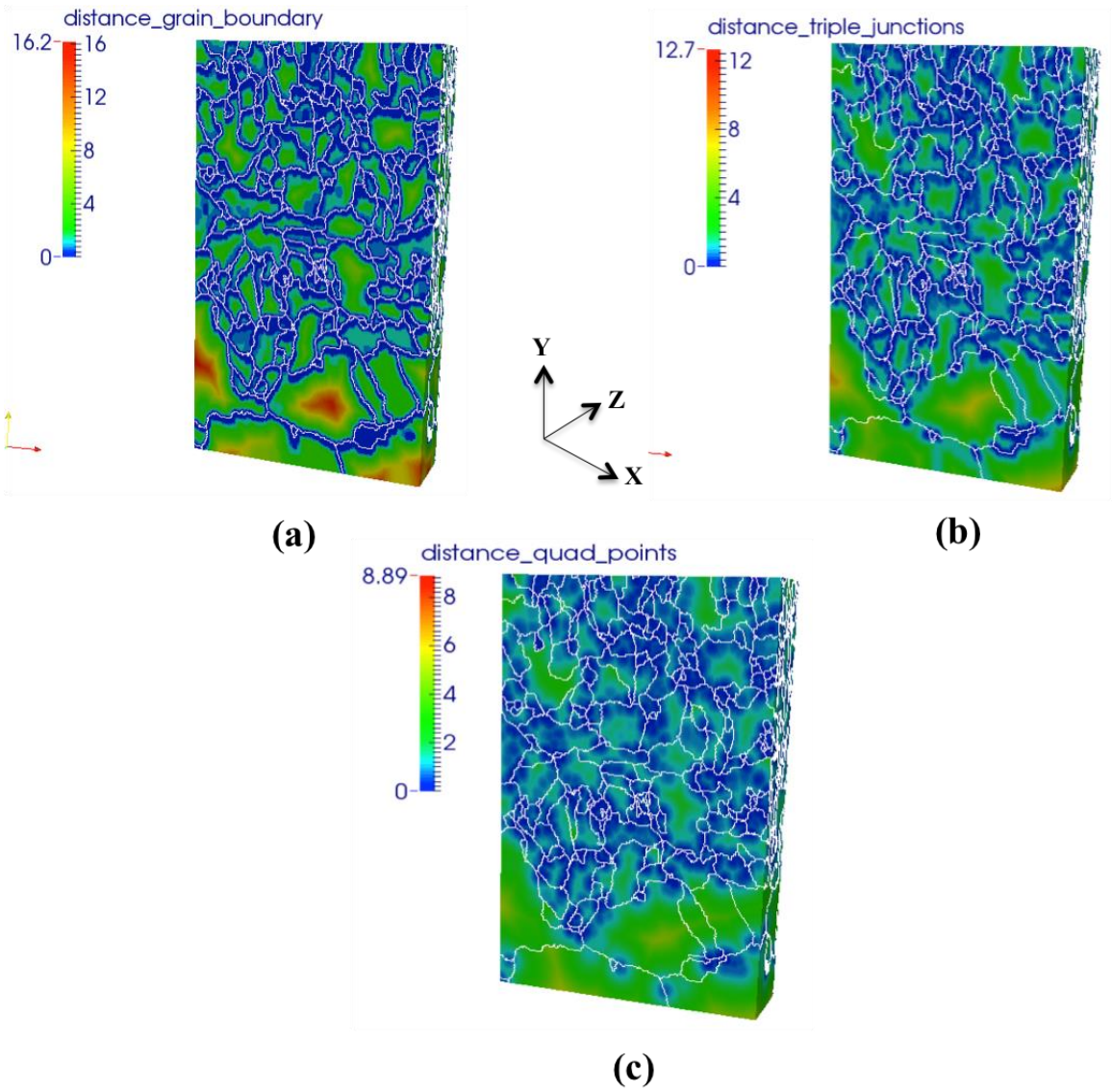

Figure 2.7 Distance map of each points to microstructural features

Distance map (units of voxels) for the input ferritic microstructure for a) the distance to the nearest grain boundaries, b) the distance to the nearest triple junction and c) the distance to the nearest quadruple point.

2.5.3.1 Grain scale Stress and strain-rate localization

Figure 2.8 exhibits variation of distance vs. local strain-rate of the points to GB, TJ, and QP. The general tendency in all three curves for each strain path is rather similar, and points near TJ and QP experience greater local strain rate. Both high and low values of strain-rate are found near microstructural features, and the maximum values of strain-rate close to the microstructural features depend on the strain path. Two-dimensional DIC experimental results also confirm existence of high and low strain regions close to grain boundaries [124]. Figure 2.8 shows that the maximum distances are found for local strain-rates close to 1, i.e. most likely in the grain center. In high strain-rate regions near grain boundaries, there is an inflection for all deformation modes except torsion, and the strain-rate of inflection point depends on the deformation path.

According to experimental observation, a grain can be divided into two regions, mantle referring to regions near grain boundaries, and the center of grain called core, and Each grain has several mantle zones according to neighboring grain numbers [147]. Therefore, the inflection point in the curves in Figure 2.8 can be considered as a boundary between mantle and core regions. Tension has the biggest inflection strain-rate (i.e. ~2) and compression has the smallest one (i.e. ~1.5). The points with local strain-rate larger than inflection strain-rate belong to mantle zone; otherwise the points belong to core.

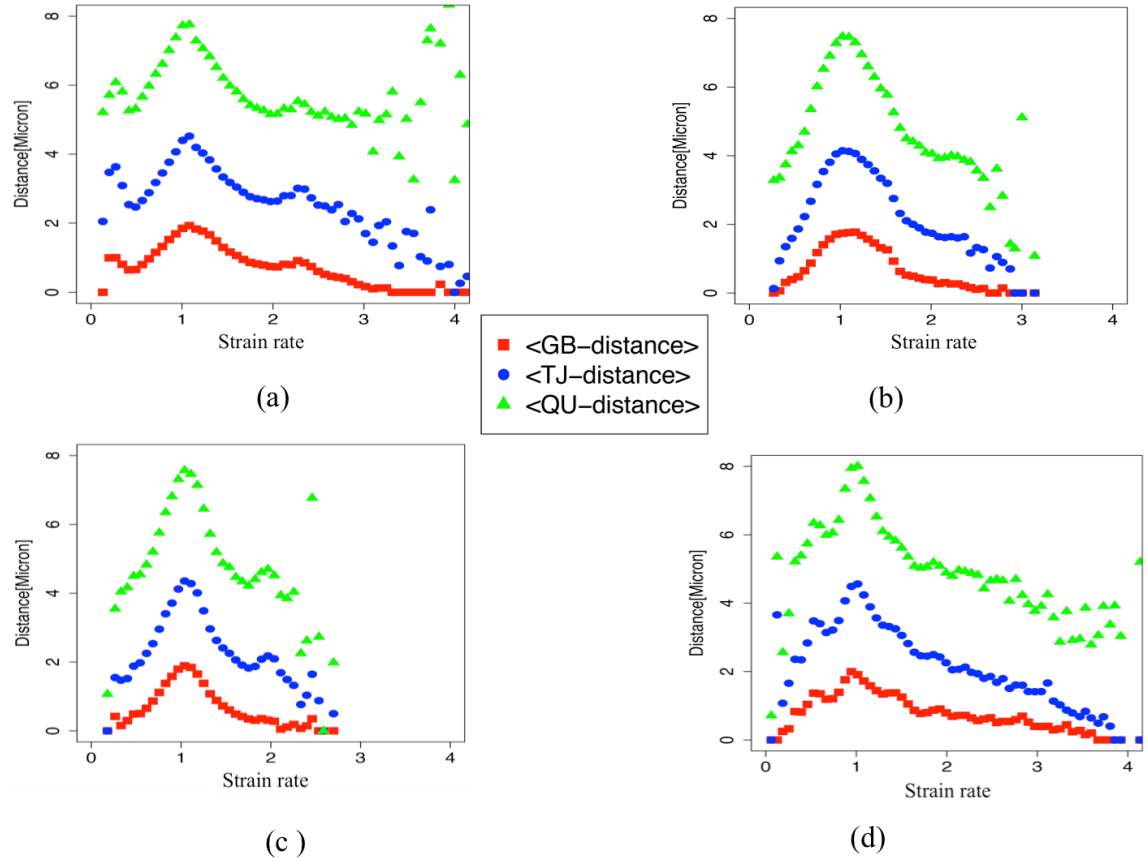

Figure 2.8 Plot of average distances binned by local strain rate

Plot of average distance to microstructural features in each strain-rate class after applying a) tension, b) compression, c) plane strain and d) torsion deformation, as described in Table 2.1.

To estimate the distance of the boundary between mantle and core zone from GBs, the local strain-rate was binned based on the closest distance from GBs in three-dimensions. Figure 2.9 shows variation of average strain-rate vs. the closest distance to grain boundary after applying four deformation paths. We observe that the local average strain-rate decreases with increasing distance from nearest GBs. There is an inflection point in the tension and plane strain curves, which is in agreement with results of two-dimensional DIC strain measurement [124]. In addition, the distance of the inflection point from GBs depends on the deformation path. Tension and plane strain cause the

shortest and longest mantle zone, respectively, while torsion produces a very smooth transition to the core zone. Surprisingly, under compression, local average strain-rate and distance to grain boundary does not show any meaningful correlations. In the other words, the existence of inflection point in tension, compression and plane strain reveals localized strain regions mostly concentrated near microstructural features, while in torsion they are more diffuse.

Figure 2.10 shows the relation between local stress and distance to GB, TJ, and QP in grain scale for all the four deformation modes. The general trend of curves is alike for all strain paths. In particular, the maximum stress values localize preferentially near microstructural inhomogeneities, and the points with low stress values lie close to GB, TJ and QP. Other experiments [148] and simulations [147] results are in agreement with our finding, which stresses localize more substantially in the vicinity of grain boundaries than in grain interiors.

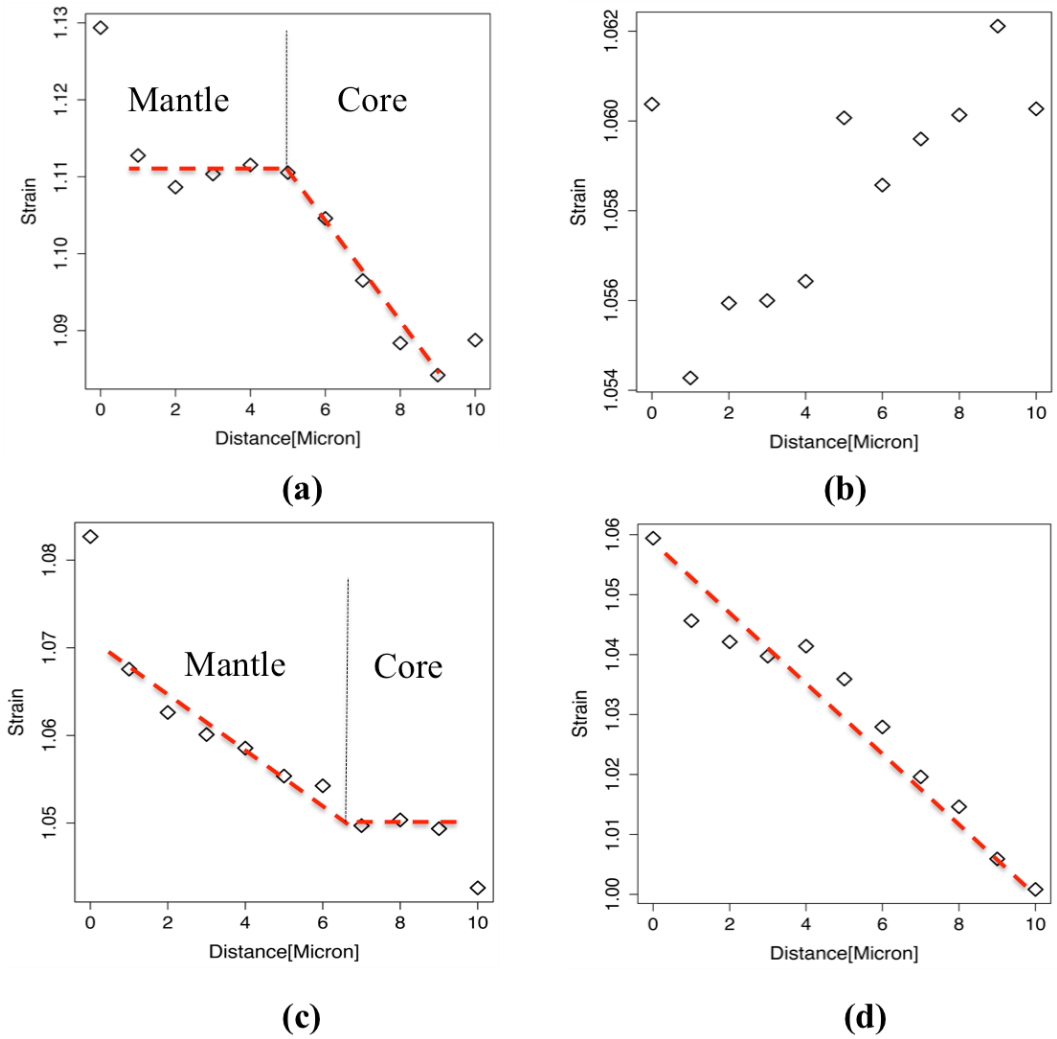

Figure 2.9 Plot of local strain binned by distance to microstructural features

Plot of average strain vs. distance to grain boundaries after applying a) Tension, b) Compression, c) Plane strain and d) Torsion boundary condition as described in Table 2.1.

The maximum values of local stress near grain boundaries depend on the deformation mode; that is, tension and compression cause the largest and smallest maximum local stress near grain boundaries, respectively. Moreover, the value of local stress in the grain center regions where have the maximum distance to grain boundaries

strongly is a function of the strain path. For instance, tension and plane strain induces the maximum and minimum local stress in the grain center regions, respectively

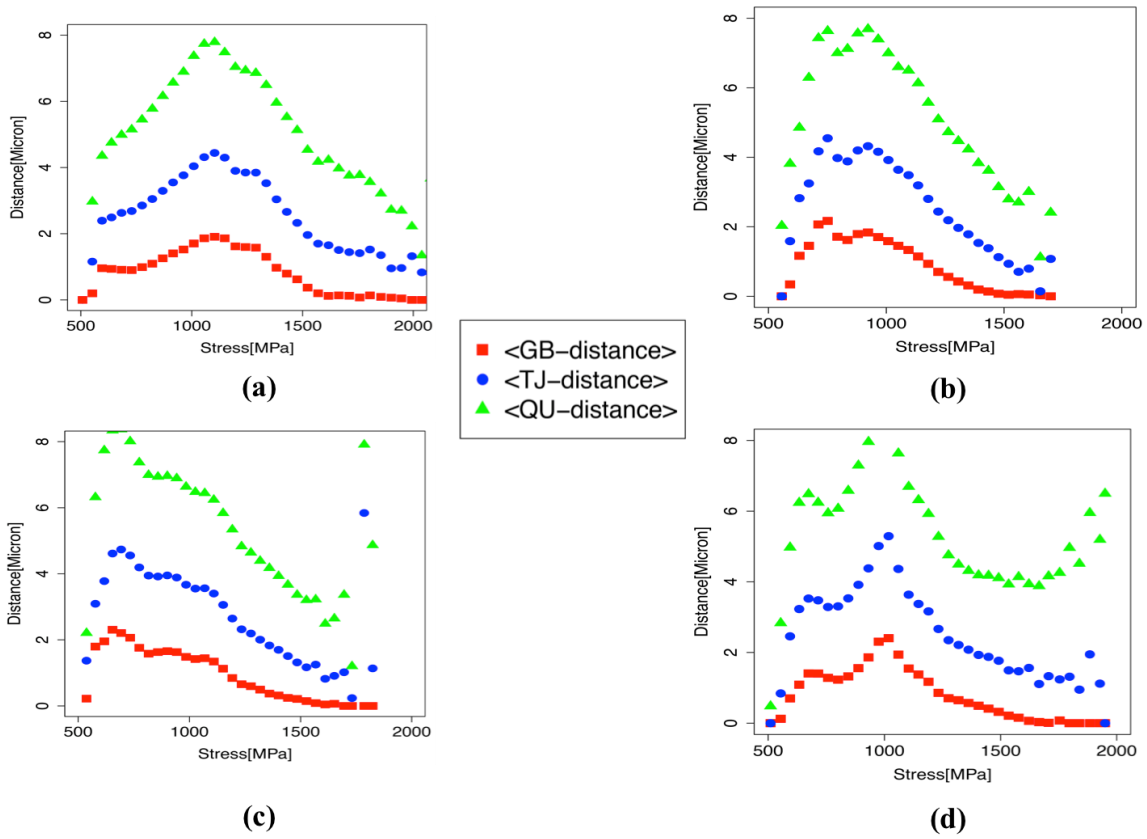

Figure 2.10 Plot of distance based on local stress in each point

plot of average distance to microstructural features in each stress class after applying a) Tension, b) Compression, c) Plane strain and d) Torsion boundary conditions as described in Table 2.1. Of the four strain paths, the plane strain case shows the most obvious anti-correlation between stress and distance, i.e. low stresses are found close to microstructural features.

2.5.4 Micromechanical Taylor Factor Analysis

To investigate the local relation between orientation and stress/strain-rate, we computed local Taylor factor in each Fourier point, which was referred to by micromechanical Taylor factor in other studies [149]. To calculate the local Taylor Factor, the summation of plastic strain over all active slip system was divided by local von Mises strain (equation 3-a).

$$M = \frac{\sum_{\alpha} |\dot{\gamma}^{\alpha}|}{\varepsilon_{eff}} \quad (2.5)$$

$$\varepsilon_{eff} = \sqrt[2]{\frac{2}{3}\varepsilon_{ij}}\varepsilon_{ij} \quad (2.6)$$

Figure 2.11 shows local Taylor factor was binned by the distance of the points to the microstructural Features (GB, TJ, and QP). The curves reveal an effect of the loading condition on the distribution of Taylor factor. Furthermore, regions with low and high Taylor factor values lie in the vicinity of microstructural features. The curves reveal that local Taylor factor values of the voxels near TJ and QP are greater than those for voxels near GB. This entails voxels near TJ and QP require stresses closer to stress vertices, and thus probably higher local stresses because of more pronounced hardening. Similarly, Harren and Asaro [150] showed that strain localization is more severe nearby TJs than elsewhere along GBs.

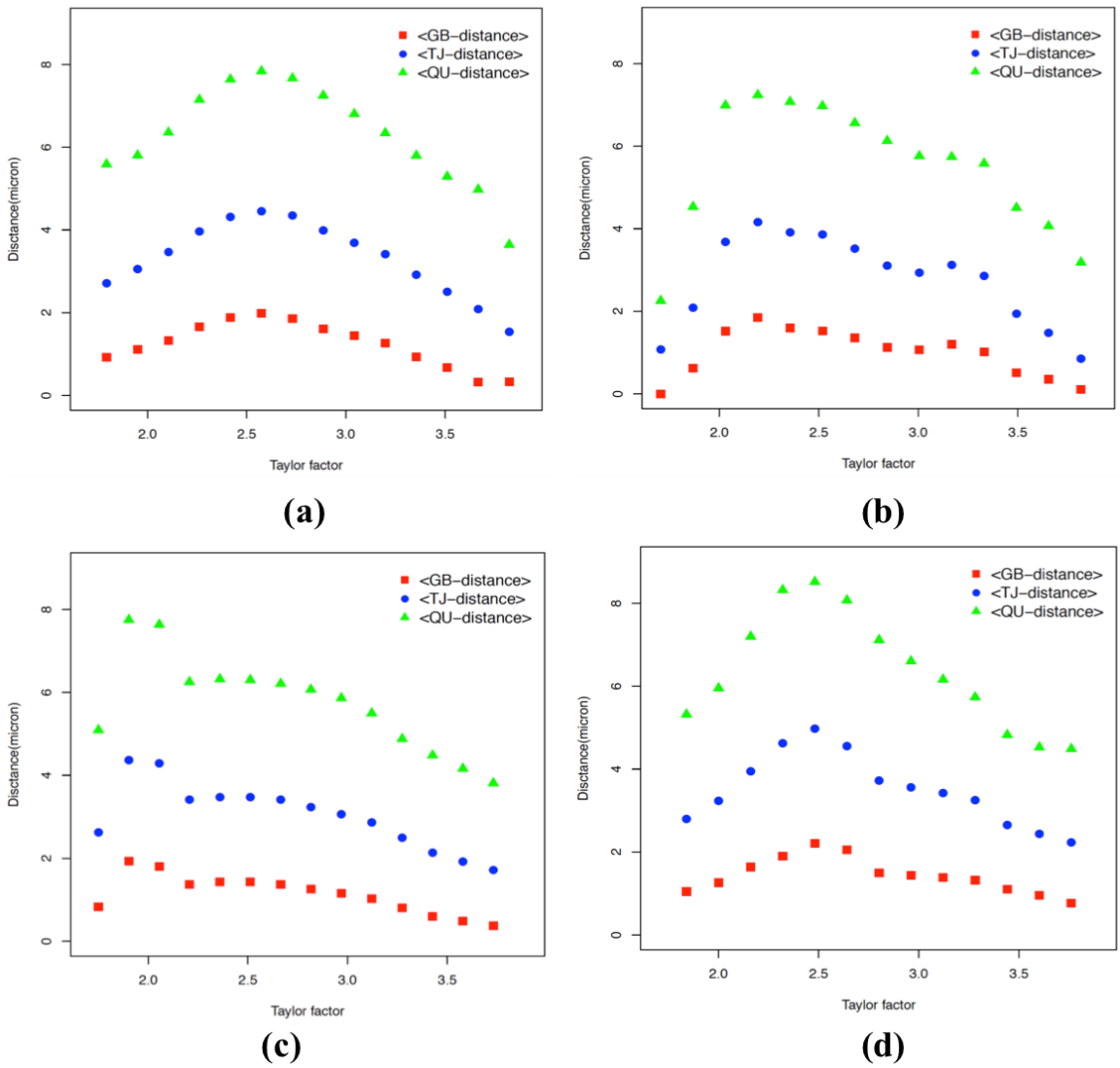

Figure 2.11 Plot of distance binned by local Taylor factor

Plot of average distance to microstructural features in each Taylor Factor class after applying a) Tension, b) Compression, c) Plane strain and d) Torsion boundary conditions as described in Table 2.1. The variations are similar to those observed for stress.

To quantify the relation between orientation and stress/strain-rate in each Fourier point, the variations of Taylor factor with local strain-rate/stress were calculated. Figure 2.12b shows that the local Taylor factor is anti-correlated with the local strain-rate. The Taylor factor was binned by local strain-rate in each boundary condition. In all

deformation modes, there is a negative correlation between Taylor factor and local strain-rate, decreasing strain-rate with increasing Taylor factor. Moreover, the deformation mode does not have significant effect on the correlation between local strain rate and local Taylor factor. The anti-correlation of Taylor factor with local strain rate polycrystal model was also reported for a FCC metal subjected to tension [76,151]. This behavior is consistent with the view of Taylor factor as determining the tendency of a local orientation to be favorable for plastic deformation. It means the points with low Taylor factor will experience more strain compared to points with high Taylor factor values, in the average.

Figure 2.12a shows the correlation plots between the local Taylor factor and local stress. The Taylor factor was binned by local stress in each deformation mode. For all deformation modes, there are strong positive correlations showing increasing Taylor factor with increasing stress. The correlation plots can be divided into two regions. In the first region, local stresses are less than 1000 MPa, for which all correlation plots have essentially the same values. In the second region, where stresses are higher than 1000 MPa , some divergence is evident with respect to deformation path. For the same stress value in the second region, tension and plane strain bring about the smallest and highest Taylor factor values, respectively. This entails that with changing stress state from uniaxial to multiaxial in a same equivalent von Mises stress, strain incompatibility increases in high local stress regions, which are near the microstructural features.

Local strain variations caused by Taylor factor mismatch across grain boundaries can be the source of intergranular crack formation [152,153]. In reality, strain gradients could be mitigated by transmission of slip across the grain boundary [42], but this

interfacial reaction phenomenon is not captured in our crystal plasticity framework. High Taylor factor points near grain boundaries in figure 2.11 are referred to regions with low local strain or low amount of slip shear, and can be damage or crack nucleation sites.

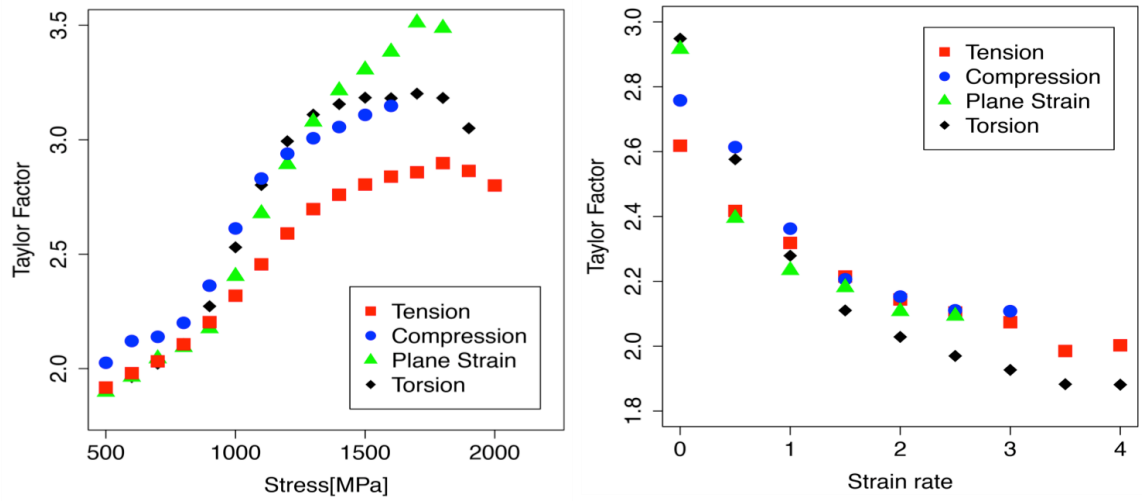

(a) **(b)**

Figure 2.12 Correlation between local Taylor factor and local stress/strain-rate

Correlation plot between Taylor factor and a) local strain rate, b) local stress for Tension, Compression, Plane strain, and Torsion boundary conditions as described in Table 2.1. The Taylor factor is positively correlated with stress and anti-correlated with local strain rate.

2.5.5 Orientation and Stress gradient

Kernel average misorientation (KAM) is a reliable criterion for calculating the local orientation changes and the deformation degree in each point. Several studies have been performed to measure the localized misorientation with the help of kernel average misorientation in 2D with Electron Backscatter Diffraction (EBSD). A review of the technique was reported in a review paper by Wright et al. [154].

In this work, KAM was determined in 3D for each grid-point within a given grain as an average over all 26 nearest neighbors in the simple cubic grid. However, neighbors with misorientation exceeding 10° in lattice misorientation were excluded from the averaging procedure in order to avoid including neighbor points from a different grain.

Figure 2.13 shows local average misorientation map on the surface of simulation volume. The map key goes from blue to red for low to high local average misorientation values. From a qualitative point of view, it is clear that the orientation change does not happen uniformly at grain scale on the surface of unit cell, and there is an orientation gradient inside of the grain. To obtain a quantitative analysis of orientation gradient in the grain scale, the values of local KAM binned according to the distance of the points to the microstructural Features (GB, TJ, QP) are given in Figure 2.14.

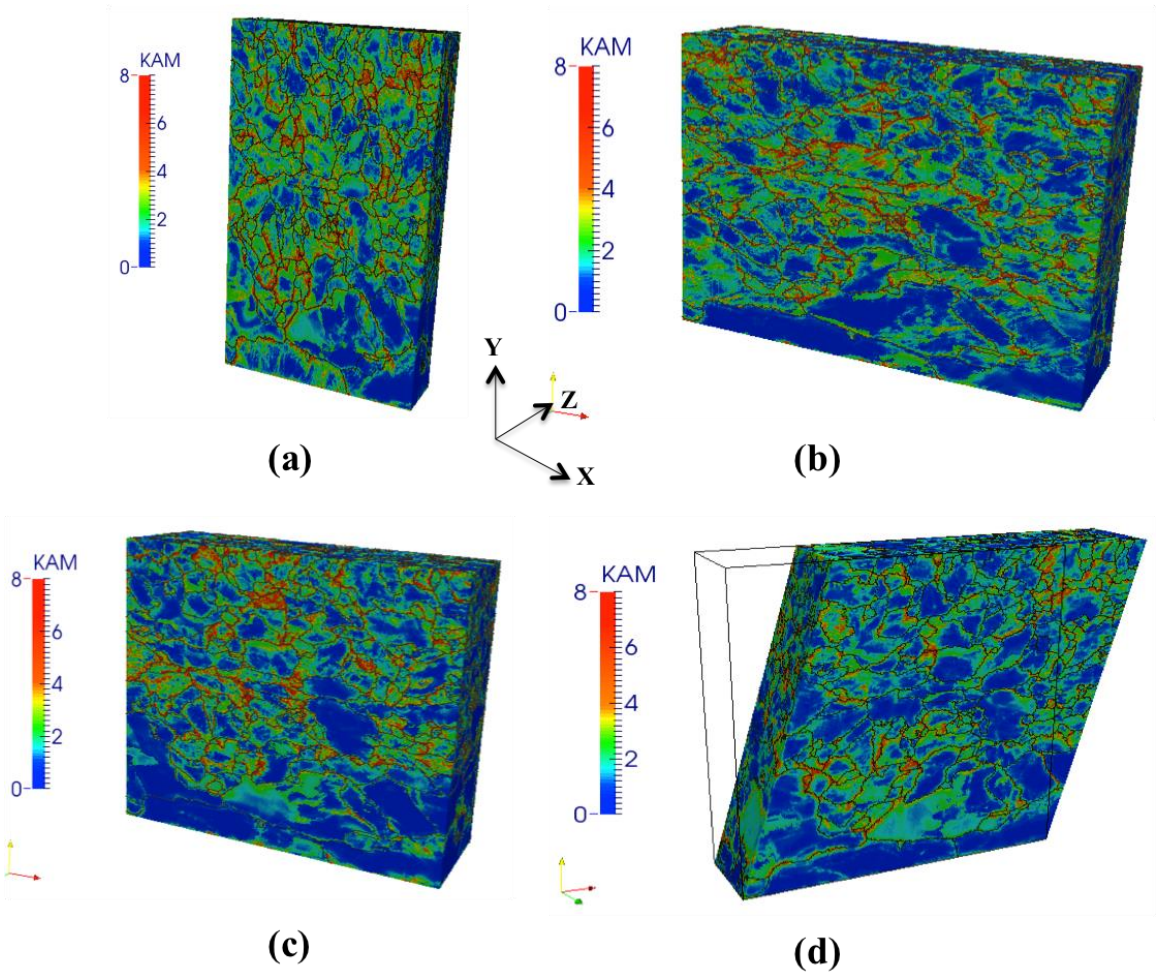

Figure 2.13 Distribution of local average misorientation on simulation box

Kernel Average misorientation on the surface of simulation volume after applying a) Tension, b) Compression, c) Plane strain and d) Torsion boundary conditions as described in Table 2.1.

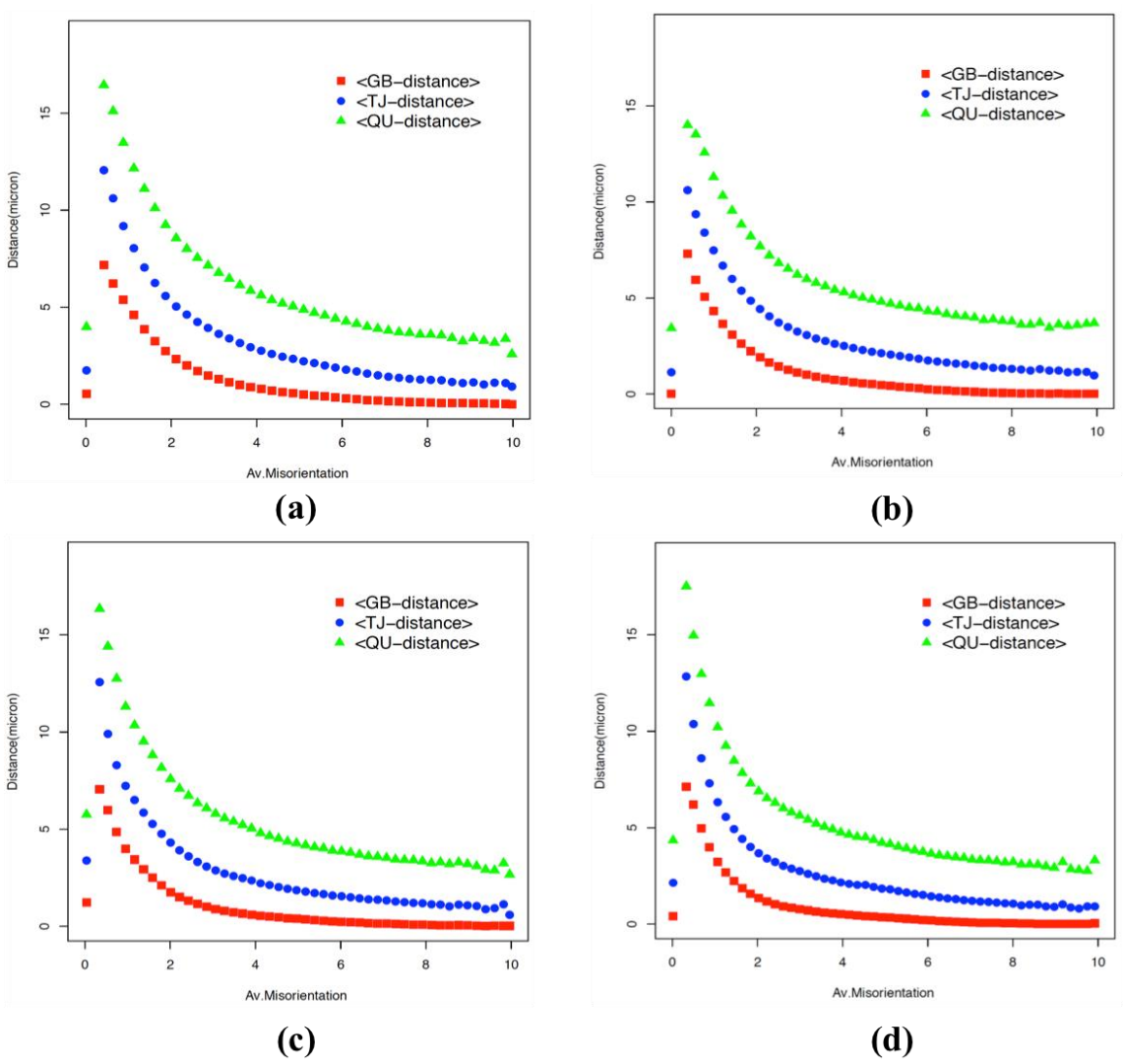

Figure 2.14 Plot of distance binned by local average misorientation in each point plot of average distance to microstructural features in each kernel average misorientation class after applying a) Tension, b) Compression, c) Plane strain and d) Torsion boundary conditions as described in Table 2.1.

The general trend is that KAM varies with distance to grain inhomogeneities in a similar fashion for four types of the investigated deformation paths, and high KAM points lie near the microstructural features. Moreover, The corresponding curves for QP and TJ are over that of GBs, which means that for the same KAM, the width of localized

misorientation regions near TJs and QPs is higher than that of regions near GBs. In the other words, triple junctions and quadruple points are more preferential sites for localized misorientation. This is consistent with the observation made in the other studies on dislocation densities, which were found to concentrate in the vicinity of TJ sand QPs [155]. In 2D measurements, micro-hardness and Hough based EBSD line scans revealed that triple junctions can act as preferential sites for GND accumulation which caused an increase in KAM [157,158].

To find the relation between orientation gradients and stress gradients, the first spatial derivative for each stress component was calculated. Figure 2.15 shows the (scalar) von Mises equivalent stress gradient in each Fourier point. Comparing local average misorientation and stress gradient map (Figure 2.13 and 2.15) reveals similarities in the features; high and low values lie close to microstructural features and in center of grains, respectively. Rollett et al. [159] reported alike stress gradient map for tension. They suggested that stress gradient near grain boundaries ties with changes of Taylor factor and stress state form one grain to another.

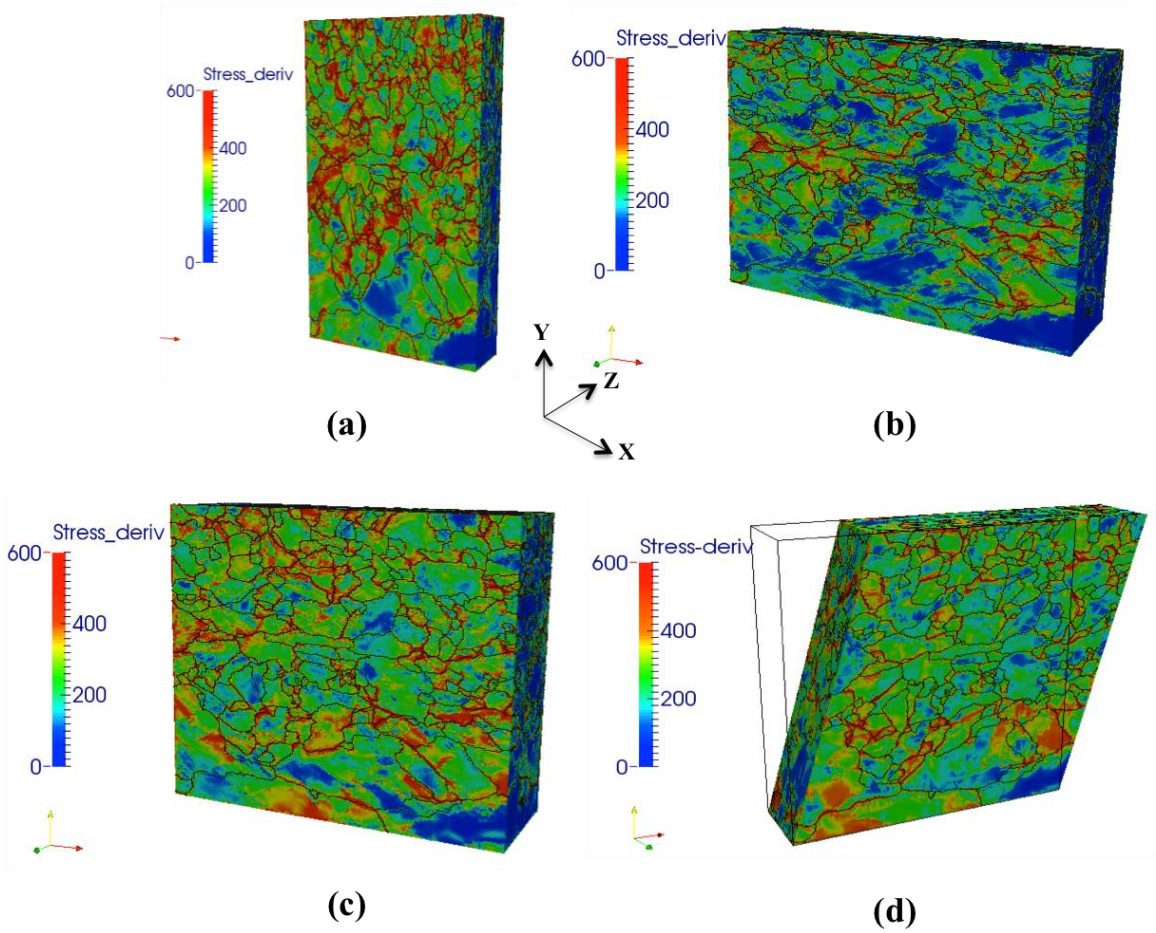

Figure 2.15 Distribution of local stress gradient on the surface of simulation box

Stress gradient (von Mises equivalent) on the surface of the simulation volume after applying a) Tension, b) Compression, c) Plane strain and d) Torsion boundary conditions as described in Table 1.

In order to quantify the similarities between orientation and stress gradient maps, correlation between local average misorientation and stress gradient was plotted in Figure 2.16. These plots are KAM binned by stress gradient in each strain path. Tension and compression show a strong positive correlation with stress gradients for the extreme range explored, while the strong positive correlation is more limited for plane strain compression and torsion. Similar observations were reported by Raabe et al. [160], who analyzed a deformed BCC bicrystal under plane strain. Having obtained a homogenous

deformation with no orientation gradients, these authors suggested both grains have small Taylor factor under plane strain condition, as one grain delivers external constraint and shearing into its neighbor. Moreover, both grains experienced nearly similar reduction or plastic strain, and had the same kinetic hardening.

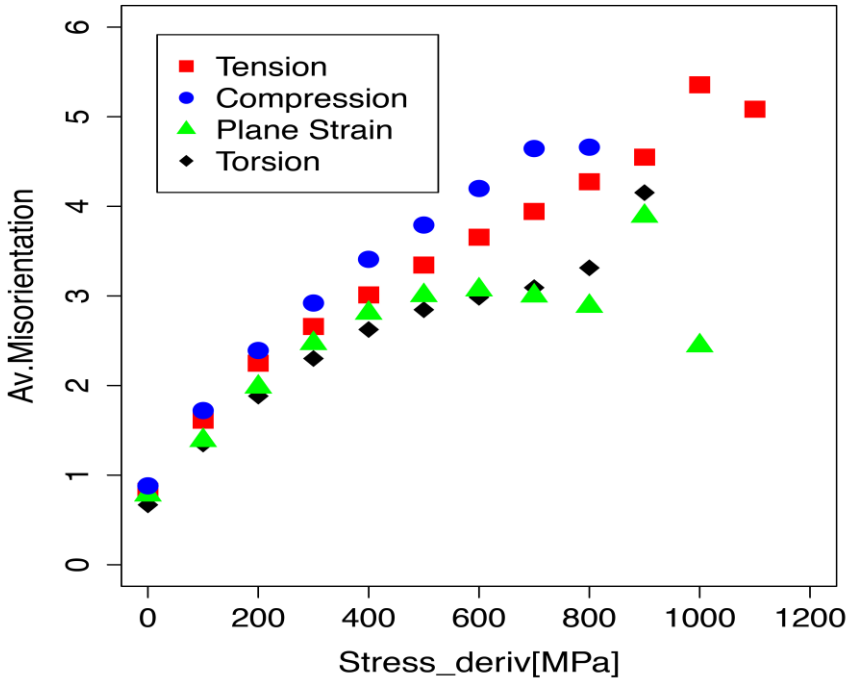

Figure 2.16 Correlation between Average misorientation and Stress derivation

Correlation plot between Kernel Average misorientation (KAM) and Stress gradient after applying a) Tension, b) Compression, c) Plane strain and d) Torsion boundary conditions as described in Table 1.

2.6 Conclusions

Using the viscoplastic fast Fourier transformation (VPFFT) model, we studied the effect of stress state on the three-dimensional distribution of local stress, strain, KAM, and Taylor factor in a ferritic steel microstructure obtained by focused ion beam-electron backscattered diffraction. The results of the simulations of deformation under tension, plane strain, and torsion suggest the following conclusions:

1. The presence of microstructural features affects the stress and strain localization with high and low values of stress and strain localizing near TJ and QP rather than near GBs.
2. The local strain-rate values at the grain scale show a distinction between core and mantle regions in grains. The width of the mantle region (next to grain boundaries) varies with stress state boundary conditions.
3. For all deformation modes, KAM values tend to peak close to grain boundaries.
4. For all deformation modes, the average KAM value increases nearly linearly with strain at a rate that varies as tension > compression > plane strain > torsion.
5. Local Taylor factor correlates strongly with local stress and inversely with strain-rate. These correlations are relatively insensitive to the deformation mode.
6. KAM correlates strongly with stress gradient for tension and compression, whereas this correlation is slightly weaker for plane strain and torsion

CHAPTER III

THE EFFECT OF DEFORMATION TWINNING ON STRESS LOCALIZATION IN A THREE DIMENSIONAL TWIP STEEL MICROSTRUCTURE

Previously published in Modelling Simul. Mater. Sci. Eng. **23** 045010)

doi:10.1088/0965-0393/23/4/045010

3.1 Abstract

We present an investigation of the effect of deformation twinning on the visco-plastic response and stress localization in a low stacking fault energy twinning-induced plasticity (TWIP) steel under uniaxial tension loading. The three-dimensional full field response was simulated using the fast Fourier transform method. The initial microstructure was obtained from a three-dimensional serial section using electron backscatter diffraction. Twin volume fraction evolution upon strain was measured so the hardening parameters of the simple Voce model could be identified to fit both the stress-strain behavior and twinning activity. General trends of texture evolution were acceptably predicted including the typical sharpening and balance between the <111> fiber and the <100> fiber. Twinning was found to nucleate preferentially at grain boundaries although the predominant twin reorientation scheme did not allow spatial propagation to be captured. Hot spots in stress correlated with the boundaries of twinned voxel domains,

which either impeded or enhanced twinning based on which deformation modes were active locally.

3.2 Introduction

Twinning-induced plasticity (TWIP) steels have high strength and ductility, and are finding use in demanding applications in the automotive industry. The high manganese (Mn) content in TWIP steel (typically ~ 20\%) reduces stacking fault energy and increases the formation of mechanical twins [161]. Several investigations have been performed to study the effect of various factors such as grain size [162], chemical composition [163] and grain orientation [164] on the formation of mechanical twinning.

During plastic deformation, the orientation of material deformed by dislocation slip changes modestly, whereas material undergoing deformation by twinning causes a large discrete change in orientation, such as the ~ 60 degree for the {111}<11-2} twin [165]. These orientation changes cause homogeneous and localized deformation regions, respectively. Several computational twinning models have been developed for efficient capture of the crystallographic reorientation caused by deformation twinning in polycrystals [166,167].

The predominant twin reorientation (PTR) scheme [167] was implemented in the visco-plastic self-consistent (VPSC) polycrystal simulation code to predict twin volume fraction and grain reorientation due to deformation twinning. In previous research efforts, the VPSC code was used to predict texture evolution in HCP [168] and FCC [169] metals undergoing deformation twinning during plastic deformation. The VPSC method is a ``mean-field" approach, which is based on an Eshelby-like interaction of each grain with a homogenized medium. The mean-field approach allows the strain (increment) in each

grain to deviate from the average while determining the response of each grain. The grain based approach means that there is no information on the local stress and strain in specific regions such as the interior of a grain or near boundaries.

Because of this limitation, and to gain better insight into the spatial distribution of mechanical twinning, full-field calculations such as the crystal plasticity finite element method (CPFEM) have been used. CPFEM, based on a non-homogenization scheme, is a full-field solution of crystal plasticity [170]. Some researchers implemented a constitutive model to compute both texture and twin volume fraction [171]. Kalidindi [172,173] also proposed a model based on the total Lagrangian approach to predict twin volume faction and texture evolution. Several examples are available of the use of the PTR model in CPFEM to calculate the deformation twin volume fraction and stress distribution in hexagonal metals [174–176]. Use of the FE method requires a mesh; it is easy to generate a pixelated mesh, which leads to large numbers of degrees of freedom in the calculation. Less dense meshes that conform to the grain boundary network can also be generated but the process is complicated and time-consuming.

A full field solution based on visco-plastic fast Fourier transforms (vpFFT) was applied to find the local stress and strain rate inside of a grain or near to grain boundaries. The simulation domain for vpFFT is a three-dimensional image of the microstructure of interest. Originally, the full field solution for stress and strain rate using Fast Fourier transform (FFT) was developed to compute the elastic and inelastic, effective and local response of composites [177]. In further developments, Lebensohn [178] and his collaborators [179,180] used FFT to compute the full field solution of a visco-plastic polycrystalline aggregate. The vpFFT simulations on both synthetic and measured

microstructures showed that highly stressed regions (``hot~spots" [181]) tend to occur near microstructural features such as grain boundaries.

In this paper we propose an approach for the incorporation of twinning in an actual three dimensional TWIP steel microstructure with vpFFT. The actual three dimensional TWIP steel microstructure was obtained by three dimensional serial sectioning electron backscatter diffraction (EBSD). An approach that we introduce as ``three dimensional PTR" is used in this work, and is based on the predominant twin reorientation (PTR) scheme. This approach does not capture the shape or growth of a twinned region after nucleation, so the typical lamellar, or plate like, morphology of twins is not accounted for. However, the twin volume fraction is controlled based upon considering an admissible accumulated shear of the predominant twin system (PTS). Thus, the approach should perform better for the case of random textures where deviations from the average strain rates play an important role in twin nucleation. We benchmark the results of twinning contribution to strain localization with the behavior of a three-dimensional (3D) microstructure of a classical high Mn-containing TWIP steel.

3.3 Method

3.3.1 3D Microstructure

A hot rolled Fe-0.6C-18Mn-1.5Al (wt \%) TWIP steel [164] was loaded under uniaxial tension along the transverse direction (TD) until about 0.4 total strain. Electron backscatter diffraction (EBSD) was performed on the pre-deformed state and after 0.4 strain in an effort to instantiate the numerical simulations by the final deformation texture and twin volume fraction. The sample preparation procedure and EBSD characterization were described by [164], and the reader is referred to this work for more details.

To generate a realistic 3D grain orientation microstructure for use by the FFT model, a rectangular specimen was extracted from the middle of the hot rolled plate perpendicular to TD. Then, two sides of the sample were mechanically ground to make parallel sides normal to TD, which were then subjected to the 3D EBSD serial sectioning technique explained in detail by [182]. The experimental data was then processed using the Dream.3D (Digital Representation Environment for Analyzing Microstructure) software package [183] to generate the 3D orientation map shown in Figure 3.1.

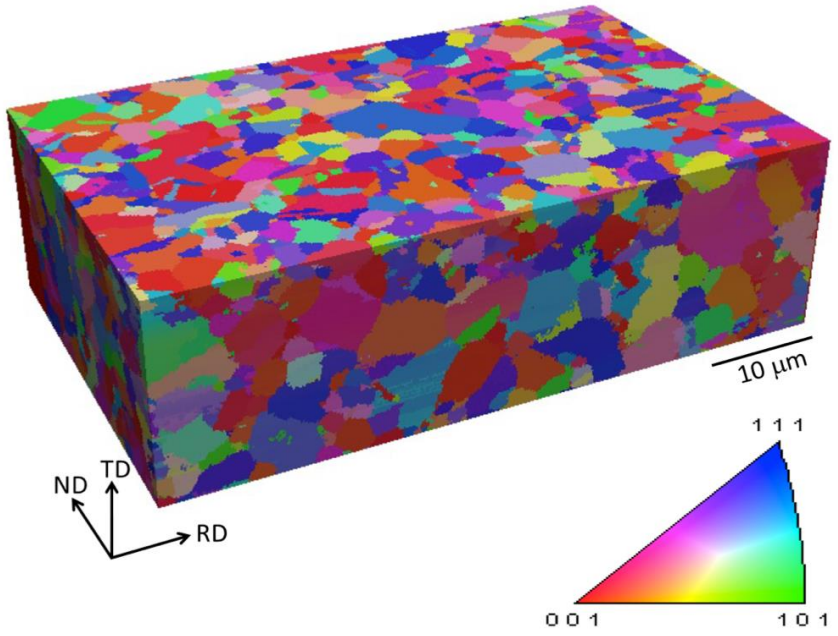

Figure 3.1 Three dimensional reconstructed microstructure of TWIP steel

Three-dimensional inverse pole figure (IPF) grain orientation map reconstructed by electron backscatter diffraction (EBSD). The colors in the IPF map correspond to the orientations in the transverse direction

Because of poor reconstruction at the edges, 50 voxels were removed at the edges in the x and y directions, and a subset with dimensions $128 \times 128 \times 100$ was extracted from the original 3D image, which had dimensions of $343 \times 267 \times 100$ in the x, y, and z

directions, respectively. Buffer layers (28) were added in the z dimension to make a cell with power-of-two dimensions. By inserting a buffer layer, a free surface is obtained on the top and bottom of the structure. In the Dream.3D clean-up procedure, any grains larger than 50 voxels were considered as a grain, and smaller regions were absorbed into their majority neighbor. This resulted in a total of 713 grains in the FFT input microstructure. The FFT input texture (Figure 3.2b) was close to the experimental one (Figure 3.2a) despite the small number of grains in the domain.

Since the simulation is periodic, but the actual microstructure is not, there is a concern about artifacts near the edges. However, in work by [181] this was shown to not be a concern.

3.3.2 FFT Method and hardening rule

The description of the FFT method for simulating the visco-plastic behavior of 3D polycrystalline materials has already been described in detail [178–180,184]. The key feature of the method is the use of a Green's function in the solution, which leads to a convolution integral that is replaced via the FFT with a local tensor product. We emphasize, however, that because the perturbation (polarization) field of the local strain at each grid-point is not a priori known, an iterative convergence criterion must be employed to compute a compatible strain rate field that fulfills the equilibrium condition. Since the latter is sensitive to the contrast in local properties [178,181], the augmented Lagrangian algorithm [180] was used wherein the compatible local strain rate field and the equilibrated stress field are simultaneously updated.

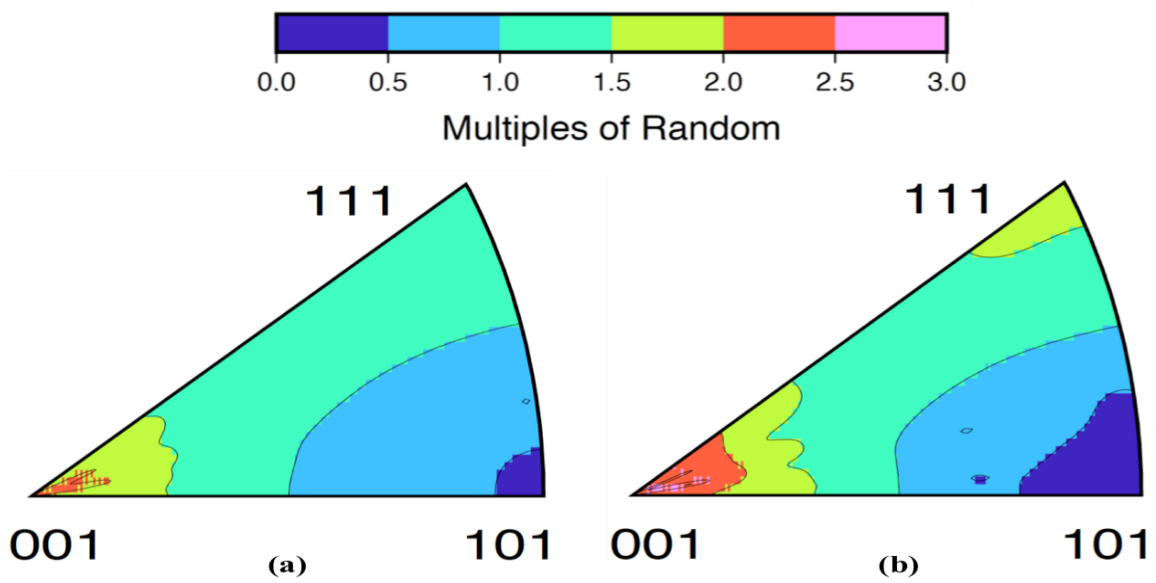

Figure 3.2 Inverse pole figure of 2D and 3D EBSD measurement

Inverse pole figure diagram of (a) measured texture with EBSD at strain 0%, and (b) FFT input microstructure via 3D serial sectioning EBSD technique with dimension 128 * 128 * 100.

The compatible strain-rate field still satisfies the following classical constitutive equation at every grid-point:

$$\dot{\mathcal{E}}^{s}{}_{ij}(x) = \sum_{s=1}^{N} m_{ij}^{s}(x) \left(\frac{m_{ij}^{s}(x):\dot{\sigma}(x)}{\tau^{s}(x)}\right)^{n} sgn\left(m_{ij}^{s}(x):\dot{\sigma}(x)\right) \qquad (3.1)$$

Here summation of $N = N_s + N_t$ terms includes all N_s slip and N_t twin systems, τ^s, m^s, and $\dot{\gamma}^s$ are the current critical resolved shear stress, Schmid tensor, and local shear rate associated with each deformation system, respectively; $\dot{\varepsilon}(x^d)$ and $\dot{\sigma}(x^d)$ are the strain-rate and deviatoric stress tensors at grid-point x; $\dot{\gamma}_0$ is a normalization factor which, in practice, is a constant value in relation to the normalized imposed macroscopic strain rate, and n is the rate-sensitivity exponent, which was set equal to 12.

The hardening rule used in the simulations is the extended phenomenological Voce model, as defined for the VPSC model [185]. The stress-strain data used was a single quasi-static test and therefore the Voce equation was a sufficient description. In this model, hardening is described by:

$$\tau_s(\Gamma) = \tau_0 + (\tau_1 + \Theta_1\Gamma)\left[1 - exp\left(\frac{-\Theta_0\Gamma}{\tau_1}\right)\right] \quad (3.2)$$

Where the evolution of the slip resistance for each slip system, s, is represented by phenomenological parameters reflecting a purely curve fitting approach: τ_0, τ_1, θ_0, and θ_1. The Γ term is the accumulated shear strain in each grid-point. Latent hardening can be included in this scheme but was not used here because of the lack of multi-axial test data.

3.4 Three dimensional PTR scheme

The three dimensional PTR scheme consists in following the accumulated shear strain of the most active twin system upon strain in each grid-point, x^d until it reaches a threshold twin volume fraction $F^{th,mode}$ for reorientation. The most active twin system is detected by following the accumulation of the shear strain $\gamma^{t,n}$ at each twin system t for a given increment n. Thus, a virtual volume fraction F at each grid-point can be calculated as:

$$F^{mode}(t, x^d) = \sum_1^n \Delta F^{mode}(t, x^d) = \sum_1^n \frac{\gamma^{t,n}}{S_0} \quad (3.3)$$

Where S_0 represents the characteristic shear of the twin mode. Whenever a grid-point satisfies $F^{mode}(p) = F^{th,mode}$ for a predominant twin system p, the subroutine

allows it to reorient that grid-point and updates the effective twin volume fraction, F^{eff}, which becomes:

$$F^{eff} = \frac{N_r}{N} \quad (3.4)$$

Where N_r and N are the total reoriented grid-points by twinning and total grid-points in the unit cell, respectively.

Naturally, the threshold will be a function of both F^{eff} and the sum of accumulated F^{mode} of all twin systems averaged over all grid-points:

$$F^{th} = c_1 + c_2 \frac{F^{eff}}{F^{acc}} \quad (3.5)$$

$$F^{acc} = \sum_{x^d} \sum_t F^{mode}(t, x^d) \quad (3.6)$$

where c_1 defines the incubation strain for the onset of twinning, and c_2 is a constant that will be tuned to the observed resistance to twin propagation.

Following [186], the reorientation of the grid-points is monitored in such a way that F^{eff} never exceedsF^{acc}. However, as mentioned already, this purely local approach does not capture the lamellar, or thin plate, growth often observed in mechanical twinning [165].This limitation is discussed in the interpretation of the simulation results.

3.5 Results and discussions

3.5.1 Overall behavior

Figure 3.3a compares the experimental and modeling results of the stress-strain behavior. The rate sensitive constitutive formulation of Equation (III-1) assumed all the 24 bi-directional close-packed {111}<-110> slip systems in addition to all 12 uni-directional {111}<11-2> twinning systems to accommodate the imposed strain.

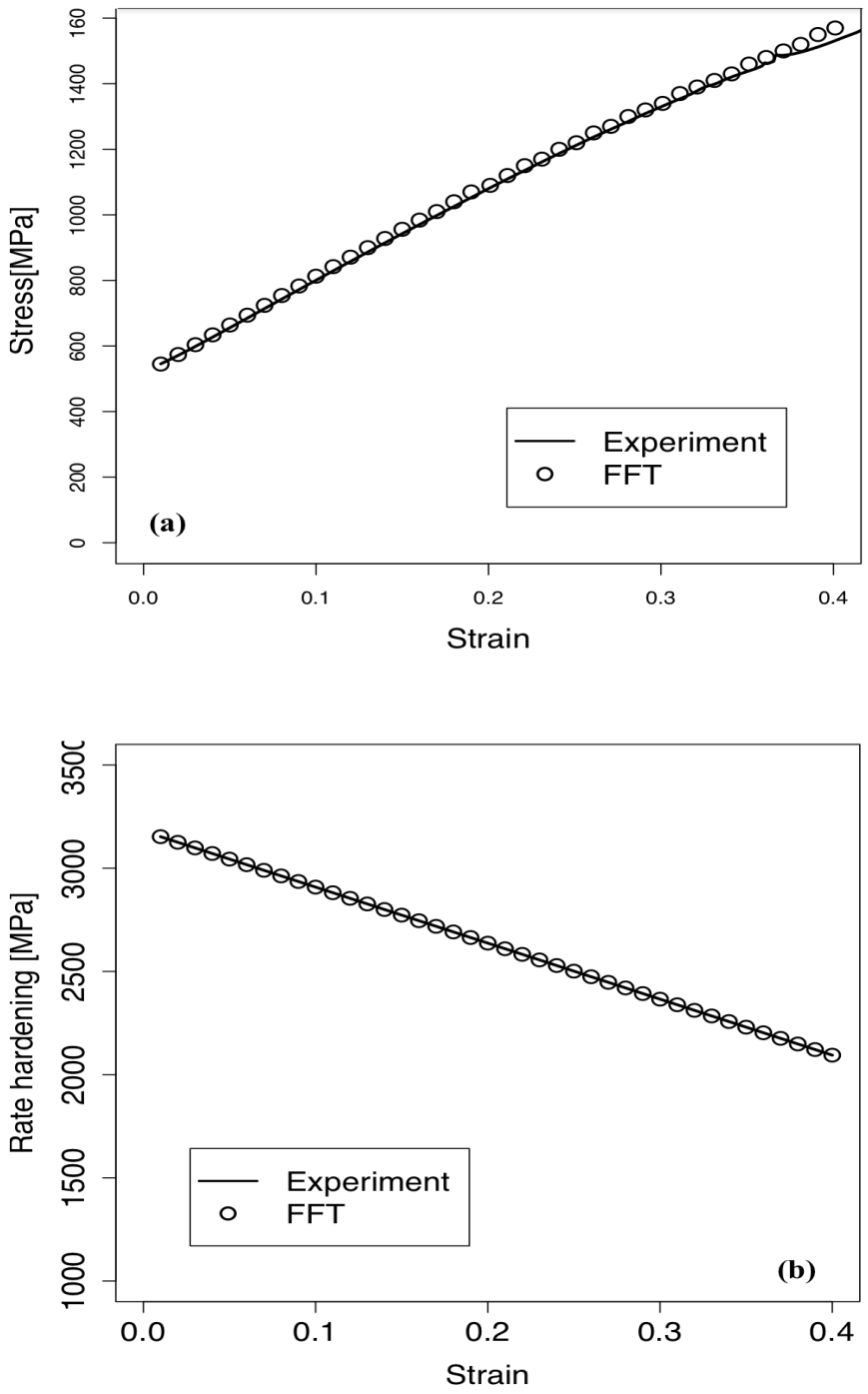

Figure 3.3 Simulation and experimental stress-strain curve

Plot of the (a) measured stress-strain response of the TWIP steel showing strong strain hardening, overlaid with the simulated curve based on the Voce model, and (b) the plot of experimental and simulation strain hardening vs. strain.

The polarity of twinning was captured by setting the negative values of τ_0 as ∞. Following transmission electron microscopy (TEM) observations [164], nearly 4 % strain of pure slip is needed before twinning triggers within favorably oriented grains. Generally, authors argue that multiple slip systems must be actively reacting to produce stable twins in an FCC lattice [187,188]. Following these common hypotheses about twin nucleation, we set $c_1 = 0.15$ in our simulations

The best fit of the TD tensile behavior in Figure 3.3a corresponded to the Voce hardening model parameters for slip and twinning that are listed in Table 3.1. A good fit did not require self-latent hardening between the slip systems nor between the twin variants. In general, assigning parameters for latent hardening requires multiaxial tests, which were not available. Similar values of self and latent hardening parameters were used by [169] in their simulations of twinning effects on the behavior of silver-copper cast eutectic nanocomposites. Table 3.1 shows that the critical resolved shear stress for twinning is more than that for slip. The τ_0 parameters reported for slip and twinning in other literature on TWIP steel [188] are, however, consistent with our results.

Table 3.1 Simulation parameters identified for the best fit of the stress-strain behavior

Parameter	Slip	Twinning
τ_0(MPa)	215	260
τ_1(Mpa)	330	460
θ_0	410	510
θ_1	225	275
$h^{s\acute{s}}$	1	1
$h^{s\acute{s}}$	1	1
c_1	-	0.15
c_2	-	0.15
n	12	12

3.5.2 Relative activities

The simulated stress-strain behavior includes both slip and twinning, and Figure 3.4a shows the variation in relative activity as a function of strain. The results show that twinning decreases during the course of deformation, which agrees with the relative activities reported in other work on the simulation of TWIP steels [189,190]. Slip is significantly more active than twinning, which is directly related to the notably higher hardening rate parameters assigned to the twinning modes, compared to those for slip. The underlying pseudo-slip approach for twinning may not be adequate to describe the fast progress of twin lamellae expected in grains undergoing a fairly homogeneous and favorable stress state distribution.

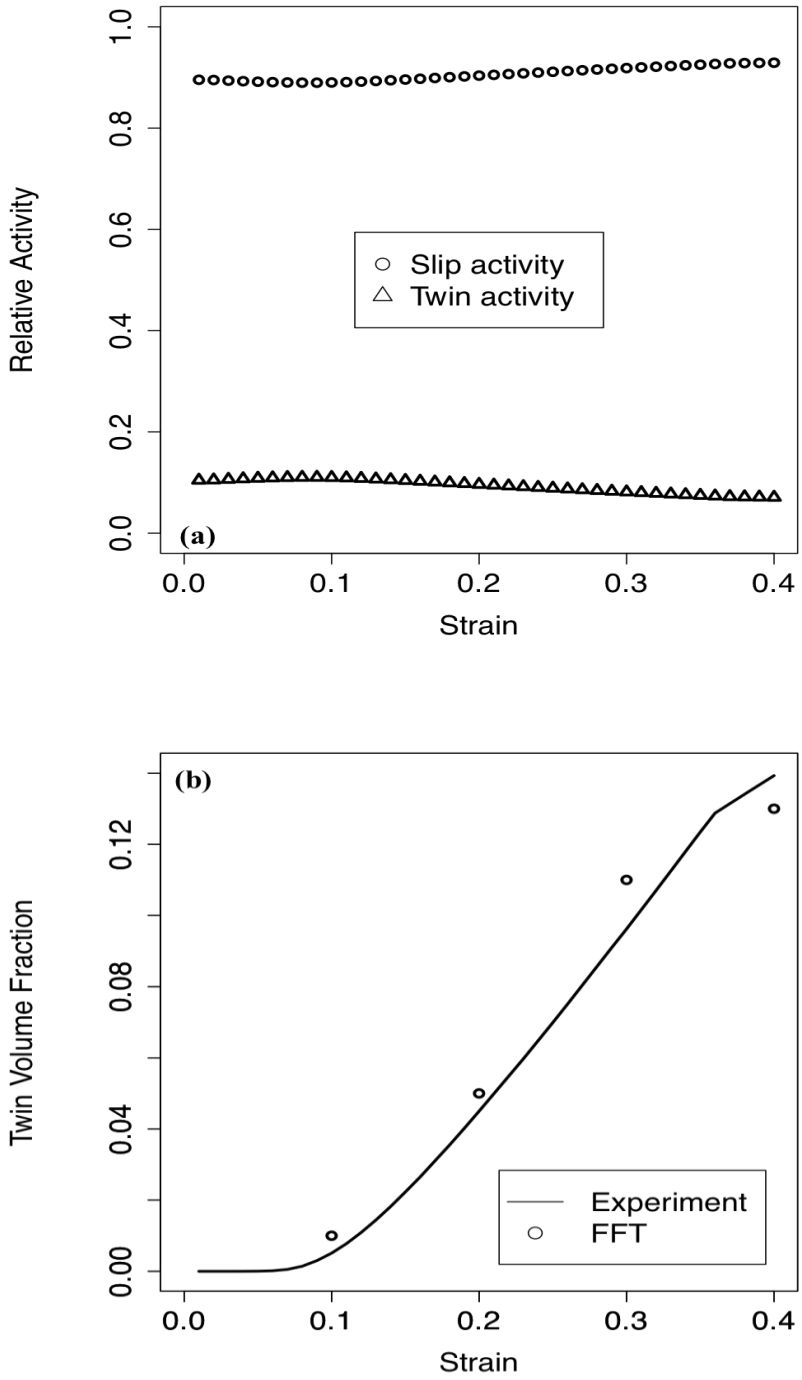

Figure 3.4 Relative activity and twin volume fraction curves

Results of FFT simulations showing (a) the relative activity of slip and twinning during deformation, and (b) the simulated evolution of the twin volume fractions in the unit cell as compared to that measured experimentally.

However, twin propagation may be obstructed by twin-twin interactions, as the 12 twin variants allow for multiple nucleation events in any given grain. Thus, the effect of twin-twin hardening on the overall plastic behavior can be considered to be implicitly included in the relatively higher values of θ_0 and τ_1 (for twinning).

Figure 3.4b shows measured and calculated twin volume fraction. The volume fraction of twins was obtained from [164] using EBSD technique. It is worth mentioning that the spatial resolution of EBSD measurement (i.e. step size) is lower than twin size (i.e. ~20 nm), which makes it difficult to resolve each individual twin. Therefore, the EBSD measurement only shows the twinned area, which consists of twin and grain matrix. In addition, most grains do not display uniform twinning. Considering these limitations arising from the EBSD technique and microstructure complexity, the volume fraction of twinned area measured by EBSD was divided by a factor of 3 [164] to estimate the volume fraction of twins at different true strains.

Overall, the vpFFT simulations, as shown in Figure 3.5a, satisfactorily predicted the evolution of twin volume fractions. The stress hot spot analysis aggregates points with high twin activity, which avoids assigning significance to individual points. As the twin distribution on the exterior surfaces of the simulation volume reveals, Figure 3.5, only a few agglomerations of highly twinned material are larger than the typical grain size in the volume.

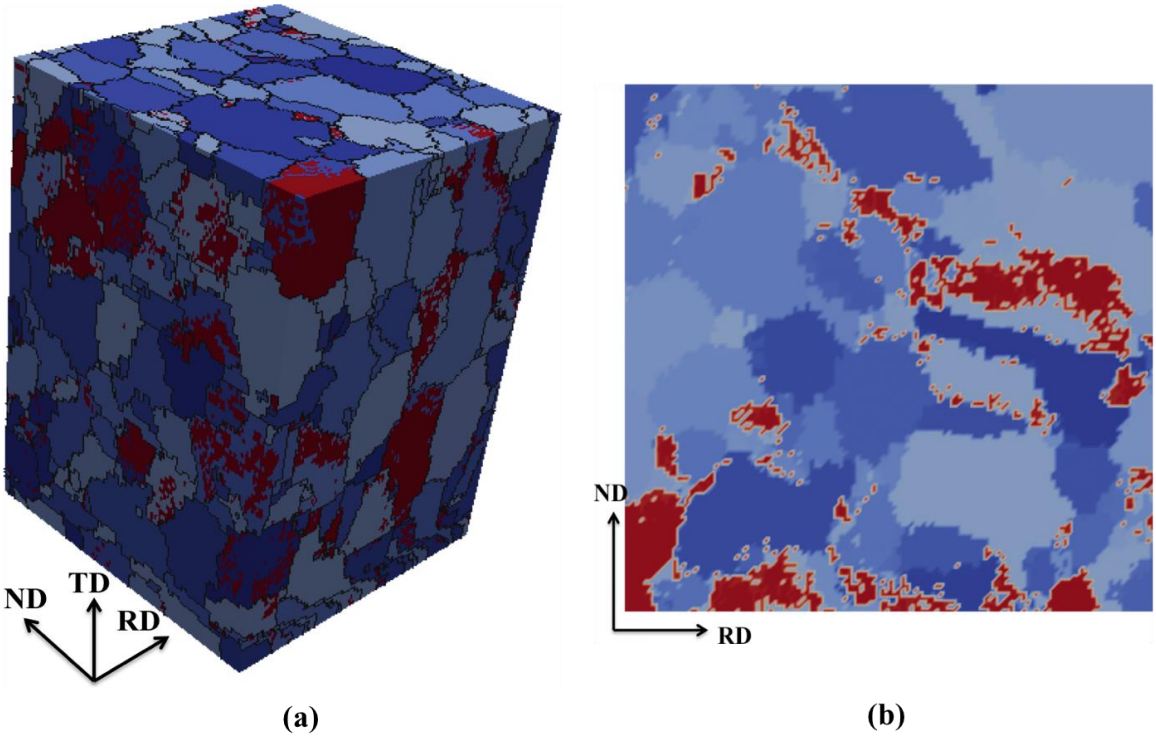

Figure 3.5 FFT simulation twin distribution on simulation box

Results of FFT simulations showing (a) twin distribution (in red) on the exterior surface of the simulation volume, and (b) twin distribution on a middle plane. To ensure that the twinned regions (red) are apparent in the figure, the grain ID-based color scale was adjusted such that non-twinned points were in the blue-white range

3.5.3 Orientation change

Figure 3.6 shows change of misorientation of each voxel deformed by slip or twinning with respect to initial condition during deformation. The orientation of voxels deformed by twinning undergoes a jump to the new twinned orientation, while other voxels deformed by slip gradually reorient in each step. Note that slip-induced lattice rotation is more pronounced around twins, indicating the important contribution of twins to localization.

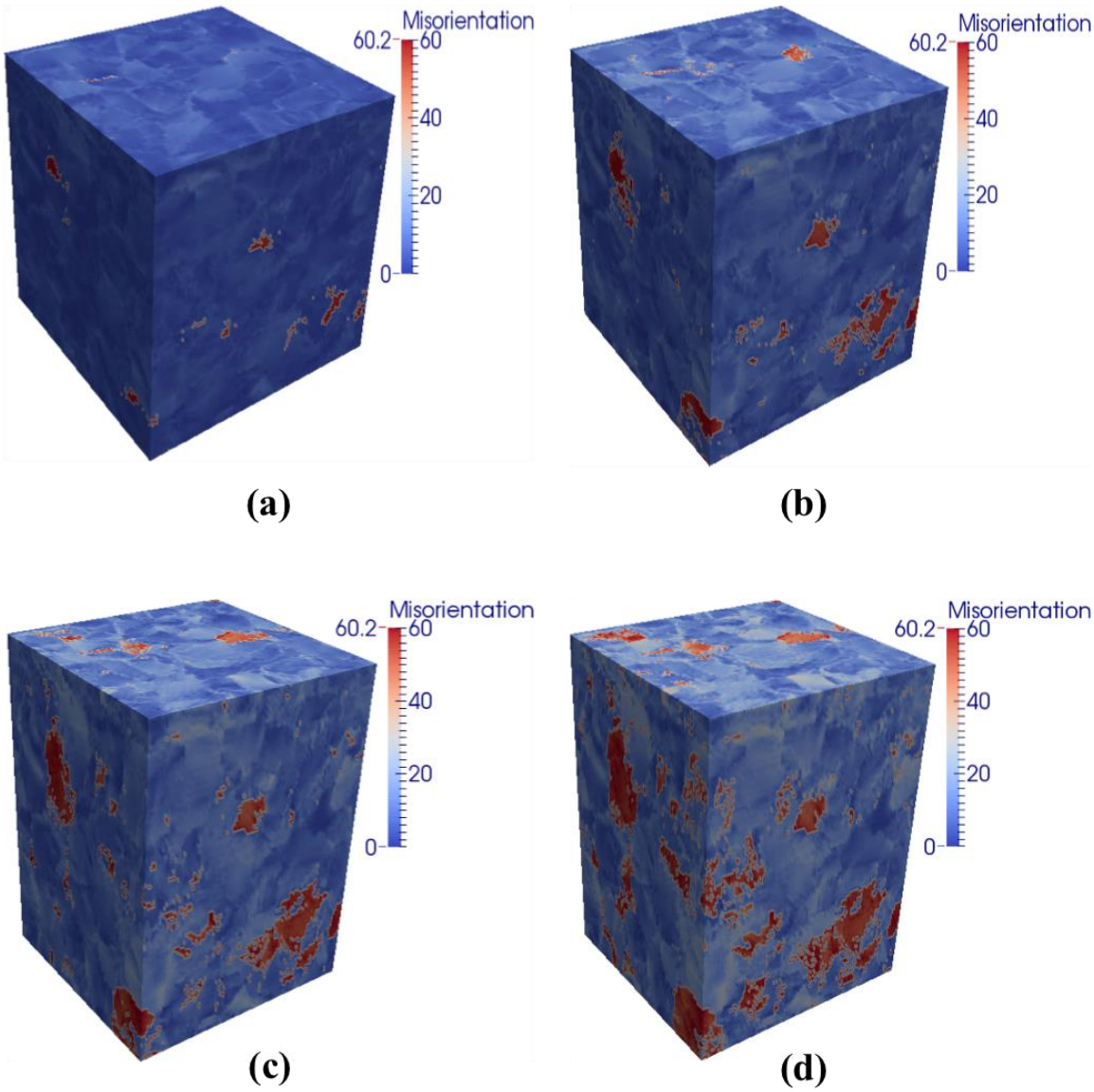

Figure 3.6 Orientation changes in each voxel during plastic deformation

Misorientation angle of each voxel with respect to initial condition (strain 0 %) in three-dimensional (a) 10 %, (b) 20 %, (c) 30 %, and (d) 40 % total tensile strain along the transverse direction. Blue regions are slip dominated, whereas red ones are twin dominated.

Field et al. [191] reported the existence of orientation gradients near twins which disappeared, caused by twin boundary migration, after performing channel die deformation in copper. Their results show that twins disappear at high misorientation

regions (e.g 10 degree) in the parent grains. Recently, using orientation microscopy by TEM confirms the presence of high geometrically necessary dislocation densities in the regions with high local misorientation [192].

3.5.4 Twin initiation at high stress regions

Twin nucleation events in low SFE FCC metals were demonstrated to follow a pseudo-slip mechanism, i.e. they trigger in regions where the resolved shear stress is greater than the critical resolve shear stress for twinning. Figure 3.10 clearly shows that most of the highly stressed voxels are located in the vicinity of grain boundaries, and the associated resolved shear stress on twinning systems is also high. Correlated with this, both Figures 3.5a and Figure 3.5b indicate that the twins primarily nucleated at regions with high local stress values (e.g. grain boundaries) and then grew inside the grains. Although the typical lamellar shape of the twins was not captured for obvious reasons inherent to the three-dimensional PTR twinning model, prediction of preferential nucleation at GBs is an encouraging feature of the FFT simulations. Twins were observed to mainly nucleate at low-angle boundaries [12,193]. Interface defects are known to mediate twin propagation in both FCC and HCP metals in some cases [193,194], the stress surrounding the twin is mainly relaxed by the motion of such defects thus accommodating twin edgewise thickening. In the following, more detailed analysis shows that twinned points tend to be also high stress points.

3.5.5 Predictions of deformation texture

The evolution of texture after 40% strain is mainly characterized by the stabilization and strengthening of the <111> || TD and <001> || TD components. A

comparison between the initial state in Figure 3.7a and Figure 3.7b suggests that the <111> TD fiber strengthened at the expense of the orientation around it. It is clear that there is over-prediction of <001> || TD in the FFT simulation compared to the experimental results. De Cooman et al [195] showed the similar over- and under-prediction of the <001> and <111> fibers in Al-added TWIP steel by VPSC. They mention that the Brass-type texture in Al-added high SFE TWIP steel is stronger than that in Al-free low SFE TWIP steel. This property increases the intensity of Goss orientation relative to Brass orientation in Al-added TWIP steel, in which the Goss component is the preferred orientation for slip and micro shear banding [190]. Both the Cu-texture {112}<111> and Goss-texture {110}<001> in the τ fiber gradually increase with increasing strain in Al-added TWIP steel [195]. Therefore, the <001> || TD in Figure 3.7d mostly contains twin free grains with <001> texture. Moreover, the higher fraction of <001> texture in the FFT input (Figure 3.2b) causes a stronger <001> FFT prediction compared to experimental one.

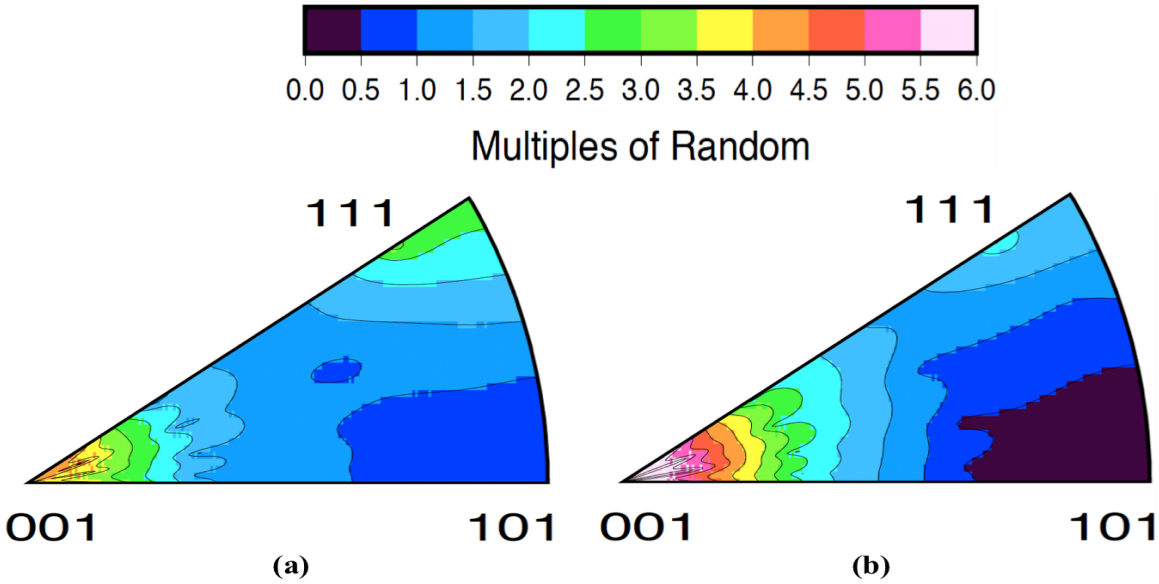

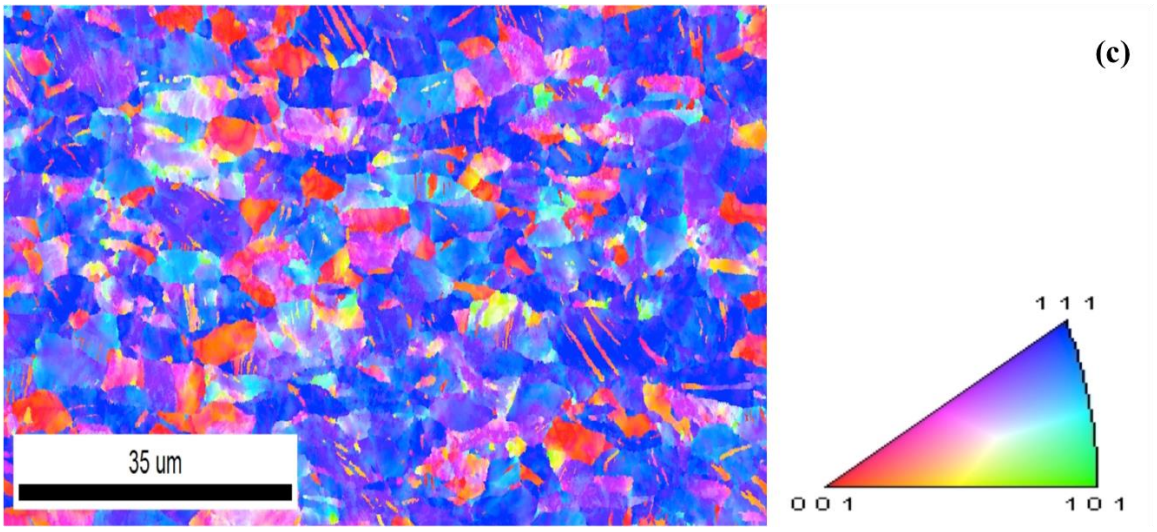

Figure 3.7 Predicted and measured final texture after tensile deformation

Comparison of TD-mapped inverse pole figures of (a) measured and (b) FFT simulated after 40\% total tensile strain along the transverse direction. (c) IPF map measured by EBSD after 40\% total strain along TD. Note that the tensile axis was aligned with the original TD.

3.5.6 Effect of linearization scheme on texture prediction

Different methods are available to linearize the stress and strain relation in a grain scale, and the selected linearization method influences the accuracy of the predicted texture. Tangent, secant, affine, and n^{eff} are linearization methods implemented in the VPSC code [180]. To investigate the effect of these linearization methods on the output texture and grains rotation, VPSC simulations were performed under uniaxial tension to a strain of 0.4. Figure 3.8 shows the resulting VPSC simulations taking FCC random texture as an input. The results reveal that grains rotate toward <111> or <001> direction, and their rotation angles are a function of the linearization scheme. The general trend of each grain rotation is consistent with 3DXRD texture measurement in copper under tension [196]. Interestingly, the fraction of grains, which tend to align in a direction <111> or <001>, strongly depends on the linearization approach. Moreover, Figure 3.8 reveals that the intensity of <001> and <111> in predicted textures changes with the linearization methods. According to the full constraint (FC) Taylor model (compatibility) [197], tension on FCC metals develops texture with stronger <111> fiber and weaker <001> fiber aligning along the tensile axis . Therefore, the secant linearization scheme calculates a more realistic texture, while the other linearization schemes (tangent, affine, and n^{eff}) predict stronger <001> and <001>-<111> fibers compared to experimental ones. Lebensohn et al [180] reported that when n (rate-sensitivity exponent) gets higher values, the tangent approximation predicts a uniform stress-state like Sachs equilibrium based approximation (lower bound). On the other hand, the secant estimation is stiffer and predicts a uniform strain-rate similar to Taylor based compatibility approximation (upper bound).

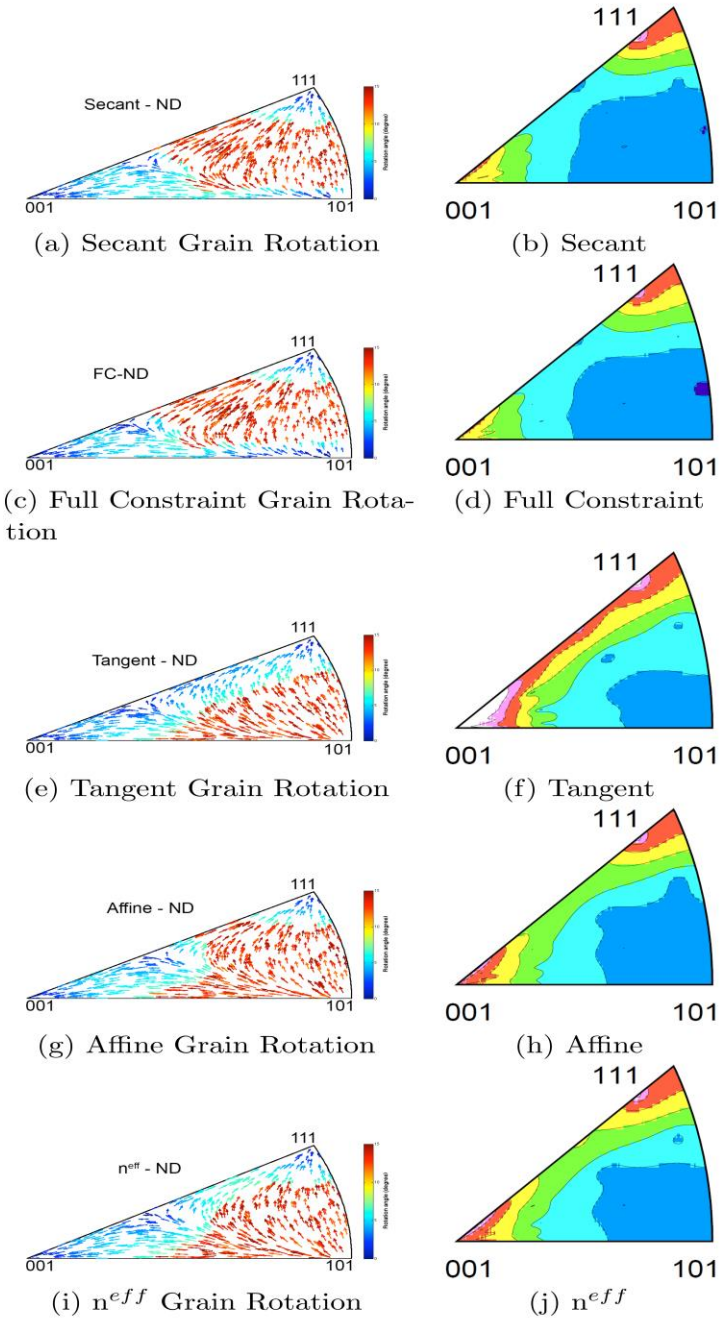

(a) Secant Grain Rotation (b) Secant

(c) Full Constraint Grain Rotation (d) Full Constraint

(e) Tangent Grain Rotation (f) Tangent

(g) Affine Grain Rotation (h) Affine

(i) n^{eff} Grain Rotation (j) n^{eff}

Figure 3.8 Effect of linearization scheme on texture prediction

Inverse pole figures of output texture and rotation maps of 500 grains along Tensile direction, after applying 40% tensile elongation in VPSC with linearization scheme, with arrows pointing from the location prior to deformation to that at 40% strain.

However, the vpFFT formulation uses the tangent method to linearize local stress and strain relation in each Fourier point (in equation III-1), which causes stronger predicted <001> fiber compared to experimental one.

3.5.7 Grain scale deformation texture

Development of dislocation pile-ups, which cause a local stress concentration, and activation of multiple slip systems [198] are thought to be necessary for initiation of mechanical twinning. TEM investigation in a single grain of Hadfield steel shows that mechanical twinning does not occur in the orientation <-123> || TD, even though this orientation has a high Schmid factor for twinning. The <-123> || TD orientation is less favorable for multiple slip compared with more symmetric orientations, which is essential to mechanical twinning nucleation. TEM observations show mechanical twinning is activated in grains with low Schmid factor while twinning can fail to appear in grains with high Schmid factor [199,200].

In the literature, several authors performed a Schmid factor analysis to explain the frequency of mechanical twinning as a function of orientation [201,202]. However, Schmid's law is only reasonable for single crystals with an isostress condition leading to single slip, and it is not able to capture grain interaction and strain compatibility in the grain boundaries with neighboring grains [203]. Other simulation work shows better prediction of the active twinning mode with the Taylor model compared to the Sachs model. The multiple slip approach results in a different stress state in each grain and can identify mechanical twinning formation at small strains [204].

To identify the role of twinning on texture, Figure 3.9 shows the simulated IPFs for voxels in twins, voxels near twins, and voxels in twin-free grains, all of which can be

compared with the experimental result, Figure 3.7a. Figure 3.9a and Figure 3.9c indicate that most of the strengthening of the <001> || TD is due to deformation twinning which has primarily subtracted from the <111> || TD component. Twinning of this component is substantiated by the EBSD inverse pole figure map, Figure 3.7c after 40% strain deformation. In this figure, blue grains, showing <111> || TD, contain twins whereas the red grains, <100> || TD, may be fully twinned or twin-free.

To understand the origin of texture component, the Taylor factor of an FCC metal subjected to uniaxial tension with {111}<110> was calculated for different orientations in the inverse pole figure triangle (Figure 3.9d) [203]. The comparison of the IPF for voxels near twins and voxels in twin-free grains reveals that they have high ($M < 2.6$) and low Taylor factors ($M > 3.4$), respectively. These results are consistent with experimental work performed on the same material [164]. However, the IPF of voxels near twins reveals additional, but weak texture components between <001> || TD and <111> || TD fibers, which are not present in the experimental IPF. Similar results were reported in other simulations on TWIP steel with no clear explanation [195]. Since these components do not appear in twinned voxels, it is likely that they originate from regions undergoing localization, such that the active slip systems vary considerably. This explanation correlates well with the high Taylor factors associated with the <111> || TD fiber. In general, grains with a high Taylor factor require higher stresses for plastic deformation. The active slip systems vary to satisfy strain compatibility and stress equilibrium in the near-grain boundaries regions.

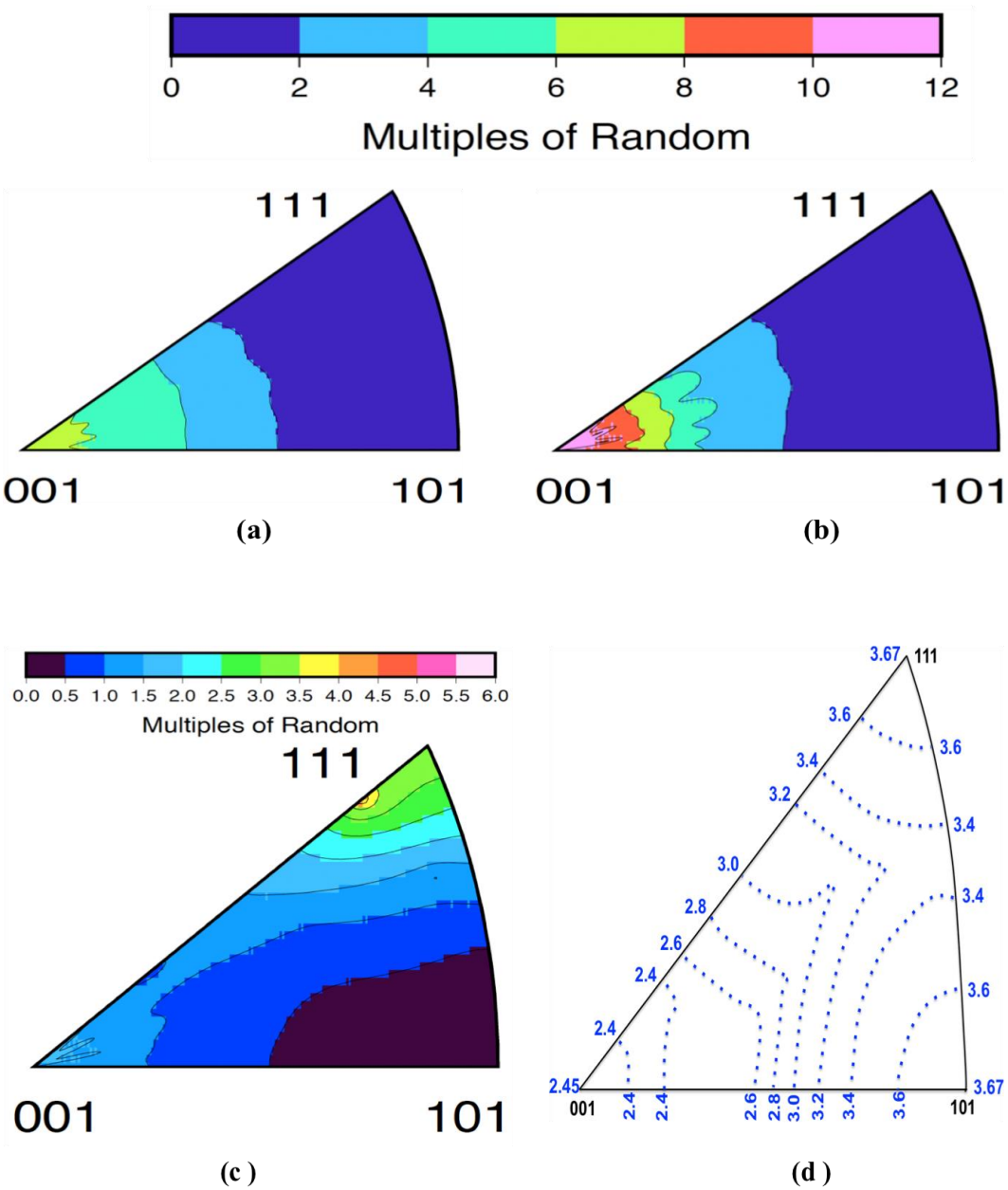

Figure 3.9 Grain scale texture prediction

Results of FFT simulations showing inverse pole figures (IPFs) corresponding to (a) twinned voxels, (b) voxels near twins, and (c) twin-free grain voxels after 40% total tensile strain along the transverse direction. (d) Inverse pole figure along tensile axis direction showing Taylor factor values, the dotted line correspond to the Taylor factor value for each specific orientation in triangle, the values were calculated for slip system {111}<110> in FCC randomly textured deformed under uniaxial tension.

Therefore, the voxels near twins with a high Taylor factor, e.g. <111> || TD, are well oriented for multiple slip as well as mechanical twinning. In contrast, the voxels in twin free grains with low Taylor factor can deform at lower stresses. In other experimental work, Miura et al [205] reported that the <001> || TD orientation promotes cross-slip, causing relief of stress concentration that might otherwise promote twinning.

3.5.8 Prediction of stress localization

Figures 3.10a-3.10b show the stress and strain rate distribution on the exterior surface of simulation volume after 40 % strain deformation. The local variations in stress (Figure 3.10c) and strain rate (Figure 3.10d) exhibit different features in the two fields; mainly, the stress histogram has two peaks and the strain histogram exhibits a long upper tail. The latter indicates that a small fraction of grid-points experienced substantially high strain rates. This may be visible in the 3D strain rate plot of Figure 3.10. Figure 3.10 shows the distribution of local strain and stress on the surface of the simulation volume, which is changing with grain structure. The variations of local stress by grain structure are more visible than that of local strain rate. Similar features were reported by other researchers [181,206,207].

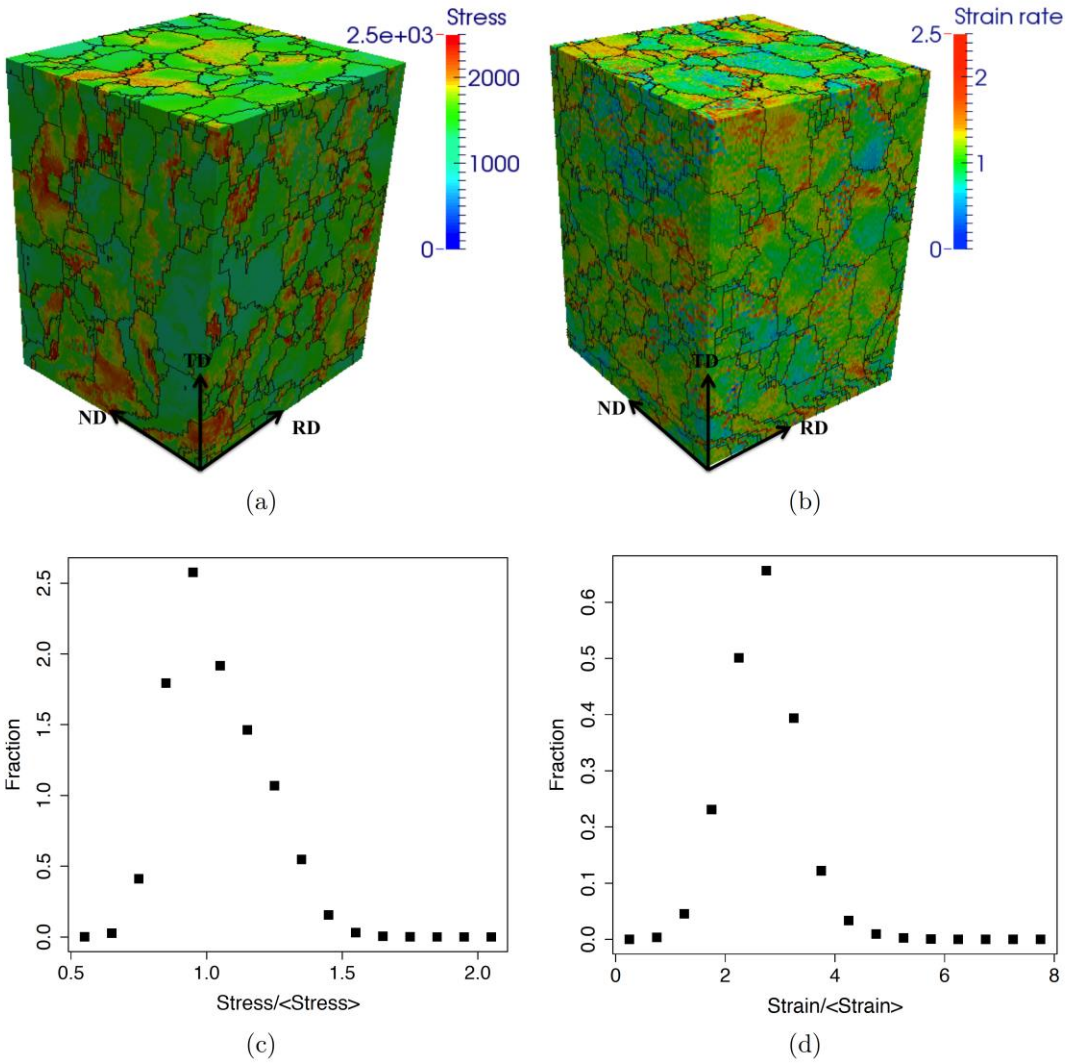

Figure 3.10 Distribution of local stress and strain rate on the surface of simulation box

von Mises (a) stress and (b) strain rate fields on the surface of the simulation volume and (c-d) their corresponding histograms, respectively

To find a relation between local stress and orientations of twinned voxels, IPFs generated by orientations of twinned voxels, which experienced a stress higher than, versus less than 90% of the peak stress are shown in Figure 3.11, respectively. These IPFs clearly indicate that the most highly stressed points (relative to the peak stress) correspond to an increasingly sharp <001> || TD texture. This suggests that most of the

twinning happens in the voxels with high local stress, even though the criterion for twinning is strain-based. Correlation of hot spots in stress to twinning was previously reported with measurements of backstress effects in a low stacking fault energy steel [195].

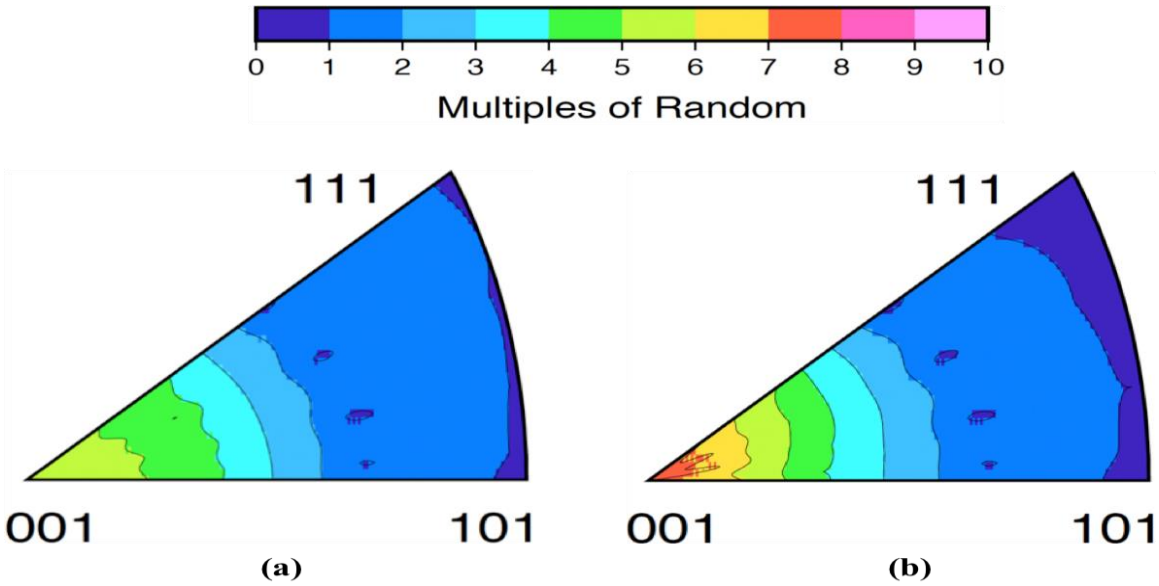

Figure 3.11 Relation between orientation of twinned voxel and local stress

Inverse pole figures revealing textures of twinned voxels in the regions with stresses less than (a) 0.9 of the peak stress, and (b) greater than 0.9.

In order to quantify the relationship between twin voxels and local stress, the Euclidean distance map for twinned voxels was computed. In the grains containing twinned voxels, the minimum distance between untwinned voxels and twinned voxels was computed. This distance was binned based on the stress value and the distance values averaged over the points in each bin. Figure 3.12 shows the calculated plot of average distance to twinned voxels. In this graph, each point depicts the average distance to the

closest twinned voxel, and the vertical and horizontal axes were normalized by the global average distance and average stress, respectively. Figure 3.12 indicates that higher local stresses are found adjacent to twinned voxels, which suggests that twins induce hot spots close to their boundaries.

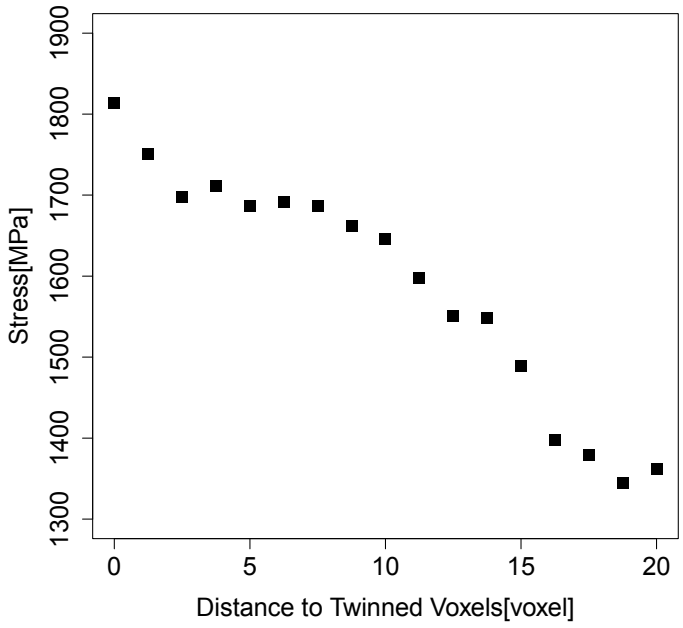

Figure 3.12 Plot of the average stress vs. distance to the twinned voxels

3.6 Conclusion

A PTR method was used to incorporate deformation twinning in a full-field, three-dimensional framework that uses the fast-Fourier transform modeling technique to compute the visco-plastic response of a face-centered cubic (FCC) steel with a Mn-induced low stacking fault energy (SFE). Hardening was described through the Voce model, which treats twinning as a pseudo-slip mechanism. The occurrence of twinning at any given grid point is controlled by a criterion based on a threshold in accumulated slip

that controls when a jump in lattice orientation is applied. The scheme does not contain rules for lengthwise versus edgewise growth of twin lamellae so the final microstructural morphologies and grain boundary texture likely contain artifacts from the sequence of grid-point interrogation. However, the successful reproduction of the observed evolution of the twin volume fractions and texture upon strain provide some confidence in the approach. The main results are as follows.

1. The strengthening and stabilization of sharp and homogeneous <111> ||TD and <001> || TD and fibers typical of low SFE FCC metals was satisfactorily reproduced. The strengthening of the <111> ||TD was mainly because of slip and marginally as a consequence of twinning of the <001>|| TD oriented grains. The development of the <011> || TD was largely caused by twinning of the developed <111> || TD fiber.
2. Both twinning and slip evolve the texture to balance between the two major fibers, so one may expect that twin re-orientation and segmentation cause a radical change and evolution in orientation boundary distribution, which greatly influences localization.
3. A plot of local stress value versus distance to twin boundaries reveals that local stress increases with decreasing distance to twin boundaries, and the value of the local stress in the voxels close to the twinned voxels is highest.

CHAPTER IV

A BRIEF REVIEW OF THE CURRENT STATE AND CHALLENGES TO CAPTURING THE EVOLUTION OF THE LAMELLAR MORPHOLOGY OF TWIN NUCLEATION AND PROPAGATION IN FULL-FIELD CRYSTAL PLASTICITY IN HCP METALS

4.1 Introduction

As we previously mentioned, deformation twinning in HCP materials proceeds in three-stage growth (As in fatigue and fracture mechanics, we mean by growth a process which includes nucleation, propagation, and coalescence) process as illustrated in the two-dimensional schematic of Figure 4.1. These three stages are 1) nucleation of a small embryo, which is usually achieved at the sample free surface or a grain boundary, 2) drastic lengthwise thickening across one or multiple grains, and 3) edgewise propagation or thickening. Most of the shape change is accomplished during the last stage. Shear stress at the twin-parent interface drives the shear strain, which is brought about by glide of disconnections having a step character responsible of the volume increase of the twin.

Deformation twinning is generally much easier in hexagonal closed packed (hcp) crystal structure than in their cubic counterparts. In Mg, $\{10\bar{1}2\}$ twinning can completely get a favorably oriented grain even at the quasi-static regime and ambient temperature. This relatively ease of twinning is widely attributed to the great difficulty of achieving

slip along <c+a> pyramidal planes, which is necessary to provide $\langle c \rangle$-axis deformation when needed. In fact, the $\{11\bar{2}2\}$ planes on which the $\langle 11\bar{2}\bar{3} \rangle$ dislocation was observed to glide [17] exhibit atomic zigzags along the slip direction [208]. These zigzags prohibit a "Shockley" type dissociation to occur. Thus, a zonal core of the dislocation, spreading on multiple planes, may be required on multiple planes instead, so to ease the high shear associated with the pyramidal slip. In fact, if such a fault occurs to accommodate the glide of an extended Frank-Nicholas dislocation [209], an energy almost equal to that of crack formation would be required [208]. This paradigm for explaining the ubiquitous formation of twinning in hcp metals is clearly supported by the vanishing twinning activity when temperature increases, which causes a dramatic decrease of the critical stresses, associated with non-basal slip, and particularly the second order pyramidal $\langle c + a \rangle$ slip.

However, this widely held paradigm for the ease of twinning in hcp metals does not explain why $\{10\bar{1}1\}$ compression/contraction twinning, for example, is much more difficult in Mg than the second order pyramidal $\langle c + a \rangle$ slip. Only the $\{10\bar{1}2\}$ twinning which accommodates tension/extension of the $\langle c \rangle$-axis has a critical resolved shear stress comparable to that of basal slip. Hence, the formation of twins in hcp is more to do with the ease of this particular twin mode than the high critical resolved shear stress of non-basal dislocations with Burgers vector having a $\langle c \rangle$ component. This view is substantiated by the continuing predominance of $\{10\bar{1}2\}$ twins in Zn and Cd despite that, as dictated by the sign reversal of its characteristic shear; they turn to accommodate compression of the $\langle c \rangle$ axis.. Furthermore, $\{10\bar{1}2\}$ twinning exhibits several growth peculiarities, which set them clearly aside from all other twinning modes. For instance, detwinning and twin

transmission across twins and grain boundaries were not observed to occur in other twins modes, while they have important effects on the macroscopic behavior and anisotropy.

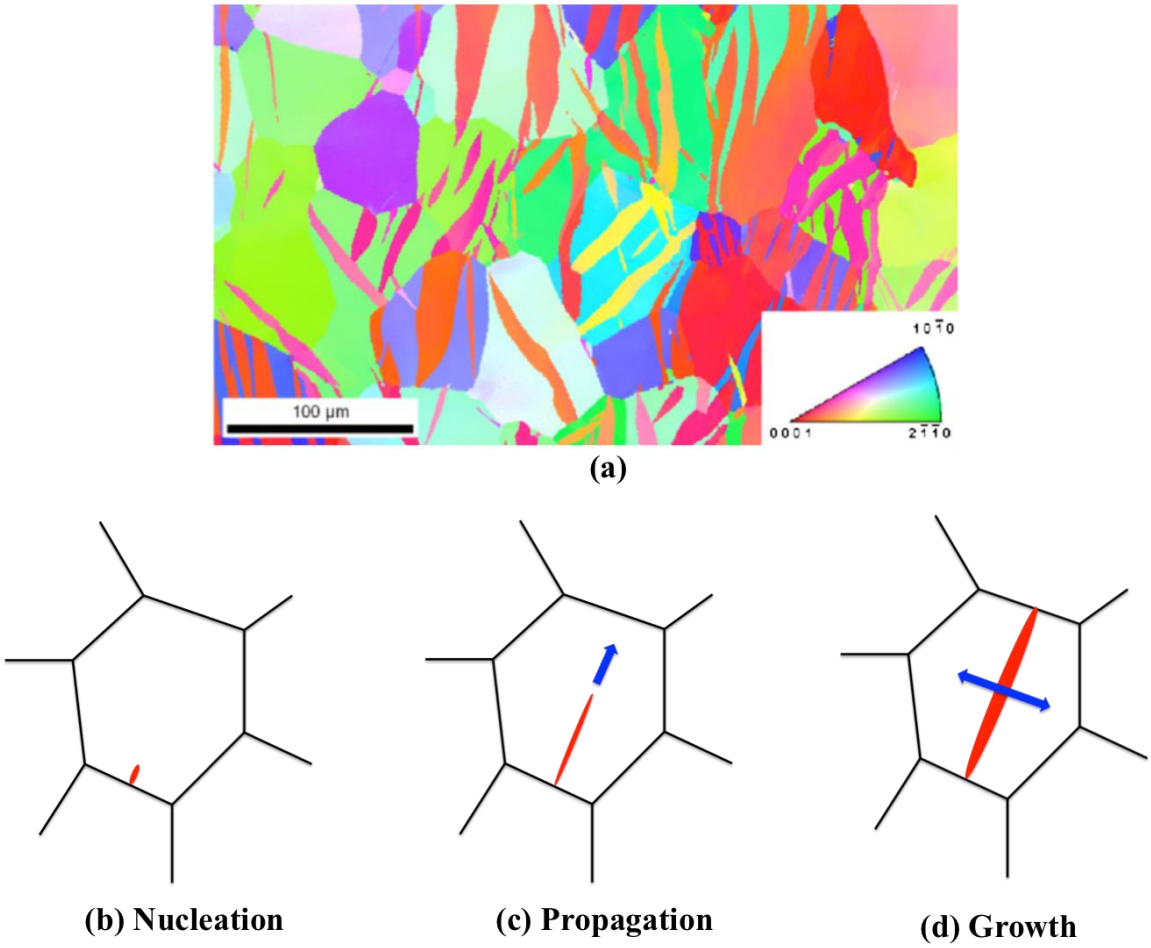

Figure 4.1 Three stages of mechanical twinning

(a) Inverse pole figure map of high-purity Mg loaded to 3% strain to induce $\{10\bar{1}2\}$ twinning [41], Two-dimensional simplification of the three stages characteristic of a lamellar, deformation twin growth. (a) Nucleation of a twin embryo at grain boundaries, (b) twin propagation inside the grain by drastic lengthwise thickening, and (c) edgewise twin propagation by, increase of twin thickness.

This lack of understanding of the nucleation and growth of twins in hcp metals explains the sluggish progress made in capturing twins in crystal plasticity as localized

grain lamella. At present, both nucleation and propagation of twins, despite their highly localization character, are modeled by a pseudo-slip approach, where the volume fraction is simply controlled through the classical crystallographic relationship between shear on the twin plane and the characteristic shear constant of the twin mode (eg. 0.13 for $\{10\bar{1}2\}$ in Mg). Thus, similarly to slip, twinning is viewed as a diffuse deformation mechanism in the matrix, which limits a reliable prediction of its effect on stress hot spots and damage initiation.

This thesis section briefly reviews recent attempts to capture twinning as local event in full field crystal plasticity and discusses some of the challenges associated with the incorporation of the main micromechanical characteristics of twinning in the framework of EVPFFT. We benchmark these discussions by simulating the behavior of a couple Mg bicrystals, hoping to shed light on some of the main barriers to be overcome in future work.

4.2 Modeling of Twin nucleation

EBSD measurements of mechanical twinning in Zr and Mg alloys suggest that the most of twins nucleate at the sample free surface in single crystals or at grain boundaries of metals with sharp textures, and start nucleating as texture gets weak [210,211]. The reason for the high propensity to nucleate at the free surface resides in the ease of accommodation effect by kinking, while in the bulk nucleation of a twin will require plastic accommodation by slip or nucleation of another twin (typical for sharp textures). In all other cases, twins were observed to start at grain boundaries for the following mechanisms [212] :

1. Grain boundaries provide large partial dislocations and multiple twinning dislocations.
2. Multi-layered stable twin needs rearrangement and restructuring of atoms that are supported by grain boundaries.
3. High stress concentration at grain boundaries could provide the energy to overcome twin nucleation barriers.

As mentioned in Section 1.2.1, one of the main reasons relevant to crystal plasticity and for which twins tend to nucleate at surface defects such as grain boundaries is the stress concentration that builds up in these regions. These stresses arise because of the difficulty associated with cross slip of early basal slip onto planes and directions kinematically compatible with providing shape change along the $\langle c \rangle$-axis. In a similar view, Beyerlein and Tomé [212] suggested that randomness correlated with grain boundary type and character are probably the source of the observed fluctuations in spacing and morphology of deformation twins in hcp materials. These random characteristics are divided into material components and mechanical components. The material components refer to the critical stress or energy, which is required to convert grain boundaries defects into twin-related disconnections and random mechanical components are determined by distribution of the local stresses at grain boundaries.

Twin nucleation is sensitive to both the microstructure (e.g. grain size, orientation, and dislocation density) and loading conditions (e.g. strain rate, temperature, and stress level) at the mesoscale [212]. Beyerlin et al. [69] reported that the propensity, frequency, and morphology of deformation twins are different among grains with the same orientations and applied boundary conditions. Therefore, based on these variances,

they suggested that twin nucleation at grain boundaries is a largely stochastic or random process in the grain scale.

Statistical analyses carried on EBSD measurements on deformed Zr and Mg revealed effects of additional microstructural features such as grain boundary misorientation on nucleation and growth of {10-12} twins [43]. The results supported the random nature of twin nucleation and indicated that twin nucleation and grain area do not show a meaningful one-to-one correlation. Moreover, grain misorientation larger than 5 degrees does not have significant effects on twin nucleation at grain boundaries. The twin variants with the highest Schmid factor have the highest probability of activation (50-60%), while the probability of twin variants with the second highest Schmid factor values is around 23% [211]. As stated in the introduction, these results substantiate a CRSS for twinning, while nucleation of secondary twins occurs in regions where lattice rotations favored a high Schmid factor.

In a similar statistical study performed on Mg, Beyerlein et al [212] showed a correlation between high Schmid's factors and twin thickness. This positive correlation was attributed to the fact that well oriented twin variants can more easily overcome the backstresses developed during growth (Figure 4.2b).

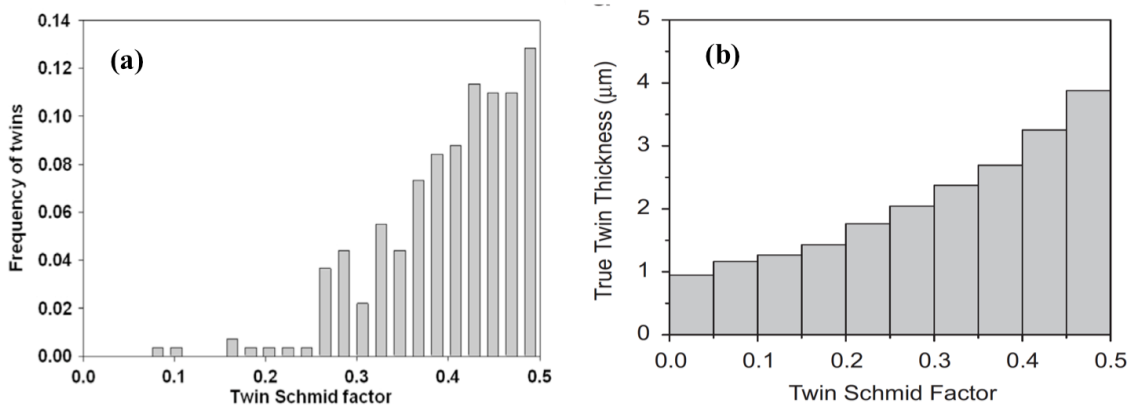

Figure 4.2 Effect of twin Schmid factor on probability and thickness of twin

(a) Distribution of the Schmid factor with respect to observed twins [211], and (b) measured twin thickness as a function of the Schmid factor [41]

Aydiner et al. [213] used a three dimensional X-ray technique to measure the average resolved shear stress on twin systems during twin nucleation and growth in AZ31 alloy subjected to compression. When a twin nucleates, the average value of resolved shear stress on twin plane along the twin direction is not equal to that in the parent (Figure 4.3a). Furthermore, the sign of the resolved shear stress (RSS) on the composition plane inside the twin is opposite to that inside the parent. The opposite sign of the shear stress on twin variants can be due to the local backstress. The local backstress is a result of internal constraints, which are imposed by the surrounding grains in response to the localized shear transformation during nucleation. Similar results in were reported by Bieler *et al*. [214] in Ti subjected to tension (see Figure 4.3b).

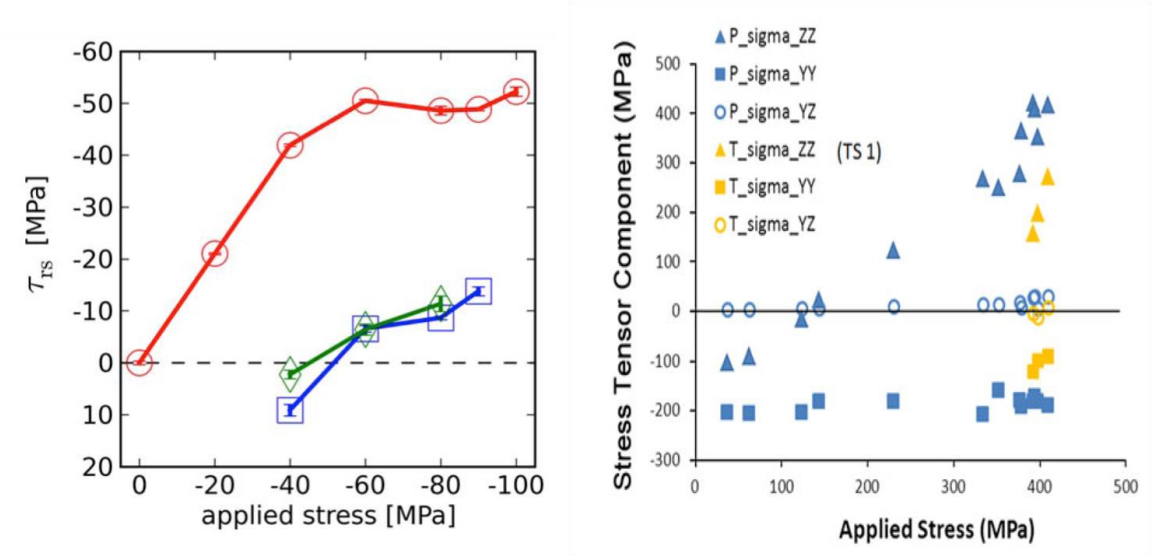

(a) **(b)**

Figure 4.3 3DXRD measurement of resolved shear stress on twin system

Measured resolved shear stress by 3DXRD on twin system along twin direction in the twin and the parent, (a) in AZ31 under compression [213], and (b) in pure Ti subjected to tension [214].

Based on the hypothesis that twin nucleation is a random event, Beyerlein et al. [212] presented a probabilistic mesoscale model for twin nucleation. This model relied on three major assumptions:

1. Twins mainly nucleate at grain boundaries,
2. Under a local stress state, transformation of grain boundary defects into partials required for creating a twin nucleus
3. Formation of a stable twin nucleus happens at the appropriate stress , which is generated in the vicinity of the defect.

Following these three hypotheses, these authors reported that a number of N of dissociation events can be a function of both the grain boundary surface area and local stress. N is a random variable, which depends on the statistical distribution of grain

boundary defects. The probability for $N = m$ in a grain boundary with surface area a, can be expressed as:

$$P(N = m, a) = \frac{(\lambda a)^m}{m!} \exp(-\lambda a) \quad (4.1)$$

where λ is the dissociation rate per unit area being a function of local stress:

$$\lambda(\tau) = \frac{1}{a_0} \left(\frac{\tau}{\tau_0}\right)^{\alpha} \quad (4.2)$$

where α and τ_0 are characteristic values of grain boundary defects in the grain boundary area. α represents the ordered or disordered structure of grain boundaries. For example, higher α value is considered for ordered grain boundary structure (e.g. 10), while the lower values act for disordered grain boundary structure. To implement the discrete probability Equation IV-1 in a crystal plasticity continuum model, a continuous probability function (F) for twinning was introduced as follows,

$$F(S < \tau) = P(N \geq m^*, a_c) = 1 - \sum_{m=0} P(N = m, a_c) \quad (4.3)$$

where a_c is a characteristics area, and m^* is the minimum number of N number of events, which must take place in a_c for twin nucleation. S is a random variable representing the critical stress for twin nucleation anywhere within the characteristics region a_c,

$$F(S < \tau) = 1 - \exp\left(1 - \left(\frac{\tau}{\tau_{nucl}}\right)^{\alpha}\right) \quad (4.4)$$

Equation (IV-4) is a Weibull distribution such that if $m^* = 1$, at least one conversion event will occur in a_c for a single twin nucleation.

These formulations were implemented in the Viscoplastic Self-Consistant (VPSC) model to calculate RSS in the direction of twin dislocation [41]. The VPSC approach is a

mean field approach for computing the global stiffness tensor, which approximates the strain around a given grain by the average strain of the entire aggregates, and calculate thereupon via an iterative procedure the average stress ${\sigma^g}_{ij}$ in each grain. This yields the RSS τ^g for a grain having ${m^g}_{ij}$ as the Schmid tensor:

$$\tau^g = {m^g}_{ij}{\sigma^g}_{ij} \quad (4.5)$$

It is clear that the local stress near the grain boundary is different from the average strain of the polycrystalline material. This could be however corrected by a perturbation stress $\Delta\sigma$ such as:

$$\sigma^{gb} = \sigma^g + \Delta\sigma \quad (4.6)$$

where σ^{gb} is local stress near grain boundary that is larger than average stress in each grain. The RSS on twin system near grain boundary is computed as following:

$$\tau^v = {m^v}_{ij}{\sigma^{gb}}_{ij} \quad (4.7)$$

where τ^v is RSS for a given twin system. A twin system with the maximum RSS is selected as the active variant.

4.3 Modeling of twin growth

Twin lengthwise thickening takes place immediately after twin nucleation at grain boundaries. The lengthwise thickening process of mechanical twinning bears a lot of similarities with crack propagation [215]. The stress for propagation is substantially smaller than that for forming a stable twin embryo. Consequently, twin nuclei propagate to a favorable size to lower the high elastic energy that builds up around the embryo.

To investigate stress evolution around twin lamellae during propagation, Aydiner et al. [213] performed in situ three dimensional XRD to investigate the evolution of stress state in the twins and their AZ31 parent being was subjected to tension.

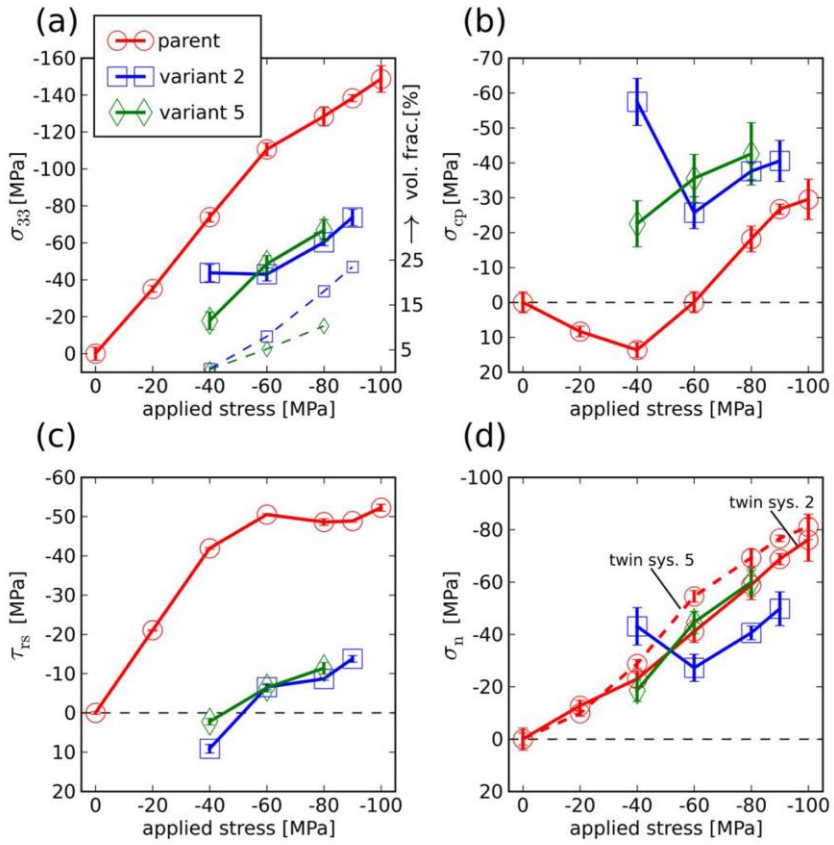

Figure 4.4 Projection of measured stress tensor in parent and twin

Projection of stress tensor in parent and twin (color legend describes the curve associated with twin and parent) as a function of applied loading: (a) σ_{33}, crystal stress tensor along loading axis, (b) σ_{cp}, component of the stress tensor along c-axis of parent, (c) τ_{rs}, resolved shear stress in twin plane along twin direction from average measurements of stress in the parent and twin, (d) σ_n, the stress tensor component along twin plane normal for each variant [213].

Due to the drastic lengthwise propagation, a kink would need to form. To prevent the parent grain from localized shear deformation, the area surrounding the twin

undergoes a backstress, which depends on the overall plastic resistance of the parent. Up on twin nucleation, τ_{rs} on twin plane has reached CRSS at approximately -40 MPa of applied stress, and the sign of the average shear stress on twin variants in twinned regions is opposite to that in the parent, and increases rapidly with the applied stress to become positive at approximately -50 MPa of applied stress depending on the twin variant. However, the average resolved shear stress on the twin plane inside the twin remains always substantially lower than that inside the parent for the entire applied stress range. This "seemingly" violation of the traction-continuity condition indicates strong stress gradient across the twin interface.

Crystal plasticity based on finite element (CPFEM) gives a full field solution, and is able to compute an approximation of the local stress at twin-parent interface, which can be used for twin growth simulation [216,217].

Recently, Kumar et al. [218] used elasto-vicoplatic version of FFT to compute evolution of local stress in the vicinity of an embedded twin in HCP grain at microscale. They modified the EVPFFT model to consider the strain associated with twin transformation, by rewriting the constitutive relation as follows:

$$\sigma(x) = C(x): \varepsilon^{el}(x) = C(x): (\varepsilon(x) - \varepsilon^{pl}(x) - \varepsilon^{tr}(x)) \qquad (4.8)$$

where $\sigma(x)$ is the Cauchy stress, $C(x)$ is the elastic stiffness tensor and $\varepsilon^{el}(x)$ is elastic strain at each point x. The elastic strain can be written in terms of the total strain $\varepsilon(x)$, plastic strain $\varepsilon^{pl}(x)$ due to slip dislocations, and transformation strain $\varepsilon^{tr}(x)$ associated with twin transformation. They proposed the following expressions for $\varepsilon^{pl}(x)$ and $\varepsilon^{tr}(x)$:

$$\varepsilon^{pl}{}_{ij}(x) = \sum_{s=1}^{N} m_{ij}^{s}(x) \left(\frac{m_{ij}^{s}(x):\sigma(x)}{\tau^{s}(x)}\right)^{n} \operatorname{sgn}\left(m_{ij}^{s}(x):\sigma(x)\right) \quad (4.9)$$

$$\Delta\varepsilon^{tr} = m^{tr}(x):\Delta\gamma^{tw}(x) \quad (4.10)$$

where m_{ij}^{s} and m^{tr} are Schmid's tensor on slip and twin systems, respectively. $\Delta\varepsilon^{tr}$ exists during the build up process of twinning transformation; otherwise it is zero.

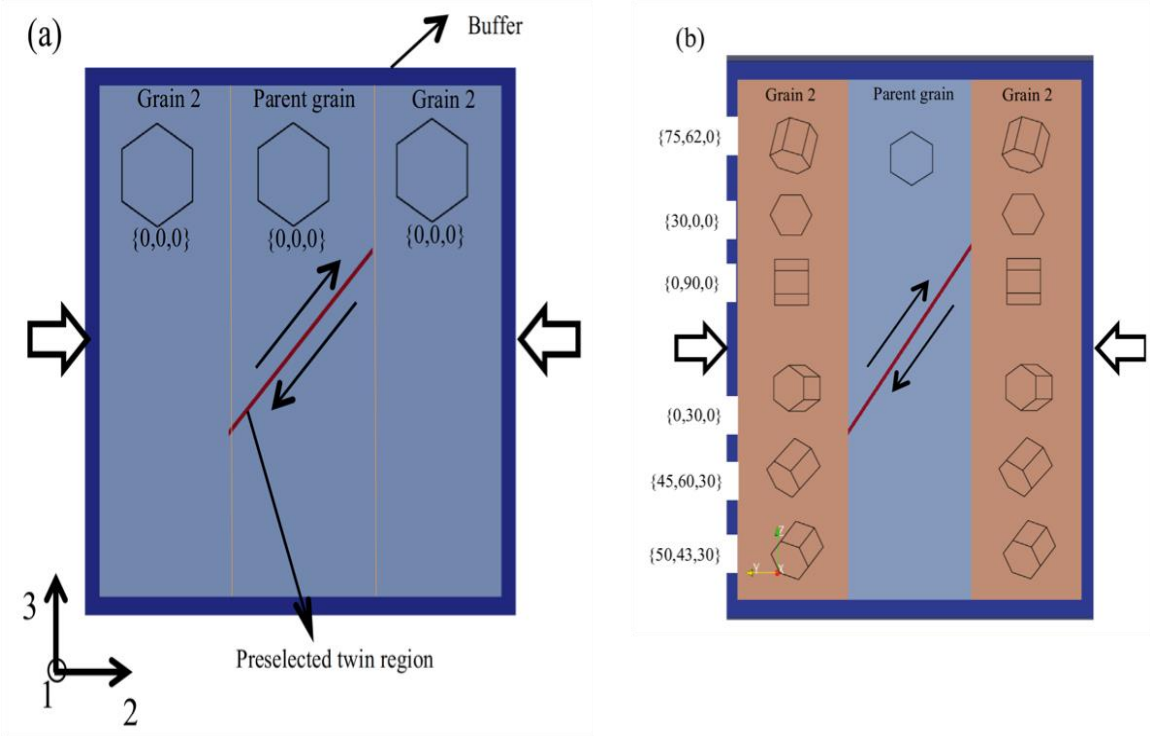

Figure 4.5 Schematic illustration of the simulation unit cell containing three grains

Schematic illustration of the simulation unit cell containing three grains, (a) a twin inside of a single crystal, (b) a twin embedded in crystal surrounded by two crystals with different orientations [218].

They used this formulation to study the effect of twin transformation and neighbor grain orientation on the local stress distribution in the parent grain. To consider effect of neighboring grains, they inserted a twinned region in several tricrystals (Figure 4.5). At a

first step, the effect of twin transformation was isolated by considering three grains of a same crystallographic orientation (Figure 4.5a).

As schematized in Figure 4.5, the twin domain corresponded to $(01\bar{1}2)$ $[0\bar{1}11]$ variant. Two different twin thicknesses of 13 and 7 voxels were considered, and they were associated with 1% and 0.5% twin volume fraction, respectively. The angle between the twin and compression axis was 43.1°, causing the Schmid's factor to be maximum.

Figure 4.6 shows the distribution of shear stress on the twin plane along the twin direction (T-RSS), embedded in one single crystal. T-RSS inside of the twin is homogeneous and negative, while it is positive in the surrounding medium. The heterogeneity of T-RSS at the twin tip is attributed to the reaction of the surrounding neighborhood and to the plastic compliance of neighboring grains to accommodate the twinning shear. Figure 4.7 shows the profile of T-RSS along the upper twin-parent interface in the parent grain from point A to B (see Figure 4.6). The profile is plotted at (i) before twin transformation, (ii) end of twin transformation, and (iii) further increase in stress. Kumar et al. [218] noted two important changes:

1. The profile changes from homogenous to heterogeneous in both the parent and twin,
2. The positive T-RSS in the parent reverses sign while the T-RSS in the neighboring regions increases.

These results seems to be in agreement with the measured shear stress by 3DXRD [213]. Twinning is unidirectional, and it starts to grow when the stress-state is positive at twin-parent interface. Due to higher T-RSS induced by the twinning transformation at the

twin tip, twin propagation takes place, while the negative induced T-RSS on the lateral interface of the twin obstructs further twin growth.

In the second, more realistic case, the effects of grain-grain interaction on twin growth were investigated by bounding the parent grain with grains having different orientations (Figure 4.5b). Figure 4.7 exhibits the T-RSS profile in the parent grains at the end of the transformation process and after further stress increase.

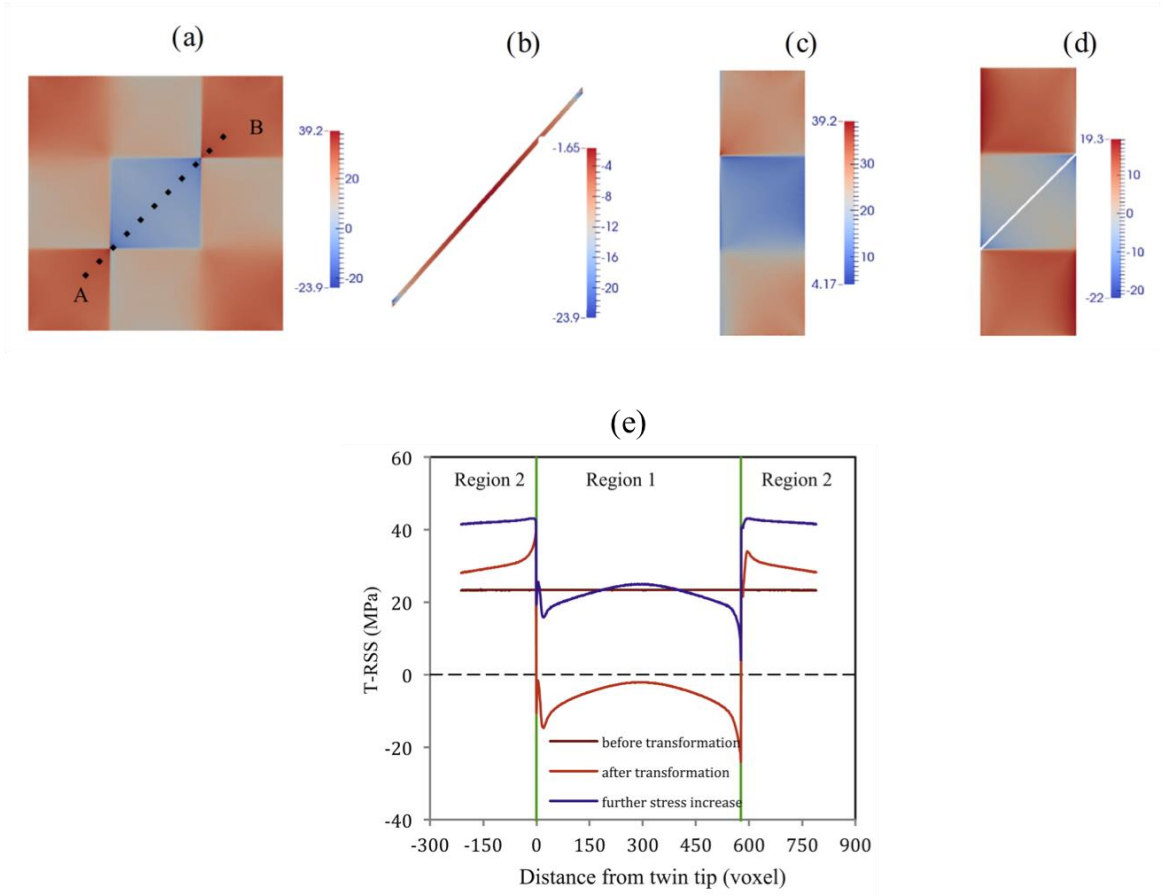

Figure 4.6 Distribution of resolved shear stress on twin system along twin direction

Distribution of the T-RSS the end of twinning transformation under an applied stress of -40 MPa for (a) the whole single crystal, (b) twin domain, (c) neighbor grains, and (d) the parent grain around twin, (e) T-RSS profile for single crystal from point A to point B in (a) [218].

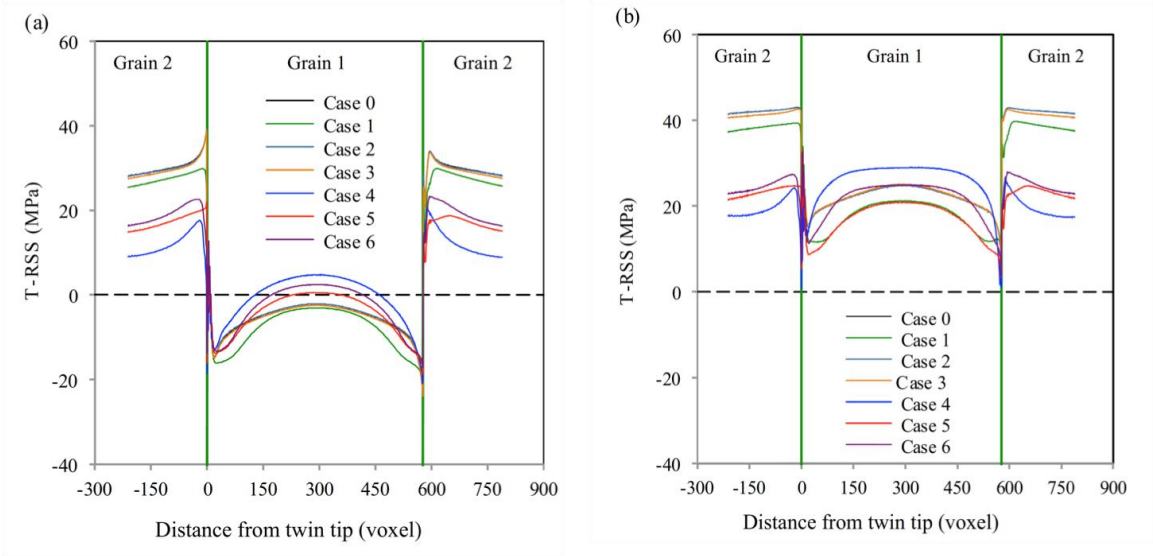

Figure 4.7 Effect of neighboring grains orientation on T-RSS profile

T-RSS profiles at twin-matrix interface in parent grains for six different neighbor grains: (a) at the end of transformation process, and (b) after further stress increase beyond -60 MPa [218].

All profiles have globally the same shape. Moreover, once the applied stress was increased, the sign of T-RSS at the twin-parent interface changes from negative to positive. Comparison of the profiles in Figure 4.6 and Figure 4.7 shows that the neighbor orientation has a significant effect on stress field at the twin tip. The external applied stress induced the resolve shear stress to overcome the backstress, which is induced by twin transformation in grains with high Schmid's factor. Consequently, those twins start to grow and expand [218]. Similarly, for twins with low Schmid factor, they start to grow when the applied stress increased to a point where the resolved shear stress is larger than the internal backstress. The statistical EBSD measurements performed by Beyerlein et al. [219] support the above calculations as they have shown a strong correlation between thicker twins and higher Schmid factors.

The body of literature shows several attempts to capture mechanical twinning in plastic deformation. However, incorporation of twin nucleation still lags. This may be due to the view of twin nucleation as a random event, which depends on the stochastic nature of dislocation reactions at grain boundaries. The complexity of these interactions greatly depend on the atomic structure of the grain boundary, which is in turn extremely sensitive to each of the to the five macroscopic degrees of freedom. Furthermore, these reactions are local and take place only at a few segments of the grain boundary.

4.4 Numerical difficulties in implementation of twinning in EVPFFT

This section is a contribution to identify challenges of numerical nature, which would be encountered in capturing twin nucleation in EVPFFT. To this end, we attempted to simulate $\{10\bar{1}2\}$ twinning in a bicrystal magnesium subjected to two different compression directions; one along the $\langle c \rangle$-axis prohibiting twinning and the other one normal to the $\langle c \rangle$-axis, which provides the maximum Schmid factor for this twin mode.

We constructed the bicrystal with respect to an imaginary rolling plate providing the reference frame. The two orientations of the two crystals are schematically illustrated in Figure 4.8. Specifically, the $([1\bar{2}10], [10\bar{1}0], [0001])$ crystal axes of the overlaying Grain 1 make (0,0,0) angles with the sample reference frame RD, TD, and ND, while those of the underlaying Grain 2 make (0,30,0) angles. $\{10\bar{1}2\}$ twinning is activated in Grain 1 when the bicrystal is subjected to compression along TD, while it is prohibited under compression along ND.

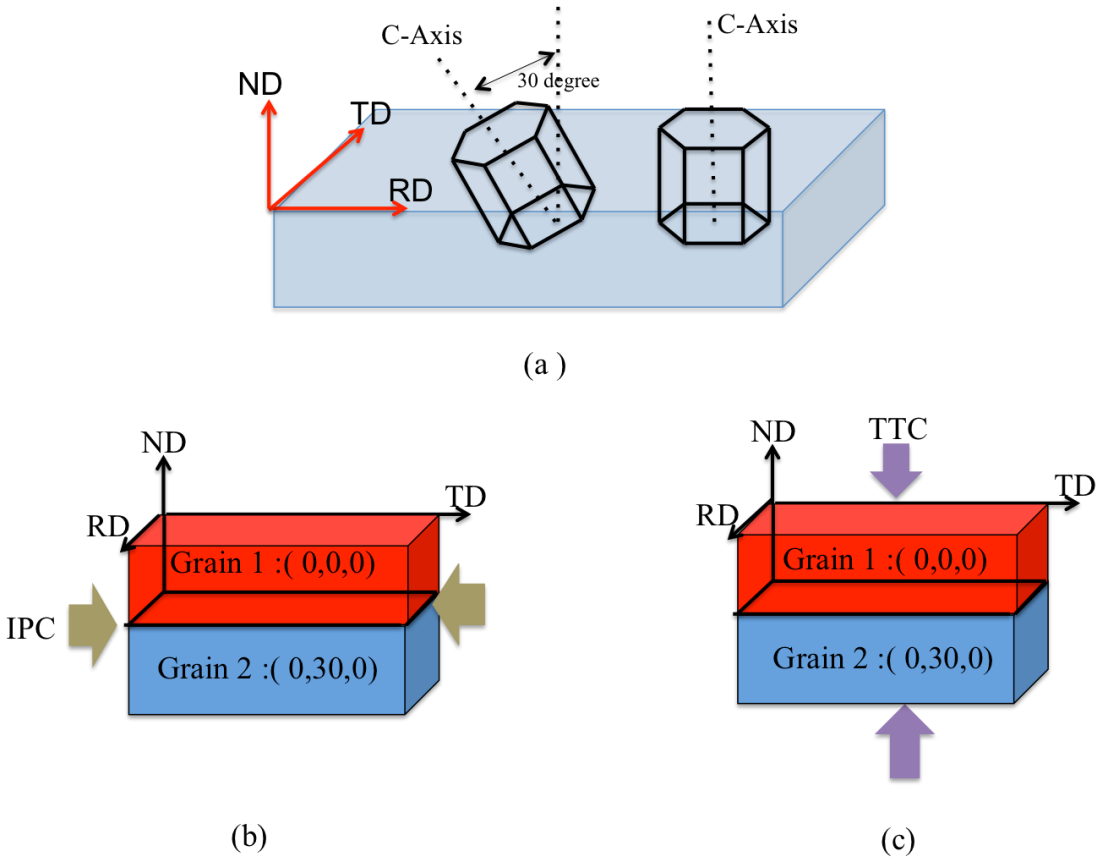

Figure 4.8 Schematic illustration of the bicrystal used in the EVPFFT simulations

Schematic illustration of the bicrystal used in the EVPFFT simulations illustrating (a) the orientations of the two grains with respect to an imaginary rolled plate, and (b) the two compression directions.

4.4.1 Simulation details

To perform EVPFFT simulations, the bicrystal input was discretized to $32 \times 32 \times 32$ Fourier points. Elastic constants of magnesium single crystal at room temperature are given in Figure 4.9 [117]. In a similar fashion to the hardening law used in VPFTT, the evolution of CRSS was captured by Voce law. Table 4.1 provides the initial value of CRSS and hardening parameters used in Voce equation to generate the stress-strain curve of the bicrystal.

$$\mathbf{C}^0 = \begin{pmatrix} 59.4 & 25.6 & 21.4 & 0 & 0 & 0 \\ 25.6 & 59.4 & 21.4 & 0 & 0 & 0 \\ 21.4 & 21.4 & 61.6 & 0 & 0 & 0 \\ 0 & 0 & 0 & 16.4 & 0 & 0 \\ 0 & 0 & 0 & 0 & 16.4 & 0 \\ 0 & 0 & 0 & 0 & 0 & 16.9 \end{pmatrix}$$

Figure 4.9 The elastic stiffness matrix of magnesium expressed in the crystal reference frame in units of GPa

Table 4.1 CRSS and hardening parameters used in EVPFFT

Deformation Mode	τ_0	τ_1	θ_0	θ_1
Basal <a>	10	30	100	0
Prismatic	55	80	500	0
Pyramidal <c+a>	60	90	1500	0
Tensile twin	30	0	30	30

Rate sensitivity parameter n is equal to 20

The applied strain-rate tensor components were $\dot{E}_{22} = -1, \dot{E}_{11} = \dot{E}_{33} = 0.281$ for TD, and $\dot{E}_{33} = -1\,, \dot{E}_{11} = \dot{E}_{22} = 0.281$ for ND, with 300 steps of 0.05% each.

4.4.2 Results

Figure 4.10 shows the stress-strain response generated by the above simulations. Due to the high disparities of initial CRSS values between different slip and $\{10\bar{1}2\}$ twinning, the yield stress of the bicrystal strongly depends on the loading direction, being much stronger along ND than along TD compression. .

The calculated relative activity of slip and twin modes are shown in Figure 4.11. Basal and Pyramidal slip systems mainly accommodate strain when the bicrystal is subjected to compression along ND. The reason for this is that the extension twin is unidirectional and does not operate under compression along the c-axis. In contrast compression along TD causes both basal and extension twin to trigger in order to accommodate extension along c-axis.

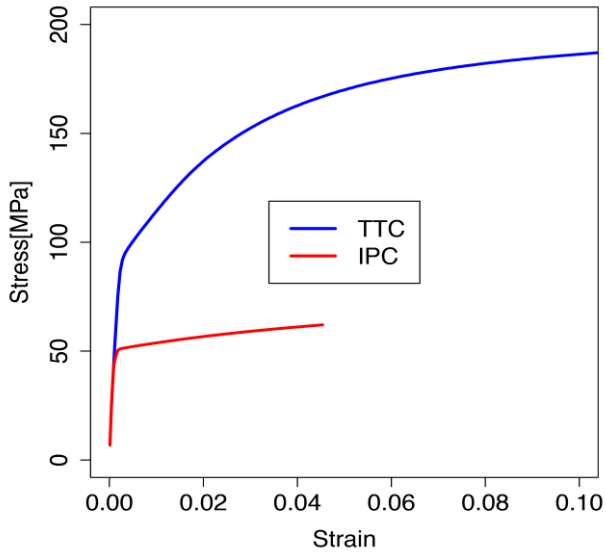

Figure 4.10 Stress-strain curve for compression along (a) ND and (b) TD generated by EVPFFT based simulations.

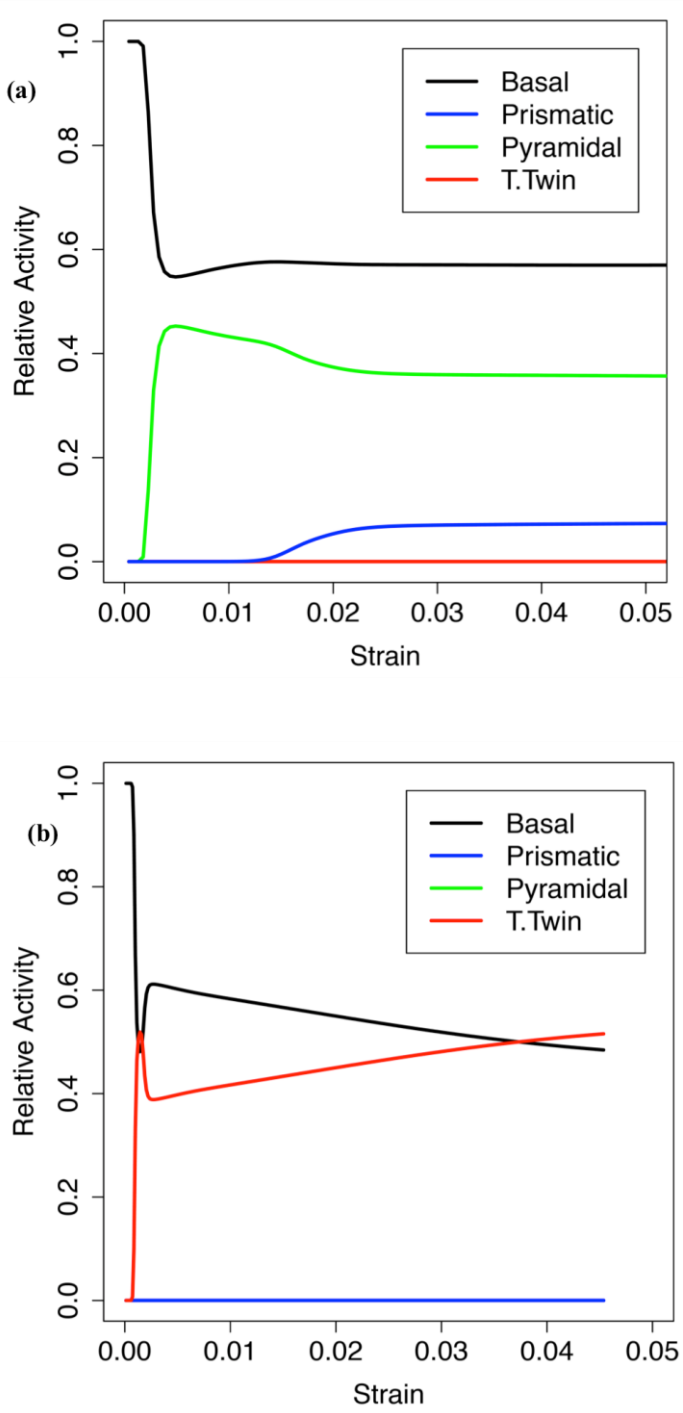

Figure 4.11 Simulated relative activity of deformation modes

Simulated relative activity of deformation modes under simple compression along (a) Through thickness compression (TTC) and (b) In plane compression (IPC).

4.4.3 Capturing twining in EVPFFT

As mentioned above, twin nucleation is currently understood as a random phenomenon taking place at surface defects such as grain boundaries, and there is not a widely accepted criterion for twin nucleation in crystal plasticity. The simplest and most commonly used criterion is that there is a CRSS for each twin system, and twinning may occur when the RSS on a twin system reaches the CRSS. Usually, twinning is viewed athermal, so the strain rate and temperature only upsets the CRSS for slip. The RSS on each twin system is given by

$$\tau^{tw} = m^{tw} : \sigma \qquad (4.11)$$

where τ^{tw} is the RSS on twin systems, while m^{tw} and σ are the corresponding Schmid and stress tensors, respectively. Due to the nature of the power law strain rate type sensitivity formulation implemented in EVPFFT (Equation IV-12), the RSS cannot attain the associated CRSS.

$$\dot{\mathcal{E}^s}_{ij}(x) = \sum_{s=1}^{N} m_{ij}^s(x) \left(\frac{m_{ij}^s(x) : \acute{\sigma}(x)}{\tau^s(x)}\right)^n sgn\left(m_{ij}^s(x) : \acute{\sigma}(x)\right) \qquad (4.12)$$

Equation (IV-12) is a power law equation, which was proposed to avoid singularities at the corner of yield surface of single crystal. Therefore, the RSS never reached the actual values of CRSS. More importantly, the value of maximum RSS is the same for all points near the grain boundary, so there would be no preferred point for twin nucleation at the grain boundary from the classical crystal plasticity standpoint, which is in contrast to local character known about twinning [41,212].

4.5. Conclusions

1. Twin nucleation is currently considered in crystal plasticity as a stochastic or random event taking place at surface defects such as a free surface or a the grain boundary. As long as this assumption is maintained, it would be difficult to capture the local character of twin nucleation in full field crystal plasticity.
2. Local conditions at or near grain boundaries such as material components and mechanical components have a dramatic influence on twin nucleation.
3. Numerical simulation of stress state around twins show that RSS inside of twin is homogenous but is heterogeneous near the twin-parent interface inside the parent.
4. Modeling twin transformation reveals that twin transformation strain either facilitates twin growth, or obstruct it during deformation.
5. The simplest and most commonly used criterion for twin nucleation in crystal plasticity is that twin can initiate when the resolved shear stress becomes equal or larger than its corresponding CRSS. However, because of the power law type rate sensitivity equation, RSS does not reach the assigned CRSS values, so in practice the activated systems that are selected are the ones that qualitatively have the highest resolved stress, More importantly, a major shortcoming is the current ability to capture the local nature of twinning.

CHAPTER V

SUMMARY AND FUTURE WORK

5.1 Highlights

1. As expected, for both BCC and FCC steels, stress was predicted to preferentially localize near grain boundaries, named as a mantle zone, where multi-slip conditions are required (vertices).
2. However, the extent of stress hot spot at the GBs is sensitive to the imposed deformation path. Plane strain compression showed the most pronounced mantle zone with sharp transition to the center of grains, named as core zone.
3. Stress hot spot analysis in typical TWIP steel textures reveals that deformation twins form mostly in regions with high local stresses, notably microstructural features such grain boundaries, triple junctions and quadruple points. This result is consistent with observed tendencies for twin nucleation, but it could be only valid for random textures.
4. Current numerical schemes adopted in crystal plasticity based on FFT, (probably not excluding CPFEM), to calculate strain and stress fields are not suited to capture the drastic lengthwise growing of the twin, which is an essential stage of twin nucleation. A transformative approach in crystal

plasticity may be needed to capture nucleation and propagation of twin lamellae.

5.2 Summary

In the present work, we used three-dimensional full field viscoplastic formulation based on FFT method (vpFFT) to predict local stress, local strain-rate, and local texture evolution in polycrystallines deforming by slip and twin. Three-dimensional data set of TWIP and Ferritic steel microstructure, obtained by serial sectioning using a FIB-EBSD technique, was employed as simulation inputs. The vpFFT simulation results such as predicted stress-strain curve and final texture were compared with the experimentally measured results under tension.

The investigation of deformation paths on stress and strain localization in Ferritic steel was presented in chapter II. The voce equation parameters were fitted with the help of available tension strain-stress curve. Then, the stress-strain curve, local texture evolution, and local stress/strain values were predicted in each material point for all deformation modes. The results show that the distribution of local strain rate and stress on the surface of the simulation box depends on the deformation mode.

To find the grain scale distribution of local heterogeneities, Euclidean distance from microstructural features such as grain boundaries, triple junction, and quadruple points were computed in each deformation mode. The strain rate values were binned by local distance to the grain boundaries. The correlation plots reveal that there are mantle zone regions near the grain boundaries, and that the width of mantle zone changes with deformation paths. For example, the width of the mantle zone region in tension and plane strain is the smallest and largest, respectively, while the local strain rate distributed

uniformly in grain scale without showing any mantle zone regions in torsion. Furthermore, the local strain rate values were binned, and the average distance within each bin to microstructural features was computed and plotted. High and low values of local stress and strain rate were found to lie near all microstructural features. The points near quadruple points and triple junction experience higher local strain rate and stress values compared to ones near grain boundaries.

Local Taylor factor shows a positive correlation with the local stress, and correlates inversely with the local strain rate. Deformation paths do not have significant effects on the correlation between Taylor factor and strain rate, while the correlation between local Taylor factor and local stress is slightly sensitive to deformation paths.

Distribution of local kernel average misorientation (KAM) and local stress gradient on the surface of simulation box are insensitive to deformation paths; moreover, the highest and smallest values of both local KAM and stress gradient lie near to grain boundaries and in the grain center, respectively. To investigate the correlation between KAM and stress gradient, the former values were binned by stress gradient values. The correlation plots indicate that KAM correlates strongly with stress gradient for tension and compression, whereas this correlation is slightly weaker for plane strain and torsion.

In Chapter III, to incorporate mechanical twinning in TWIP steel, we implemented PTR scheme in vpFFT code. The first challenge we encountered in capturing twin nucleation originates actually from the well-known crystallographic dependence between the strain rate brought about by twinning and its volume fraction. Due to the instable nature of the drastic lengthwise thickening, which is, to some extent, independent of the macroscopic stress, it was not possible within the iterative calculation

scheme currently adopted in the model to compute the volume fraction of twins as a constitutive response of the material. Rather, the volume fraction had to be computed after evaluation of stress and strain tensors at the end of each strain step. This is a major impediment to capture the lamellar morphology of twinning within a continuum framework. This difficulty can be solved by the fact that twin nucleation is known to correlate with a stress drop similar to the yield point effect. A second major challenge corresponded to the lack of understanding of the mechanisms that drive the site-specific phenomenon that characterizes twin nucleation.

However the volume fraction of twins was merely controlled with the predominant twin reorientation scheme previously proposed in mean-field crystal plasticity. The comparison between experimental and simulation results indicates that twin volume fraction, final texture, and stress-strain curve were satisfactorily predicted. Despite the that predominant twin reorientation scheme was not suitable to capture lamellar shape of twins in the microstructure, twin domains were predicted to form and grow at or close to grain boundary regions.

In chapter IV, we surveyed current literature, which aimed at capturing the characteristic lamellar morphology of twins. These studies were proven largely unsuccessful for several reasons. In addition to the difficulties mentioned above, twin nucleation is known to arise from slip dislocation dissociations, which occur either at the free surface (especially for sharp textures) or at grain boundaries, and are highly sensitive to stress fluctuation at these surface defects at early strain regimes. Furthermore, once a nucleation event takes place, it immediately relieves stress in the neighboring segments of the surface defect. This is because of the sudden increase in the twin volume

associated with the lengthwise growth or propagation, which leads to a very high local strain rate. These high sensitivities caused several authors [41,212] to assume that twin nucleation is a random event, a view which augments the barriers to identify a continuum numerical scheme suitable for capturing the physics of twin nucleation within the essentially continuum framework of crystal plasticity.

5.3 Future work

5.3.1 Chapter II: effect of deformation path on stress/strain-rate localization

Our study showed a noticeable effect of deformation path on the formation and width of this mantle zone (regions near grain boundaries), and the local strain rates values inside these mantle zones. To better understand these effects, numerical simulations of cyclic loadings where the deformation path is changed during mechanical testing of a given microstructure is warranted. The evolution of mantle and core zones may shed lights on the reasons for this dependence.

Moreover, most experimental studies for stress-strain localization were limited to two-dimensional characterization. It would be interesting to simulate deformation of previously experimentally studies microstructures and compare the results to infer the effect of three-dimensional state of deformation on hot spots.

5.3.2 Chapter III: effect of mechanical twinning on stress localization

The activation of mechanical twinning in TWIP steel strongly depends on temperature. It might be interesting to develop a strain-rate temperature dependent formulation to predict twin volume fraction at different temperatures and its effect on the stress localization. Twinning is known to be athermal, but the decrease in the CRSS of

slip, with temperature may decrease the activity of twinning. This could only be captured with the fitting parameter of the Voce model. However, a more physical consideration would require a model, which captures the onset of embryonic twin nucleation and its drastic shooting.

5.3.3 Chapter IV: current state and changes in capturing lamellar morphology of mechanical twinning

Many challenges must be overcome to capture the localized nature of twinning in crystal plasticity:

1. Twin nucleation occurs at the free surface and grain boundaries, and it does not seem to obey the Schmid's law. As such, crystal plasticity power Law [220] is not valid. A local stress-strain dependent criterion must be first devised at the atomistic level and then translated to the mesoscale level,
2. The spacing between the twins depends on the way the lengthwise growing relieves stress in the neighboring region. Thus, the lengthwise growing must be taken into consideration in the nucleation criterion, which complexifies the issue.
3. Another difficulty arises from the intermediate scale of dislocation interactions, in between atomistic and mesoscale, which pertains to stress concentration precursor to twin nucleation. Studies must be performed to understand how the stochastic nature of dislocation interaction and cross slip influences twin nucleation.

4. Edgewise twin propagation seems to obey the Schmid's law, so the rate-dependent stress-strain rate crystal plasticity power law [220] can be maintained to simulate this stage of twin growth. However, it may not be reliable to simulate competition between different variant during nucleation and growth, especially twin-twin interactions. In fact, it has been demonstrated that twin-twin interactions lead to a higher number fraction of twins, and thus impact the non-Schmid's character of twin nucleation. Future studies should be able to link between edgewise twin propagation and twin nucleation as well.

REFERENCES

[1] C. Bettles, M. Barnett, Advances in Wrought Magnesium Alloys: Fundamentals of Processing, Properties and Applications, Elsevier, 2012.

[2] U. Kocks, D. Westlake, AIME MET SOC TRANS 239 (1967) 1107.

[3] A.N. Chamos, C.A. Charitidis, A. Skarmoutsou, S.G. Pantelakis, Fatigue Fract. Eng. Mater. Struct. 33 (2010) 252.

[4] F.E. Hauser, P.R. Landon, J.E. Dorn, Deformation and Fracture of Alpha Solid Solutions of Lithium in Magnesium, Minerals Research Laboratory, Institute of Engineering Research, University of California, Berkeley, 1956.

[5] Y. Zhang, P.C. Millett, M. Tonks, B. Biner, Scr. Mater. (2011).

[6] 9 S. Mahajan, D.F. Williams, Int. Mater. Rev. 18 (1973) 43.

[7] M.R. Barnett, N. Stanford, P. Cizek, A. Beer, Z. Xuebin, Z. Keshavarz, JOM J. Miner. Met. Mater. Soc. 61 (2009) 19.

[8] L. Jiang, J.J. Jonas, A.A. Luo, A.K. Sachdev, S. Godet, Mater. Sci. Eng. A 445 (2007) 302.

[9] J. Koike, Metall. Mater. Trans. A 36 (2005) 1689.

[10] Q. Ma, H.E. Kadiri, A.L. Oppedal, J.C. Baird, M.F. Horstemeyer, M. Cherkaoui, Scr. Mater. (2011).

[11] R. Reed-Hill, W. Robertson, Acta Metall. 5 (1957) 717.

[12] H. El Kadiri, J. Kapil, A.L. Oppedal, L.G. Hector Jr., S.R. Agnew, M. Cherkaoui, S.C. Vogel, Acta Mater. 61 (2013) 3549.

[13] J.W. Christian, S. Mahajan, Prog. Mater. Sci. 39 (1995) 1.

[14] M.A. Meyers, O. Vöhringer, V.A. Lubarda, Acta Mater. 49 (2001) 4025.

[15] A. Serra, D.J. Bacon, Phil Mag A 73 (1996) 333.

[16] A. Serra, D.J. Bacon, R.C. Pond, Phys. Rev. Lett. 104 (2010) 29603.

[17] R. Bell, R. Cahn, Acta Metall. 1 (1953) 752.

[18] P. Price, Proc. R. Soc. Lond. Ser. Math. Phys. Sci. (1961) 251.

[19] P. Price, J. Appl. Phys. 32 (1961) 1746.

[20] N. Allen, B. Hopkins, J. McLennan, Proc. R. Soc. Lond. Ser. Math. Phys. Sci. 234 (1956) 221.

[21] C.N. Reid, A. Gilbert, G.T. Hahn, Acta Metall. 14 (1966) 975.

[22] C.V. Thompson, R. Carel, in:, Trans Tech Publ, 1996, pp. 83–98.

[23] J.W. Christian, The Theory of Transformations in Metals and Alloys (part I+ II), Access Online via Elsevier, 2002.

[24] P. Price, J. Appl. Phys. 32 (1961) 1746.

[25] P. Price, Proc. R. Soc. Lond. Ser. Math. Phys. Sci. (1961) 251.

[26] S. Mendelson, J. Appl. Phys. 41 (1970) 1893.

[27] S. Mendelson, Nat Bur StandUS Spec Publ No 317 495-529 Dec 1970 (1970).

[28] S. Mendelson, SCR MET 4 (1970) 5.

[29] S. Mendelson, J. Appl. Phys. 40 (1969) 1988.

[30] S. Mendelson, Mater. Sci. Eng. 4 (1969) 231.

[31] R.W. Armstrong, W. Arnold, F.J. Zerilli, Metall. Mater. Trans. A 38 (2007) 2605.

[32] R.W. Armstrong, W. Arnold, F.J. Zerilli, Metall. Mater. Trans. A 38 (2007) 2605.

[33] M. Barnett, M. Nave, C. Bettles, Mater. Sci. Eng. A 386 (2004) 205.

[34] E. El-Danaf, S.R. Kalidindi, R.D. Doherty, Metall. Mater. Trans. A 30 (1999) 1223.

[35] M.R. Barnett, Z. Keshavarz, A.G. Beer, X. Ma, Acta Mater. 56 (2008) 5.

[36] Q. Yu, Z.-W. Shan, J. Li, X. Huang, L. Xiao, J. Sun, E. Ma, Nature 463 (2010) 335.

[37] M.R. Barnett, Z. Keshavarz, A.G. Beer, D. Atwell, Acta Mater. 52 (2004) 5093.

[38] X.Z. Liao, Y.H. Zhao, S.G. Srinivasan, Y.T. Zhu, R.Z. Valiev, D.V. Gunderov, Appl. Phys. Lett. 84 (2004) 592.

[39] X.L. Wu, Y.T. Zhu, Phys. Rev. Lett. 101 (2008) 025503.

[40] L. Zhang, G. Huang, H. Zhang, B. Song, J. Mater. Process. Technol. (2010).

[41] I.J. Beyerlein, R.J. McCabe, C.N. Tomé, J. Mech. Phys. Solids 59 (2011) 988.

[42] L. Capolungo, I. Beyerlein, Phys. Rev. B 78 (2008) 024117.

[43] H. El Kadiri, J.C. Baird, J. Kapil, A.L. Oppedal, M. Cherkaoui, S.C. Vogel, Int. J. Plast. 44 (2013) 111.

[44] I.J. Beyerlein, N.A. Mara, J. Wang, J.S. Carpenter, S.J. Zheng, W.Z. Han, R.F. Zhang, K. Kang, T. Nizolek, T.M. Pollock, JOM 64 (2012) 1192.

[45] M. Wang, B.Y. Zong, G. Wang, Comput. Mater. Sci. 45 (2009) 217.

[46] J. Wang, L. Liu, C.N. Tomé, S.X. Mao, S.K. Gong, Mater. Res. Lett. 1 (2013) 81.

[47] C.D. Barrett, H. El Kadiri, Acta Mater. 70 (2014) 137.

[48] S. Mahajan, Philos. Mag. 23 (1971) 781.

[49] A.W. Sleeswyk, Acta Metall. 10 (1962) 705.

[50] C.D. Barrett, H. El Kadiri, Acta Mater. 70 (2014) 137.

[51] C.D. Barrett, H. El Kadiri, Acta Mater. 63 (2014) 1.

[52] A. Ostapovets, A. Serra, Philos. Mag. 94 (2014) 2827.

[53] B. Xu, L. Capolungo, D. Rodney, Scr. Mater. 68 (2013) 901.

[54] B. Li, E. Ma, Philos. Mag. 89 (2009) 1223.

[55] A. Serra, D.J. Bacon, R.C. Pond, Submitt. Philozophical Mag. (2012).

[56] P.D. Bristowe, A.G. Crocker, Acta Metall. 25 (1977) 1363.

[57] M. Yamaguchi, V. Vitek, J. Phys. F Met. Phys. 3 (1973) 523.

[58] A.H. Cottrell, B.A. Bilby, Philos. Mag. 42 (1951) 573.

[59] N. Thompson, D. Millard, Phil Mag 43 (1952) 422.

[60] P.L. Pratt, S.F. Pugh, J. Inst. Met. 80 (1952) 653.

[61] P.L. Pratt, S.F. Pugh, Some Observations on the Cleavage Face of Zinc Crystals, Atomic Energy Research Establishment, Harwell, Berks, (England), 1952.

[62] J.J. Gilman, Trans AIME 200 (1954) 621.

[63] H.S. Rosenbaum, Reed-Hill RE Hirth JP Rogers HC Deform. Twinning Gordon Breach N. Y. (1964) 43.

[64] H.S. Rosenbaum, Acta Metall. 9 (1961) 742.

[65] J. Holden, Philos. Mag. Ser. 7 43 (1952) 976.

[66] F.J. Zerilli, R.W. Armstrong, J. Phys. IV 7 (1997) 3.

[67] F.J. Zerilli, R.W. Armstrong, Grain Size Mech. Prop. Fundam. Appl. (1994) 149.

[68] M. Li, X.Y. Lou, J.H. Kim, R.H. Wagoner, Int. J. Plast. 26 (2010) 820.

[69] I. Beyerlein, C. Tomé, Proc. R. Soc. Math. Phys. Eng. Sci. 466 (2010) 2517.

[70] A.L. Oppedal, H. El Kadiri, C.N. Tomé, G.C. Kaschner, S.C. Vogel, J.C. Baird, M.F. Horstemeyer, Int. J. Plast. 30-31 (2012) 41.

[71] L. Rémy, Metall. Trans. A 12 (1981) 387.

[72] L. Rémy, Acta Metall. 25 (1977) 711.

[73] S.R. Kalidindi, J. Mech. Phys. Solids 46 (1998) 267.

[74] R.A. Lebensohn, C.N. Tomé, Acta Metall. Mater. 41 (1993) 2611.

[75] P. van Houtte, Acta Metall. 26 (1978) 591.

[76] G.B. Sarma, P.R. Dawson, Acta Mater. 44 (1996) 1937.

[77] B.S. El-Dasher, B.L. Adams, A.D. Rollett, Scr. Mater. 48 (2003) 141.

[78] T. Leffers, Int. J. Plast. 17 (2001) 469.

[79] J.F. Nye, Acta Metall. 1 (1953) 153.

[80] S.K. Mishra, P. Pant, K. Narasimhan, A.D. Rollett, I. Samajdar, Scr. Mater. 61 (2009) 273.

[81] H.F. Poulsen, in:, Three-Dimens. X-Ray Diffr. Microsc., Springer Berlin Heidelberg, 2004, pp. 73–81.

[82] W. Ludwig, P. Reischig, A. King, M. Herbig, E.M. Lauridsen, G. Johnson, T.J. Marrow, J.Y. Buffière, Rev. Sci. Instrum. 80 (2009) 033905.

[83] R.M. Suter, D. Hennessy, C. Xiao, U. Lienert, Rev. Sci. Instrum. 77 (2006) 123905.

[84] H.F. Poulsen, in:, Three-Dimens. X-Ray Diffr. Microsc., Springer Berlin Heidelberg, 2004, pp. 89–94.

[85] D.J. Jensen, S. Schmidt, Mater. Trans. 50 (2009) 1655.

[86] S.F. Li, R.M. Suter, J. Appl. Crystallogr. 46 (2013) 512.

[87] J.V. Bernier, N.R. Barton, U. Lienert, M.P. Miller, J. Strain Anal. Eng. Des. 46 (2011) 527.

[88] N.R. Barton, J.V. Bernier, J. Appl. Crystallogr. 45 (2012) 1145.

[89] U. Lienert, S.F. Li, C.M. Hefferan, J. Lind, R.M. Suter, J.V. Bernier, N.R. Barton, M.C. Brandes, M.J. Mills, M.P. Miller, B. Jakobsen, W. Pantleon, JOM 63 (2011) 70.

[90] D.W. Brown, S.R. Agnew, M.A.M. Bourke, T.M. Holden, S.C. Vogel, C.N. Tomé, Mater. Sci. Eng. A 399 (2005) 1.

[91] P.R. Dawson, D.E. Boyce, R.B. Rogge, Mater. Sci. Eng. A 399 (2005) 13.

[92] R.A. Schwarzer, D.P. Field, B.L. Adams, M. Kumar, A.J. Schwartz, in:, A.J. Schwartz, M. Kumar, B.L. Adams, D.P. Field (Eds.), Electron Backscatter Diffr. Mater. Sci., Springer US, 2009, pp. 1–20.

[93] M. De Graef, Introduction to Conventional Transmission Electron Microscopy, Cambridge University Press, Cambridge, 2003.

[94] S. Zaefferer, S.I. Wright, in:, A.J. Schwartz, M. Kumar, B.L. Adams, D.P. Field (Eds.), Electron Backscatter Diffr. Mater. Sci., Springer US, 2009, pp. 109–122.

[95] H.F. Poulsen, in:, Three-Dimens. X-Ray Diffr. Microsc., Springer Berlin Heidelberg, 2004, pp. 89–94.

[96] G. Sachs, Z Ver Dtsch Ing 72 (1928) 734.

[97] G. Taylor, J. Inst. Met. 62 (1938) 307.

[98] J.F.W. Bishop, R. Hill, Lond. Edinb. Dublin Philos. Mag. J. Sci. 42 (1951) 414.

[99] J.S. Kallend, G.J. Davies, Philos. Mag. 25 (1972) 471.

[100] R.A. Lebensohn, C.N. Tomé, Acta Metall. Mater. 41 (1993) 2611.

[101] A.J.B. Jr, H. Mecking, U.F. Kocks, Philos. Mag. A 73 (1996) 1503.

[102] F. Roters, P. Eisenlohr, L. Hantcherli, D.D. Tjahjanto, T.R. Bieler, D. Raabe, Acta Mater. 58 (2010) 1152.

[103] S.R. Kalidindi, A. Bhattacharyya, R.D. Doherty, Proc. R. Soc. Lond. Math. Phys. Eng. Sci. 460 (2004) 1935.

[104] R. A. Lebensohn, Acta Mater. 49 (2001) 2723.

[105] H. Moulinec, P. Suquet, Comput. Methods Appl. Mech. Eng. 157 (1998) 69.

[106] J.S. Walker, Fast Fourier Transforms, Second Edition, 2nd edition, CRC Press, Boca Raton, Fla, 1996.

[107] A.D. Rollett, R.A. Lebensohn, M. Groeber, Y. Choi, J. Li, G.S. Rohrer, Model. Simul. Mater. Sci. Eng. 18 (2010) 074005.

[108] C. Phatak, A.K. Petford-Long, M. De Graef, Phys. Rev. Lett. 104 (2010) 253901.

[109] H. Moulinec, P. Suquet, Comput. Methods Appl. Mech. Eng. 157 (1998) 69.

[110] J.C. Michel, H. Moulinec, P. Suquet, Int. J. Numer. Methods Eng. 52 (2001) 139.

[111] R.A. Lebensohn, A.K. Kanjarla, P. Eisenlohr, Int. J. Plast. 32–33 (2012) 59.

[112] R.A. Lebensohn, R. Brenner, O. Castelnau, A.D. Rollett, Acta Mater. 56 (2008) 3914.

[113] R.A. Lebensohn, Y. Liu, P. Ponte Castañeda, Acta Mater. 52 (2004) 5347.

[114] N. Allain-Bonasso, F. Wagner, S. Berbenni, D.P. Field, Mater. Sci. Eng. A 548 (2012) 56.

[115] S.F. Li, J. Lind, C.M. Hefferan, R. Pokharel, U. Lienert, A.D. Rollett, R.M. Suter, J. Appl. Crystallogr. 45 (2012) 1098.

[116] G. Taylor, J. Inst. Met. 62 (1938) 307.

[117] U.F. Kocks, C.N. Tomé, H.R. Wenk, Camb. Univ. Press POB 110 Camb. CB 2 3 RL UK 2000 676 (2000).

[118] S.I. Wright, D.P. Field, Mater. Sci. Eng. A 257 (1998) 165.

[119] T.R. Bieler, P. Eisenlohr, C. Zhang, H.J. Phukan, M.A. Crimp, Curr. Opin. Solid State Mater. Sci. 18 (2014) 212.

[120] T. Bieler, R.L. Goetz, S.L. Semiatin, Mater. Sci. Eng. A 405 (2005) 201.

[121] T.R. Bieler, P.D. Nicolaou, S.L. Semiatin, Metall. Mater. Trans. A 36 (2005) 129.

[122] M. Sutton, W. Wolters, W. Peters, W. Ranson, S. McNeill, Image Vis. Comput. 1 (1983) 133.

[123] H.A. Bruck, S.R. McNeill, M.A. Sutton, W.H.P. Iii, Exp. Mech. 29 (1989) 261.

[124] W.Z. Abuzaid, M.D. Sangid, J.D. Carroll, H. Sehitoglu, J. Lambros, J. Mech. Phys. Solids 60 (2012) 1201.

[125] M.A. Tschopp, B.B. Bartha, W.J. Porter, P.T. Murray, S.B. Fairchild, Metall. Mater. Trans. A 40 (2009) 2363.

[126] C.S. Lee, B.J. Duggan, Acta Metall. Mater. 41 (1993) 2691.

[127] O. Diard, S. Leclercq, G. Rousselier, G. Cailletaud, Int. J. Plast. 21 (2005) 691.

[128] P. Dawson, J. Gerken, T. Marin, in:, S. Ghosh, D. Dimiduk (Eds.), Comput. Methods Microstruct.-Prop. Relatsh., Springer US, 2011, pp. 363–392.

[129] A.C. Lewis, A.B. Geltmacher, Scr. Mater. 55 (2006) 81.

[130] A.C. Lewis, C. Suh, M. Stukowski, A.B. Geltmacher, G. Spanos, K. Rajan, JOM 58 (2006) 52.

[131] A.C. Lewis, C. Suh, M. Stukowski, A.B. Geltmacher, K. Rajan, G. Spanos, Scr. Mater. 58 (2008) 575.

[132] R. A. Lebensohn, Acta Mater. 49 (2001) 2723.

[133] R.A. Lebensohn, R. Brenner, O. Castelnau, A.D. Rollett, Acta Mater. 56 (2008) 3914.

[134] A. Prakash, R.A. Lebensohn, Model. Simul. Mater. Sci. Eng. 17 (2009) 064010.

[135] H. Moulinec, P. Suquet, Comput. Methods Appl. Mech. Eng. 157 (1998) 69.

[136] A.D. Rollett, R.A. Lebensohn, M. Groeber, Y. Choi, J. Li, G.S. Rohrer, Model. Simul. Mater. Sci. Eng. 18 (2010) 074005.

[137] H. Beladi, G.S. Rohrer, Acta Mater. 61 (2013) 1404.

[138] M.A. Groeber, M.A. Jackson, Integrating Mater. Manuf. Innov. 3 (2014) 5.

[139] R.A. Lebensohn, Y. Liu, P.P. Castañeda, Proc. R. Soc. Lond. Ser. Math. Phys. Eng. Sci. 460 (2004) 1381.

[140] J.C. Michel, H. Moulinec, P. Suquet, CMES - Comput. Model. Eng. Sci. 1 (2000) 79.

[141] L.S. Tóth, A. Molinari, D. Raabe, Metall. Mater. Trans. A 28 (1997) 2343.

[142] C. Tome, G.R. Canova, U.F. Kocks, N. Christodoulou, J.J. Jonas, Acta Metall. 32 (1984) 1637.

[143] U.F. Kocks, C.N. Tome, H.-R. Wenk, Texture and Anisotropy. Preferred Orientations in Polycrystals and Their Effect on Material Properties, Cambridge University Press, Cambridge, UK (1998), n.d.

[144] H. Moulinec, P. Suquet, Eur. J. Mech. - ASolids 22 (2003) 751.

[145] F. Barbe, L. Decker, D. Jeulin, G. Cailletaud, Int. J. Plast. 17 (2001) 513.

[146] T. Saito, J.-I. Toriwaki, Pattern Recognit. 27 (1994) 1551.

[147] Q. Liu, D. Juul Jensen, N. Hansen, Q. Liu, D. Juul Jensen, N. Hansen, Acta Mater 46 (1998) 5819.

[148] M. Zehetbauer, T. Ungár, R. Kral, A. Borbély, E. Schafler, B. Ortner, H. Amenitsch, S. Bernstorff, Acta Mater. 47 (1999) 1053.

[149] D. Raabe, M. Sachtleber, Z. Zhao, F. Roters, S. Zaefferer, Acta Mater. 49 (2001) 3433.

[150] S.V. Harren, R.J. Asaro, J. Mech. Phys. Solids 37 (1989) 191.

[151] D.P. Mika, P.R. Dawson, Mater. Sci. Eng. A 257 (1998) 62.

[152] B. Alexandreanu, O.K. Chopra, W.J. Shack, in:, 2005, pp. 579–588.

[153] E.M. Lehockey, A.M. Brennenstuhl, S. Pagan, M.A. Clark, V. Provic, in:, 2007, pp. 465–498.

[154] S.I. Wright, M.M. Nowell, D.P. Field, Microsc. Microanal. 17 (2011) 316.

[155] J. Jiang, T.B. Britton, A.J. Wilkinson, Acta Mater. 61 (2013) 7227.

[157] S. Kobayashi, S. Tsurekawa, T. Watanabe, Acta Mater. 53 (2005) 1051.

[158] V. Randle, N. Hansen, D.J. Jensen, Philos. Mag. A 73 (1996) 265.

[159] A.D. Rollett, F. Wagner, N. Allain-Bonasso, D.P. Field, R.A. Lebensohn, Mater. Sci. Forum 702-703 (2011) 463.

[160] D. Raabe, Z. Zhao, S.-J. Park, F. Roters, Acta Mater. 50 (2002) 421.

[161] O. Grässel, L. Krüger, G. Frommeyer, L.W. Meyer, Int. J. Plast. 16 (2000) 1391.

[162] E. El-Danaf, S.R. Kalidindi, R.D. Doherty, Metall. Mater. Trans. A 30 (1999) 1223.

[163] M. Pozuelo, J.E. Wittig, J.A. Jiménez, G. Frommeyer, Metall. Mater. Trans. A 40 (2009) 1826.

[164] H. Beladi, I.B. Timokhina, Y. Estrin, J. Kim, B.C. De Cooman, S.K. Kim, Acta Mater. 59 (2011) 7787.

[165] J.W. Christian, S. Mahajan, Prog. Mater. Sci. 39 (1995) 1.

[166] P.V. Houtte, Acta Metall. 26 (1978) 591.

[167] C.N. Tomé, R.A. Lebensohn, U.F. Kocks, Acta Metall. Mater. 39 (1991) 2667.

[168] H. El Kadiri, A.L. Oppedal, J. Mech. Phys. Solids 58 (2010) 613.

[169] I.J. Beyerlein, N.A. Mara, D. Bhattacharyya, D.J. Alexander, C.T. Necker, Int. J. Plast. 27 (2011) 121.

[170] F. Roters, P. Eisenlohr, L. Hantcherli, D.D. Tjahjanto, T.R. Bieler, D. Raabe, Acta Mater. 58 (2010) 1152.

[171] A. Staroselsky, L. Anand, Int. J. Plast. 19 (2003) 1843.

[172] S.R. Kalidindi, J. Mech. Phys. Solids 46 (1998) 267.

[173] S. R. Kalidindi, Int. J. Plast. 17 (2001) 837.

[174] S.-H. Choi, D.W. Kim, B.S. Seong, A.D. Rollett, Int. J. Plast. 27 (2011) 1702.

[175] E.J. Shin, A. Jung, S.-H. Choi, A.D. Rollett, S.S. Park, Mater. Sci. Eng. A 538 (2012) 190.

[176] S.-H. Choi, D.H. Kim, S.S. Park, B.S. You, Acta Mater. 58 (2010) 320.

[177] H. Moulinec, P. Suquet, Comput. Methods Appl. Mech. Eng. 157 (1998) 69.

[178] R. A. Lebensohn, Acta Mater. 49 (2001) 2723.

[179] R.A. Lebensohn, R. Brenner, O. Castelnau, A.D. Rollett, Acta Mater. 56 (2008) 3914.

[180] R.A. Lebensohn, Y. Liu, P. Ponte Castañeda, Acta Mater. 52 (2004) 5347.

[181] A.D. Rollett, R.A. Lebensohn, M. Groeber, Y. Choi, J. Li, G.S. Rohrer, Model. Simul. Mater. Sci. Eng. 18 (2010) 074005.

[182] H. Beladi, G.S. Rohrer, Acta Mater. 61 (2013) 1404.

[183] M.A. Groeber, M.A. Jackson, Integrating Mater. Manuf. Innov. 3 (2014) 5.

[184] R.A. Lebensohn, E.M. Bringa, A. Caro, Acta Mater. 55 (2007) 261.

[185] C. Tome, G.R. Canova, U.F. Kocks, N. Christodoulou, J.J. Jonas, Acta Metall. 32 (1984) 1637.

[186] C.N. Tomé, P.J. Maudlin, R.A. Lebensohn, G.C. Kaschner, Acta Mater. 49 (2001) 3085.

[187] I.J. Beyerlein, R.J. McCabe, C.N. Tomé, J. Mech. Phys. Solids 59 (2011) 988.

[188] N.P. Gurao, P. Kumar, B. Bhattacharya, A. Haldar, S. Suwas, Metall. Mater. Trans. A 43 (2012) 5193.

[189] R.A. Lebensohn, P.P. Castañeda, R. Brenner, O. Castelnau, in:, S. Ghosh, D. Dimiduk (Eds.), Comput. Methods Microstruct.-Prop. Relatsh., Springer US, 2011, pp. 393–441.

[190] A.A. Saleh, E.V. Pereloma, A.A. Gazder, Acta Mater. 61 (2013) 2671.

[191] D.P. Field, B.W. True, T.M. Lillo, J.E. Flinn, Mater. Sci. Eng. A 372 (2004) 173.

[192] I. Ghamarian, Y. Liu, P. Samimi, P.C. Collins, Acta Mater. 79 (2014) 203.

[193] J. Wang, I.J. Beyerlein, Model. Simul. Mater. Sci. Eng. 20 (2012) 024002.

[194] A. Serra, D.J. Bacon, R.C. Pond, Phys. Rev. Lett. 104 (2010) 029603.

[195] B.C. De Cooman, J. Kim, S. Lee, Scr. Mater. 66 (2012) 986.

[196] G. Winther, Acta Mater. 56 (2008) 1919.

[197] G. Taylor, J. Inst. Met. 62 (1938) 307.

[198] S. Mahajan, G.Y. Chin, Acta Metall. 21 (1973) 1353.

[199] I. Karaman, H. Sehitoglu, K. Gall, Y.I. Chumlyakov, H.J. Maier, Acta Mater. 48 (2000) 1345.

[200] J. Lind, S.F. Li, R. Pokharel, U. Lienert, A.D. Rollett, R.M. Suter, Acta Mater. 76 (2014) 213.

[201] D. Barbier, N. Gey, S. Allain, N. Bozzolo, M. Humbert, Mater. Sci. Eng. A 500 (2009) 196.

[202] I. Gutierrez-Urrutia, S. Zaefferer, D. Raabe, Mater. Sci. Eng. A 527 (2010) 3552.

[203] P. Paufler, Cryst. Res. Technol. 29 (1994) 532.

[204] S. Dancette, L. Delannay, K. Renard, M.A. Melchior, P.J. Jacques, Acta Mater. 60 (2012) 2135.

[205] S. Miura, J. Takamura, N. Narita, Trans JIM 9 (1968) 555.

[206] F. Barbe, R. Quey, A. Musienko, G. Cailletaud, Mech. Res. Commun. 36 (2009) 762.

[207] E. Héripré, M. Dexet, J. Crépin, L. Gélébart, A. Roos, M. Bornert, D. Caldemaison, Int. J. Plast. 23 (2007) 1512.

[208] H.S. Rosenbaum, Reed-Hill RE Hirth JP Rogers HC Deform. Twinning Gordon Breach N. Y. (1964) 43.

[209] F.C. Frank, Discuss Faraday Soc 5 (1949) 48.

[210] I.J. Beyerlein, L. Capolungo, P.E. Marshall, R.J. McCabe, C.N. Tomé, Philos. Mag. 90 (2010) 2161.

[211] L. Capolungo, P. Marshall, R. McCabe, I. Beyerlein, C. Tomé, Acta Mater. 57 (2009) 6047.

[212] I.J. Beyerlein, C.N. Tomé, Proc. R. Soc. Math. Phys. Eng. Sci. 466 (2010) 2517.

[213] C.C. Aydıner, J.V. Bernier, B. Clausen, U. Lienert, C.N. Tomé, D.W. Brown, Phys. Rev. B 80 (2009) 024113.

[214] T.R. Bieler, L. Wang, A.J. Beaudoin, P. Kenesei, U. Lienert, Metall. Mater. Trans. A 45 (2013) 109.

[215] R.A. Lebensohn, C.N. Tomé, Philos. Mag. A 67 (1993) 187.

[216] H. Abdolvand, M.R. Daymond, J. Mech. Phys. Solids 61 (2013) 783.

[217] H. Abdolvand, M.R. Daymond, J. Mech. Phys. Solids 61 (2013) 803.

[218] M. Arul Kumar, A.K. Kanjarla, S.R. Niezgoda, R.A. Lebensohn, C.N. Tomé, Acta Mater. 84 (2015) 349.

[219] I. Beyerlein, L. Capolungo, P. Marshall, R. McCabe, C. Tomé, Philos. Mag. 90 (2010) 2161.

[220] J.W. Hutchinson, Proc. R. Soc. Lond. Math. Phys. Eng. Sci. 348 (1976) 101.